Gravitational waves signal analysis: Matched filtering, typical analyses and beyond

Auteur : Janquart, Justin
Promoteur(s) : Cudell, Jean-Rene
Faculté : Faculté des Sciences
Diplôme : Master en sciences spatiales, à finalité approfondie
Année académique : 2019-2020
URI/URL : https://github.com/lemnis12?tab=repositories; http://hdl.handle.net/2268.2/9211

UNIVERSITÉ DE LIÈGE

MASTER THESIS

Gravitational waves signal analysis: Matched filtering, typical analyses and beyond

JANQUART Justin
In Partial Fulfilment of the
Requirements for the Degree of
Master in Space Sciences

Under the supervision of:
CUDELL Jean-René

Academic year 2019-2020

Student is not a container you have to fill
but a torch you have to light up.
—Albert Einstein
Ideas and Opinions, 1954

Acknowledgements

Contents

Introduction

The theory of general relativity as it is known today has not been written in one day. It needed the evolution of ideas on a long time scale. It is also the case for gravitational waves theory.

The first correct theory of gravity was proposed by Newton in his work *Philosophiae naturalis principia mathematica*, published in 1687 [1]. In this theory, gravitation is depicted as an attractive force acting between two massive objects. The biggest problem, already raised by Newton, is that it acts instantaneously without taking into account any distance effect between the two bodies. Nevertheless, at the time, it worked well for the description of the motion of celestial objects and it was kept for the next centuries. A first theory of relativity was proposed by the French physicist Henri Poincaré in 1900, and in 1905 he proposed gravity to be mediated by waves, which he already called *gravitational waves*. However, it is not the theory that remained famous over the years. Nevertheless, it was probably a source of inspiration for Einstein. The latter proposed in 1905 his theory of *special relativity*, which led to the surprising effect of time dilation and length contraction. He completed this theory ten years later to formulate his famous theory of *General Relativity*, still seen today as the best theory to describe gravitation. This theory describes gravity geometrically, as the manifestation of the space-time manifold. The curvature arises when a massive object is present, as well as when it has energy or momentum. Basically, this is described by Einstein's equations which make the link between the local curvature of space and time and the energy and the momentum present in the same region of space. In more technical terms, it gives the link between the Ricci tensor, the Ricci scalar and the metric on one side and the energy-momentum tensor on the other. This equation cannot, in fact, be solved analytically in many cases and has often to be solved numerically [2].

After his theory was completed, Einstein found the possibility to have the formation of gravitational waves. Those can be compared with the waves from the theory of electromagnetism (proposed by JC Maxwell in 1864 and published in 1865 [3]), where the acceleration of electric charges can produce electromagnetic waves. However, this analogy is not perfect. Indeed, for the latter theory, a dipolar emission is enough to obtain the wave. On the other hand, for gravity, the emission has to come from a higher order, the quadrupolar order. This result was not directly obtained by Einstein. Indeed, he first realized that because there are no positive and negative masses, the dipolar emission is not possible. In the case of electromagnetism, there are positive and negative charges. A dipole is then made of one positive and one negative charge and the emission arises from the relative motion of both charges. Clearly, this is not possible in the gravitational case. Nevertheless, Einstein was convinced of the possibility to have emission of gravitational waves. Therefore, he did some manipulations of his equations in order to have something looking like the equations of emission that Maxwell had found. In

order to obtain a solution, and due to the complexity of his equations, Einstein had to make several assumptions. It did not work until he changed his coordinate systems. However, his result found the existence of three different types of waves, which were called longitudinal-longitudinal, transverse-longitudinal and transverse-transverse by Herman Weyl [2].

Even if it looks like a win for the gravitational wave emission, Einstein's result raised a lot of scepticism and even criticism in the scientific community at the time. Indeed, he had assumed that the gravitational waves were emitted by bodies with a negligible gravitational field and that waves propagate in a flat and empty space-time. It was later found that solutions exist but Einstein made a mistake in his calculations. This was shown in 1922 by Eddington. He demonstrated that two out of the three wave-types that Einstein had found were spurious waves because these could have any speed and the latter depended on the coordinate system that was used. The error made by Einstein was his choice of coordinates. They were such that they induced waves by themselves and, therefore, the longitudinal-longitudinal and transverse-longitudinal waves were nothing more than flat space but seen by wavy coordinates. On the other hand, the transverse-transverse waves were proven by Eddington to travel at the speed of light in all the coordinate systems and were consequently not ruled out. Nevertheless, the non-existence of two of the three types of waves lead to a big distrust of the scientific community towards the gravitational wave emission. An extra confusion about this theory arose in 1936. After having moved to the Unites States, Einstein continued his study of gravitational waves with his younger collaborator Rosen. They claimed that the gravitational waves could not exist in his theory of General Relativity. This was first stated in a letter he wrote to Max Born. Later in the same year, the father of relativity submitted a paper, written with Rosen, to the journal *Physical Review* in which he disavowed the existence of the sought waves. However, the article was peer-reviewed by Howard Percy Robertson whose evaluation was quite negative. Therefore, the director of the review wrote back to Einstein asking him to respond to the negative comments that had been made. Angry, Einstein decided to publish his paper in another journal, where it was published without any questions. However, Einstein ended up being aware of the error he had made in his article and he modified it in order to find the solutions. In the end, although Einstein was convinced that there were gravitational waves, Rosen still stayed convinced that they were only a mathematical construction that had no physical meaning. Even if he believed in gravitational waves, Einstein was still not convinced that these would be detectable because of the faintness of the sources that were considered at the time, which were simple stars [2].

Due to the difficulties and doubts that existed around the theory of gravitational waves, it was disregarded by physicists until the late 1950's, when the conjugated works of Bondi, Pirani, Robinson and Trautman established the existence of the gravitational waves in a full theory of general relativity. Indeed, before their work, the emission of gravitational wave was only proven in simplified cases, such as quadrupoles or idealized systems.

One of the main reasons why Einstein did not believe in the detectability of gravitational waves was the faintness of the signal emitted by the most massive objects he could think of. Later on, the knowledge about the universe changed as well as the technology humankind could use. The sources became bigger when black holes and neutron stars were theorized. The precision of the instruments could also be increased. Therefore, the design for gravitational waves detectors started in the 1960's, only a decade after Einstein's death. At that time, already two types of detectors were thought of. The first are called *resonant-mass detectors*, where a solid object

resonates with the passage of the waves. These still exist but have not detected an event so far [4]. The second is the design followed by LIGO and Virgo, hence that of an interferometer with mirrors suspended and serving as test masses. The layout of these interferometers was more or less complete in the 1970's, when all the noise sources were identified by Weiss [5]. In the same period, Thorne worked on the theory of gravitational waves with a group he created at Caltech in 1968. They studied the sources as well as the noise that could be present in the detectors. They also developed the techniques to deal with the advanced detectors, where the quantum effects in the motion of the mirrors would be important due to the new precision level. In the 80's, several small prototypes were build. At the same time, some studies were made in order to have the plans to build a big detector: LIGO. The project was accepted and the 2 detectors were build in the 90's in Livingston and Hanford. The first searches were made from 2002 to 2005 without success. At the end of the 90's, Barish, the director of the LIGO collaboration, split the group in two: one responsible for the research and development of the detectors and one, the LIGO scientific collaboration, responsible for the data analysis as well as the scientific research. Another important step for the gravitational wave search is in 2007, when a collaboration was established between the American LIGO collaboration and the European Virgo collaboration, which also used an interferometer detector. So, the scientists of both collaborations joined their efforts in order to analyse the data, whereas the R&D part was kept separated. In 2008, the design for the advanced detectors was put in action. Both LIGO detectors were upgraded to the advanced phase for September 2015. Very fast after the start of this new phase, on September 14, the first gravitational wave signal was detected, confirming the existence and detectability of these waves. It is the GW150914 event, due to the merging of two black holes [6]. During this first observing run, the detectors would also detect two other black hole mergers. The second observing run started on November 30, 2016 and ended on August 31, 2017. There were more detections, and the Virgo detector joined the American detectors on August 1, 2017. This gave rise to the first triple detection, GW170814 [7], as well as the detection of the first neutron star binary merger, which is the GW170817 event. The latter was important because scientists were able to observe the electromagnetic counterpart of the event, especially with a gamma-ray burst, confirming the performance of the detectors and starting the area of gravitational waves astronomy [8, 9]. On October 3, 2017, Weiss, Barish and Thorne were awarded the Nobel Prize in physics for their contributions in the observation of gravitational waves [5]. Even if its history is related to that of the LIGO detectors, the Virgo detector has its own development history. The project was approved in 1993 by the CNRS and the INFN and its construction started three years later, in 1996. The EGO consortium, now responsible for the gravitational wave study in Europe, as well as the management of the detector (enhancement and data collection), was created in 2000. The construction of this detector, named after the Virgo constellation, ended in 2003. After that, several data collection phases were done to test the sensitivity and see if the concept worked. In particular, there was a data acquisition phase form 2007 to 2011 that was done in coincidence with the LIGO detectors. This led to the end of the *initial Virgo* project. After 2011, it was dismantled in order to be upgraded to the *Advanced Virgo* phase, which was aimed to be 10 times more sensitive than its predecessor. This upgrade was done in 2016 and the detector started to observe in August 2017 for the end of the second run, giving the first triple detection GW170814 [7], where the contribution of Virgo was essential to allow the sky localization of the event [2]. The third run started on April 1, 2019 and ended on March 27, 2020. It has the particularity that it should have been joined by the KAGRA observatory, a Japanese

cryogenic interferometer[1]. In each of these runs, the number of detections has increased [2].

Other plans also exist for the future of gravitational wave detection. A first step is the building of the Einstein Telescope, where 6 interferometers would be used: 3 cryogenic and 3 low temperature in a triangular shape [10]. In addition, there is also a project of a space telescope, called LISA for *Laser Interferometer Space Antenna*, which would enable to access ranges of gravitational waves not accessible on Earth due to the noise which is present on it [11]. But, with the increase of the number of detectors, as well as their sensitivity, the number of detections in each run is going to increase, and necessitate more data analysis. Indeed, one of the main problems that will arise is the difficulty to keep up with the data analysis. If the delay between detections decreases too much, it will become difficult to perform the analysis and find the signals hidden because the time needed to scan and process all the data will be too consequent. Therefore, it is important to find a more efficient way to deal with the data in order to find the signal. The goal of this work is to give an overview of the current analysis methods. In addition, it also looks at the influence of the parameters on the analysis. Moreover, we look at the behaviour of the analysis under some conditions, such as the presence of several signals or the detection of an event in the case where the full signal is not present. Both of these situations may happen in the future. The first can naturally arise when the length of the signal and the detection rate increase. The second case is studied from the perspective of the implementation of a multi-messenger observation of the events, with alerts sent to observe the event live in electromagnetic waves or neutrinos.

An important point is that the first gravitational wave detection, once it was confirmed and had gained the faith of the scientific community, led to a new era for astrophysics. Indeed, gravitational wave detectors would enable to observe new phenomena as well as give a new point of view on known ones, giving a new way to study them and learn more about them. In the past, the observation of space was done with photons. Even if the degree of interaction of the photon depends on its wavelength, it interacts quite substantially. Therefore, when this electromagnetic signal reaches the Earth, it is altered. Due to that, the scientists are blind to the furthest sources. On the other hand gravitational waves are not absorbed significantly by the matter of the Universe. So, the obscured objects can be observed thanks to them. In addition, all the information about the mechanism that has given rise to the gravitational wave is encoded in the latter, enabling the study of the objects and mechanisms at the origin of the wave. For example, gravitational wave astronomy enables to test whether the theory of general relativity stays consistent under extreme conditions, how matter behave in neutron stars and supernovae or the formation of black holes. Furthermore, it permits to look at cosmological models. Indeed, if the hypothesis of the stochastic formation of gravitational waves is confirmed, this new astronomical approach could enable to look back at periods that are not accessible with the photon-based astronomy.

In this work, we shall concentrate on the data analysis and the mathematical tools that are used. However, as the data come from the two LIGO and the Virgo detectors, it is important to understand their workings. The LIGO detectors are run by the American LIGO consortium. One is situated in Hanford (Washington) and the other in Livingston (Louisiana). On the other

---

[1]See https://gwpo.nao.ac.jp/en/ for more information

[2]The number of detections can be observed on the GraceDB website: https://gracedb.ligo.org/superevents/public/O3/

4

hand, Virgo is a European facility, built by the French CNRS and the Italian INFN and now operated the European Gravitational Observatory (EGO, still funded by the CNRS and the INFN). It is build in Cascina in Italy, near Pisa. All these detectors are based on the same scientific principle, which is that of the Michelson interferometer. The idea is to measure the stretching or contraction of space-time when a gravitational wave passes.

A gravitational wave deforms the space-time manifold by stretching or contracting it. Most often, when the calculations are done, the wave is represented as a plus and a cross polarization. These are represented in Fig.1, where we can see that there is a deformation of space that happens when the wave passes. It is what the detectors will measure, using a Michelson interferometer.
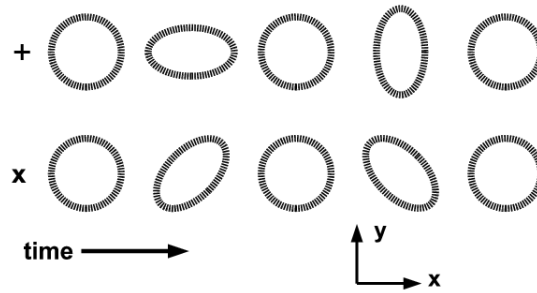
Figure 1: Evolution of the plus and cross polarization of a gravitational wave over time. The two arms of the interferometers are placed along the x and y axes. Taken from [12]

The interferometers measure distances with a high precision, $(\frac{1}{1000})^{th}$ the width of a proton. As can be seen in Fig.2, the interferometers in the detector are L-shaped, and the parts going from the splitting mirror to a reflective mirror are called the arms of the detector. The procedure is as follow: there is a laser emitting light towards the beam splitter. There, the beam of light is split into two different beams, each one going into a different arm and being reflected on a mirror at the end of it. These are the test masses, which are moved by the passage of the gravitational wave. The light then comes back and is collected at the end. When a signal is detected, hence when the mirrors move, the light intensity changes, depending on the relative stretching of the two arms. So, the interferometer gives an assessment of the relative difference in distance between the beam-splitting mirror and each test-mass mirror [4].

In order to have a better idea of what happens when a gravitational wave passes, one can imagine that the plus polarization arrives, with the plus shape being aligned on the arms of the detector. So, when the wave passes, the vertical arm is stretched whereas the other is contracted. A bit later, the detector takes its normal shape again before having the horizontal arm stretched and the other one compressed. These variations go on as long as the wave is passing, giving the detected signal. If one rotates the polarization of the wave by 45° with respect to the axis, giving a cross polarization, one sees that the same deformation will happen for both arms and no signal will be found. This shows that the detector is blind to some waves. It is another reason to have a network of detectors that have different orientations. Nevertheless, the two LIGO detectors are placed in an anti-parallel way and are, therefore sensitive to the same polarization of waves. They were built that way to allow an independent confirmation of waves detected in one of the

interferometers [5].

The description above is that of a simple Michelson interferometer. The gravitational wave detectors are considerably more complicated in order to achieve the high precision required. A first way to do so is by using very long arms (4 km for LIGO and 3 km for Virgo). This is not enough and other, more ingenious systems have to be put in action. An actual sketch of the detector can be found in Fig.2.
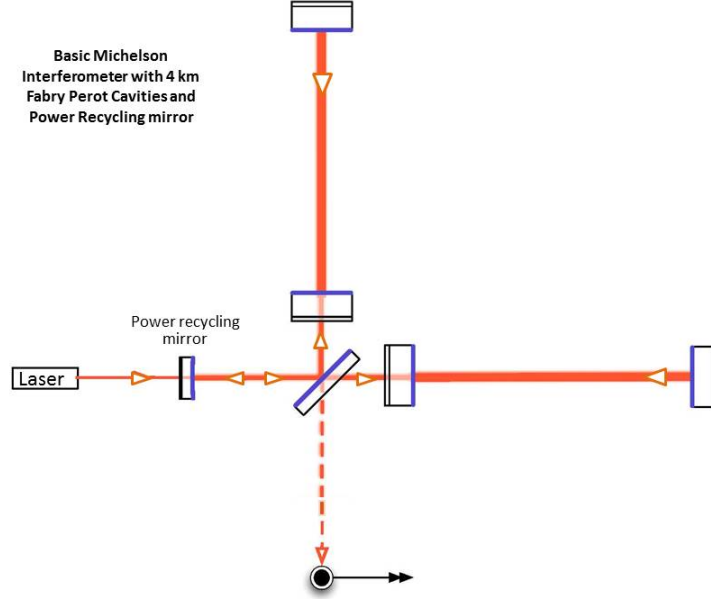
Figure 2: Representation of the LIGO detector. Taken from [13]

A first trick is the use of a *Fabry-Pérot* cavity, which is obtained by the addition of semi-reflecting mirrors after the splitting mirror. These reflect the light that comes back from the test-mass mirrors to the beam-splitter. Their basic purpose is to let the light travel several times in the arm cavity, increasing its effective length. On average, each laser beam goes 280 times in each arm of the detector, leading to an effective length of the arm of about 1120km for the LIGO detectors [14]. This system is also used in the Virgo and KAGRA detectors. A second trick is to use a *power boosted laser*, which increases the resolution of the detector by making the diffraction figure sharper. However, reaching such high power (750 kW for LIGO [14]) requires unconventional methods: additional mirrors are used, called *recycling mirrors*. These semi-reflecting mirrors are placed before the beam splitting mirror. So, the light is reflected back by the beam splitter, adding power to the laser. In fact, most of the photons coming back from the arms go to the power recycling mirror instead of the photodetector. Therefore, adding them back to the beam gives a substantial increase in the power of the laser [4].

Some other extra tools are used to make the detector more efficient. These are not really linked to the laser process itself but rather to the noises that can be substantial and hide the signal. For example, there is a seismic damping that is present in order to decrease the noise due to external activity. In the case of LIGO, there is a part of active damping system, with

seismometers recording the activity and the system actively reacting to it to avoid this noise, and a part of passive damping, which is made of a 4-stage pendulum that decouples the motion of the mirrors from the rest. For the Virgo detector, the system is a bit different, with a chain of suspended seismic filters and then the pendulum chain. In addition, both detector have their arms operating in a high vacuum. This has two main reasons: the air molecules can make noise and mask the small changes in distance between the mirrors and dust can lead to a scattering of the light which can be interpreted as a gravitational wave signal [13, 15].

In the previous section, we have focused on Virgo and LIGO because these are the detectors that have provided the data used for the analyses done in this work. However, other detectors exist or are in project. First, there is KAGRA. It has arms of 3 km and is located in Kamioka. Its main difference with the two previous detectors is that it is cryogenic. It works at $-250°C$ in order to avoid the thermal noise that is perturbing the mirrors. This detector started working at the end of the current O3 run but did not reach the expected precision yet [16]. Another detector that already exists and is working is GEO600. It is a laser interferometer that has arms of 600 m. In fact, it was operating before the other detectors. It is mainly used in order to test new technologies that can be implemented later on in the bigger versions. For example, it is improving the system of frequency-dependent squeezed light, which should be implemented in the other detectors later on [17]. A last plan is LIGO-India, which is a collaboration between India and the USA to build a copy of LIGO in India [18]. It would help for the implementation of a worldwide detector network, which is important to improve the sky localization. A map of this network is showed in Fig.3. It is important to note that all the detectors are not always working at the same time as there can be maintenances, log-off due to a local seismic activity that is too high . . . So, half of the time during O3, there were only two out of three detectors working. Increasing the number of detectors will enable to increase the precision that one has over the sky localization at a given time by ensuring that enough detectors would be logged at the same time. In addition, it may also allow a measurement of the gravitational wave polarization [19].
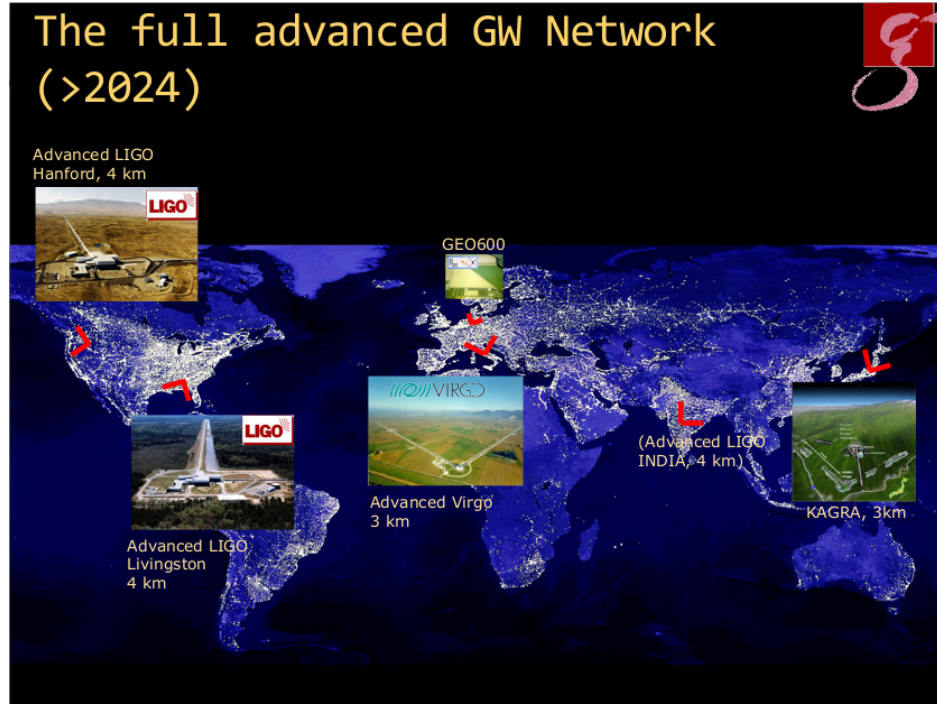
Figure 3: Map of the planned gravitational wave detector network. The angles represent the orientation of the detectors. Taken form [20]

In this work, we use the publicly available data, found on the *Gravitational Wave Open Science Center* web page[3]. They correspond only to the first and second runs of the detectors [9]. The analyses are done with the *PyCBC* package. This software package has been built by the LIGO scientific collaboration and Virgo. It contains different algorithms that enable to detect and analyse the coalescence of compact binaries (black holes and neutron stars). It is historically the package that has enabled to detect the first gravitational wave event GW150914 [21]. In the data analysis, there is the *PyCBC search* pipeline, which goes from the raw strain of the data to the parameters of the merger. In the work presented here, the full pipeline is not expanded, but we use the tools present in the package. In fact, we use it as a large Python library of functions that enable to retrieve different aspects of the mergers, with the possibility to filter data, to make templates of mergers and to do the matched filtering [22]. Although this pipeline has been proven successful, it is not the only one that exists or that is used by the collaboration [23]. For example, there is *GstLal*, which enables to do coalescence analysis, feature extraction with the identification of glitches, fake data generation, PSD generation . . . GstLal is also used in a pipeline for the gravitational wave search. It is a low-latency search which aims at the detection of the merger signal approximatively one minute after it peaks. This is important when looking for electromagnetic counterparts, as it is fast and enables to sent rapidly alerts for electromagnetic counterparts searches [24]. In addition to the software that can detect mergers, there are other ones that can detect other types of events, which are not based on matched filtering. A package illustrating this is *cWB*, used to identify transient events without knowing what they look like in advance. Therefore, when used in a pipeline, it identifies coherent events between different detectors and builds the gravitational wave signal

---

[3]see https://www.gw-openscience.org/

8

based on a maximum likelihood analysis. As a consequence, there is no need of filters and we can identify other events than the well-characterized mergers [25].

In the first chapter of this work, the method of *matched filtering* will be detailed. It presents the mathematical formalism behind the current searches for signals based on model templates. In the next section, the reader familiarizes with the *PyCBC* library. The first steps are the visualization and manipulation of the data in order to make them usable for the analysis. This is done for the GW170814 event, which is the first triple detection [7]. This event serves as an example for the complete work that follows.

In the third chapter, the significance of the event is studied. One sees how the use of several detectors helps to decide how likely it is to have a signal-to-noise ratio peak which is due to a gravitational wave event rather than noise. We also introduce statistics evaluating the significance of the event, such as the false alarm rate.

The following chapter looks at the determination of the parameters from the signal. It uses a minimization procedure and Bayesian statistics in order to find an estimation for the parameters that describe the event. A word about the possibility to find the error bars is also addressed but it is not computed in the frame of this work as it is too CPU-expensive.

In the fifth chapter, we analyse the influence of some parameters on the results. Some specific parameters defined and explained in the previous sections are looked at in more depth. A view of what they do and how they affect the modelisation of the data is given. This enables to understand the subtleties of the analysis.

In the sixth chapter, we consider the variation of the signal-to-noise ratio with the fraction of the gravitational signal that is taken into account. We look at what happens if only the inspiral is taken into account, or only a part of the ring-down, etc. and see if we could detect the signal early on and predict when the merger would happen. In addition, we also look at the effect of the non gaussian behaviour of the noise, as well as the influence of its amplitude.

In the last chapter, we look at the behaviour of the matched filtering technique when several signals are present in the same time window and overlap. This is done for three cases: two binary black hole systems, one binary black hole and one binary neutron star and two binary neutron star systems. This type of behaviour could be encountered in the forthcoming years, as the length of the signals and their detection rate increase.

All along this work, the numerical tools are explained under two different point of views. The first one is the practical computation of the different quantities that characterize the signal and their interpretation with PyCBC. The second is to look at the mathematics behind the tools in order to understand them clearly. It is also important to note that the aim of this work is to give an overview of the analysis of an event and that the procedures used in practice by the LIGO-Virgo collaboration are based on this but are often more complicated. In addition to this overview, this work shows some possible future problems and evolutions of the gravitational data analysis, while setting up some tools in order to make the computation feasible on less powerful devices. The ideas explored here are a good preliminary search about these behaviours, while opening the door to further studies.

The codes used for this work are available on the Github address: `https://github.com/lemnis12?tab=repositories`

Chapter 1

Theory of matched filtering

1.1 Importance of this technique in the detection of gravitational waves

The matched filtering technique is known to be the best linear filter to extract a signal of known form swamped in stationary gaussian noise [26]. This can be done even if some parameters of the signal are unknown, such as its amplitude or its exact reception time. This process is in fact able to detect the signal as well as to characterize these unknowns. The technique applied here uses the difference between the characteristics of the signal and the noise. In the case of the detection of gravitational waves, it is used with the additional hypothesis that the noise is second order stationary. In other words, it is a gaussian random process where the expected value of the power is assumed to be the same for each frequency, even if, in reality, its realization can be different from one frequency to the next. This process of matched filtering was initially described by *Wainstein* and *Zubakov* in their book *Extraction of signals from noise* [27]. The developments in the next sections are inspired by this book and adapted to the gravitational wave analysis context.

In this chapter, the theoretical aspect of the matched filter is developed. It starts with the presentation of the general theoretical concepts and shows the signal-to-noise ratio which is maximized at the end of the detection process in the specific case of gravitational waves.

1.2 Basic concepts of the filtering process

This section develops some generalities about the mathematical tools and the processes used in the theory of matched filtering. In the study of gravitational waves for compact object binary mergers, the shape of the signal is known and the goal is to determine if and where it is present in the observed signal, before finding which are the parameters of the event at the origin of the waves (such as the masses of the objects, the distance, the spins, etc.). Therefore, at the input stage of the filter, two cases can occur. First, the signal is present and the input is thus a

superposition of the noise and the gravitational wave. In the second case, the input is only made from noise. So, if $h(t)$ is the signal from the gravitational wave and $n(t)$ that from the noise, the first case corresponds to the expression $h(t) + n(t)$ and the second case to $n(t)$. In order to see whether the signal is present, a linear filter is used, i.e. it applies a linear operation on the input signal. So, the signal enters the filter and goes out after a transformation. If the linear filter is written as $\mathscr{K}$ and the total input signal as $i(t)$, then the output signal is $o(t) = \mathscr{K}\left[i(t)\right]$.

Different types of filters can be used. They have their own characteristics and correspond to different moments of the search for gravitational waves:

- *type I filter:* the time-dependent function $i(t)$ is recorded for a certain interval of time, $t_0 \leq t \leq t_f$. It is then transformed by a mathematical operation and gives back another function. It is, for example, what is done by a computer when it records the data, processes them and, finally, gives them back under the form of a curve or a table. This type of filter has the advantage to make use of the complete data sequence provided and to suppress the noise more efficiently. It corresponds to the offline treatment of the data. In this case, the processing is done after the detectors are turned off and there is an access to the whole time series, before and after the suspected event. It allows a more precise inference on the parameter characterization of the event. What is done, for example, is to use the parts of the data when the gravitational wave signal is not present in order to model the noise [22].

- *type II filter:* the recording and delivering of the data are done at the same time. The process is done continuously and the output data at a given moment depend only on the data obtained previously and at that exact moment. This filter has the advantage to deliver more rapidly the output data than the other type of filter. The filter here can have a finite or infinite memory, which means that the past data used for its transformation can be found in a maximum time interval T, which can be finite or infinite. When the memory has a finite range in the past, the filter is sometimes called a *type III filter*. This corresponds to the online treatment, done directly while acquiring the data and is named the low-latency search. It is the first analysis made and used to see if a gravitational wave is present [22].

For a type I filter, the relation between the input function ($i(t)$) and output function ($o(t)$) can be written as:
$$\mathscr{K}\left(i\right) = o(t) = \int_{-\infty}^{\infty} k(t')i(t - t')dt' \tag{1.1}$$

or, equivalently,
$$o(t) = \int_{-\infty}^{\infty} k(t - t')i(t')dt',$$

where we assumed $t_0 \to -\infty$ and $t_f \to +\infty$. $k(t)$ corresponds to the response of the function to an impulsion, which can mathematically be written under the form of a delta function. This can be seen by replacing the input function by the delta function in Eq.((1.1)).

In the expressions above, the function $k(t)$ is a weighting function representing the filter, called the *impulse response*. Here, one clearly sees that the output of the filter at a given time t depends both on the past and on the future times through $i(t')$ with $t' < t$ and $i(t')$ with $t' > t$. For

each of the considered times, the $o(t)$ function is weighted by the $k(t-t')$ function, depending on the time spacing. The form above is that of a *stationary* or *time-invariant* filter. If it is a time varying filter, then the weighting function is not only dependent on the time spacing but also on both times individually. In this case, the impulse response function is written as $k(t, t')$.

When we have a type II or a type III filter, the expression is the same but the limits of the integrals only cover past times. The lower bound of the integral is then $-\infty$ for the first case and $-T$ for the second, where T is called the memory of the filter.

Let us define some useful quantities characterizing the input function:

- the *average (or mean) value* of the function is denoted $\bar{i}(t)$. It corresponds to an *ensemble average* and is done over all the values that the function can take for the time t.

- the *correlation function*, also called the *autocorrelation function*, is defined as

$$R_i(\tau) = \overline{[i(t) - \bar{i}(t)][i(t-\tau) - \bar{i}(t-\tau)]}. \tag{1.2}$$

  When $\bar{i} = 0$, $R_i(\tau) = \overline{i(t)i(t-\tau)}$. This characterizes the statistical relation between the values of the function i between the times t and $t-\tau$ ($\tau > 0$ or $\tau < 0$). When the values of the function evaluated at those two times are independent, the mean value of the product is equal to the product of the mean values, which gives zero. So, $R_i(\tau) = 0$. Conversely, $R_i(\tau) = 0$ implies that $i(t)$ and $i(t-\tau)$ are statistically independent.

- the *correlation coefficient* is another important characteristic quantity for the filtering processes. It is given by $\frac{R_i(\tau)}{R_i(0)}$.

- the *cross-correlation function* for two processes $h(t)$ and $n(t)$ is defined as $R_{hn}(\tau) = \overline{h(t)n(t-\tau)}$. It expresses the statistical relation existing between the two processes at two different moments in time. This function is null when both functions are independent. In the case of gravitational waves, the functions represent the signal due to the gravitational waves ($h(t)$) and the signal due to noise ($n(t)$), which are the two components that can make up the input signal.

For the following developments, the average values of the functions are assumed to be zero. This is not a loss of generality. Indeed, if the function is such that $\bar{i} \neq 0$, a new function Δi can be defined as $\Delta i = i(t) - \bar{i}$, which has a zero mean value. The operations are then made on the latter function. This redefinition can also be performed on both the gravitational wave signal and the noise individually. In particular, for the second case, the function obtained after the average has been subtracted corresponds to the variation of the noise around its mean value, which is the most interesting quantity.

As it is often the case in time series analysis, the different functions are considered in the frequency domain instead of the time domain. The mapping from time- to frequency-dependent functions is made through the use of a *Fourier transform*. The inverse operation, enabling to go from the frequency to the time domain is the *inverse Fourier transform*. In this work, for any time-dependent function $i(t)$, its Fourier transform is noted with a rounded capital letter,

hence $\mathscr{I}(\omega)$. In fact, ω does not corresponds to the frequency itself but rather to the *angular frequency*, which is equal to $2\pi f$, where f denotes the classical frequency.

Formally, the Fourier transform is defined as:

$$\mathscr{I}(\omega) = \int_{-\infty}^{\infty} e^{-i\omega t} i(t) dt \tag{1.3}$$

and the inverse transformation is:

$$i(t) = \frac{1}{2\pi} \int_{-\infty}^{\infty} e^{i\omega t} \mathscr{I}(\omega) d\omega. \tag{1.4}$$

1.3 Characteristic functions

In this section, functions characterizing the analysed data and the filter are introduced. First, we define the *power spectral density (PSD)* , which is the Fourier transform of the auto-correlation function (1.2) of the input signal. Consequently, it is noted $\mathscr{R}_i(\omega)$. This function gives the power of the signal for a fixed angular frequency. So, when the signal presents a periodicity at a given angular frequency, its PSD has a larger value when evaluated at that frequency.

The second characteristic function is called the *transfer function* of the filter and is noted $\mathscr{K}(\omega)$. As the notation implies, it is the Fourier transform of the impulse response of the filter $k(t)$ of Eq.(1.1). It corresponds to the Green function of the $\mathscr{I}(\omega)$ function.

In addition, as can been seen from Eq.(1.1), if the input function takes the form $i(t) = i_\omega e^{i\omega t}$, then the output function has the expression

$$o(t) = \int_{-\infty}^{\infty} k(t') i_\omega e^{i\omega(t-t')} dt' = i_\omega e^{i\omega t} \int_{-\infty}^{\infty} k(t') e^{i\omega t'} dt' = i_\omega e^{i\omega t} \mathscr{K}(\omega). \tag{1.5}$$

This shows that the output function corresponds to the product of the particular input function and the Fourier transform of the impulse response function, hence the transfer function of the filter. Consequently, the $\mathscr{K}(\omega)$ function is the ratio of the complex amplitudes of the output and input. In addition, the quantities that have a physical meaning are the real parts of the complex quantities. These represent the sinusoidal oscillation in the frequency domain at the input and the output of the filter.

1.4 Khinchin's theorem

Khinchin's theorem is a general theorem used in filtering theories [28]. It enables to have a better understanding of the power spectral density and is useful for the proof of matched filtering. It is used to define the noise characteristics that are used in the signal-to-noise ratio.

By the assumption of stationarity, the autocorrelation function of the input function ($R_i(\tau)$) is an even function of time. Therefore, the power spectral density ($\mathscr{R}_i(\omega)$) is an even function

of the angular frequency. So, for a stationary process, we have $R_i(\tau) = R_i(-\tau)$, and we can compute

$$\mathscr{R}_i(\omega) = \int_{-\infty}^{\infty} R_i(\tau)\cos(\omega\tau)d\tau = 2\int_{0}^{\infty} R_i(\tau)\cos(\omega\tau)d\tau. \tag{1.6}$$

As a consequence, one has the relation $\mathscr{R}_i(\omega) = \mathscr{R}_i(-\omega)$, which translates to the fact that this function is even. The relation here is build in an idealized case, which is not totally in agreement with the gravitational waves because the latter are not stationary.

Khinchin's theorem, valid in all generality, states that the function $\mathscr{R}_i(\omega)$ is non-negative for any process $i(t)$:

$$\mathscr{R}_i(\omega) \geq 0.$$

In addition, the product $\mathscr{R}_i(\omega)d\omega$ is proportional to the intensity of the oscillations at the output of a narrowband filter that lets pass the frequency range $[\omega, \omega + d\omega]$ when the $i(t)$ function is applied at the input.

Because the autocorrelation function is the Fourier transform of the power spectral density, its value for $\tau = 0$ is

$$R_i(0) = \overline{i^2(t)} = \frac{1}{2\pi}\int_{-\infty}^{\infty} \mathscr{R}_i(\omega)d\omega. \tag{1.7}$$

This corresponds to the *intensity* (or *average power*) of the input signal. In Eq.(1.7), the integrand depends on the angular frequency ω.

Proof of the theorem:

The function processed through the linear filter is noted $i(t)$. If $k(t)$ is the impulse response of the filter, the function at the output of the filter is given by Eq.(1.1).

It has an average power calculated as:

$$\overline{o^2(t)} = \int_{-\infty}^{\infty}\int_{-\infty}^{\infty} k(t')k(t'')\overline{i(t-t')i(t-t'')}dt'dt'' \tag{1.8}$$

$$= \int_{-\infty}^{\infty}\int_{-\infty}^{\infty} k(t')k(t'')R_i(t'-t'')dt'dt'' \tag{1.9}$$

$$= \frac{1}{2\pi}\int_{-\infty}^{\infty}\int_{-\infty}^{\infty}\int_{-\infty}^{\infty} k(t')k(t'')\mathscr{R}_i(\omega)e^{i\omega(t'-t'')}dt'dt''d\omega \tag{1.10}$$

$$= \frac{1}{2\pi}\int_{-\infty}^{\infty} \mathscr{R}_i(\omega)\int_{-\infty}^{\infty} k(t')e^{i\omega t'}dt'\int_{-\infty}^{\infty} k(t'')e^{i(-\omega t'')}dt''d\omega \tag{1.11}$$

$$= \frac{1}{2\pi}\int_{-\infty}^{\infty} \mathscr{K}(\omega)\mathscr{K}(-\omega)\mathscr{R}_i(\omega)d\omega. \tag{1.12}$$

In addition, because $k(t)$ is a real function, one has the relation $\mathscr{K}(-\omega) = \mathscr{K}^*(\omega)$. As a consequence, one also has $\mathscr{K}(\omega)\mathscr{K}(-\omega) = |\mathscr{K}(\omega)|^2$. So, the final expression for the average power is:

$$\overline{o^2(t)} = \frac{1}{2\pi}\int_{-\infty}^{\infty} |\mathscr{K}(\omega)|^2\mathscr{R}_i(\omega)d\omega.$$

This expression links the intensity of the oscillations at the output with the transfer function of the filter and the spectral density of the input.

If we then consider a filter with a transfer function defined as:

$$\mathscr{K}(\omega) = \begin{cases} 1 & \text{for } \omega \in [\omega, \omega + d\omega] \text{ and } \omega \in [-\omega - d\omega, -\omega] \\ 0 & \text{otherwise} \end{cases} \tag{1.13}$$

then,

$$\overline{o^2(t)} = \mathscr{R}_i(\omega)\frac{d\omega}{2\pi} + \mathscr{R}_i(-\omega)\frac{d\omega}{2\pi} = 2\mathscr{R}_i(\omega)\frac{d\omega}{2\pi}. \tag{1.14}$$

Because $\overline{o^2(t)}$ is non-negative, one has that $\mathscr{R}_i(\omega) \geq 0$ and the inequality is proven.

From Eq.(1.14), a physical meaning of the power spectral density can be obtained. Indeed, ω is the angular frequency, and the frequency is given by $\frac{\omega}{2\pi}$. Therefore, the power spectral density can be seen as the average power per unit of frequency, when the positive and negative frequencies are considered.

If, the input signal of the filter is made of the addition of the gravitational wave signal to the noise, written $i(t) = n(t) + h(t)$, the cross-correlation functions of the two processes present in the total signal are $R_{hn}(\tau) = \overline{h(t)n(t-\tau)}$ and $R_{nh}(\tau) = \overline{n(t)h(t-\tau)}$. Their Fourier transforms are function of ω written $\mathscr{R}_{hn}(\omega)$ and $\mathscr{R}_{nh}(\omega)$. In order to obtain the interpretation of the power spectral density, some properties of the cross-correlation function and of its Fourier transform are needed. First, $R_{hn}(\tau)$ and $R_{nh}(\tau)$ obey the relation:

$$R_{hn}(\tau) = R_{nh}(-\tau). \tag{1.15}$$

Indeed,

$$R_{nh}(-\tau) = \overline{n(t)h(t+\tau)} = \overline{n(t-\tau)h(t)} = R_{hn}(\tau).$$

Taking the Fourier transform of Eq.(1.15) and using the linearity of this operation, one directly finds the relation:

$$\mathscr{R}_{hn}(\omega) = \mathscr{R}_{nh}(-\omega). \tag{1.16}$$

A last useful property to mention is that, since the cross-correlation function is real and since $\mathscr{R}_{hn}(\omega)$ is related to it by a Fourier transform, the $\mathscr{R}_{hn}$ function obeys the relation

$$\mathscr{R}_{hn}(-\omega) = \mathscr{R}_{hn}^*(\omega)$$

.

Using the different properties above and applying them to the case of the input function, we have:

$$R_i(\tau) = \overline{[h(t) + n(t)][h(t-\tau) + n(t-\tau)]} \tag{1.17}$$
$$= R_h(\tau) + R_n(\tau) + R_{hn}(\tau) + R_{nh}(\tau). \tag{1.18}$$

The power spectral density of the total input signal is found by Fourier transform of the auto-correlation function:

$$\mathscr{R}_i = \mathscr{R}_h(\omega) + \mathscr{R}_n(\omega) + \mathscr{R}_{hn}(\omega) + \mathscr{R}_{nh}(\omega)$$
$$= \mathscr{R}_h(\omega) + \mathscr{R}_n(\omega) + 2\Re(\mathscr{R}_{hn}(\omega)). \tag{1.19}$$

The first two terms of the Eq.(1.19) correspond to the individual spectral densities of the noise and of the gravitational wave signal. They correspond to the spectral density of the uncorrelated part of the signal. The last term is called the *interference intensity* and represents the intensity that arises because of the correlation of the two parts of the input. Consequently, it disappears when they are independent. This shows the entanglement that can exist between the noise and the signal, leading to some eventual complications.

1.5 Detection of a signal with a known form

Now that the useful general tools have been introduced, the more specific case of the detection of a signal with a known form swamped by stationary noise can be discussed. This corresponds to the method that is used in the case of matched filtering, in particular for the detection of gravitational waves. The gravitational wave signal ($h(t)$) has a general form that is known and that depends on several parameters. The final aim is to determine with the most precision possible these parameters once the signal has been discriminated from the random noise it is mixed with. In this section, we look at what happens when this signal passes through a linear filter characterized by a transfer function $\mathscr{K}(\omega)$, and what this function should be.

For the input signal $i(t)$, there are two possibilities. The first one is that there is an event that has triggered a gravitational wave and that the signal is present and mixed with noise. Thus, the signal is written $i(t) = h(t) + n(t)$. The alternative case is the one where there is no useful signal and the input is only due to random noises. So, $i(t) = n(t)$. The goal is to find in which case the input function is present and to find the values of the parameters that characterize it. The signal is assumed to be entirely known. That means that we haves a template that is a model for the signal. The different models that can be used are built using the post-newtonian approximation, the effective one-body problem and numerical relativity [29, 30, 31, 32]. The signal can be represented in the frequency domain through a Fourier transform. In addition, since the filter is supposed to be linear, the total output signal is equal to the sum of each of its parts modified individually by the filter. So, the input of the filter is

$$i(t) = h(t) + n(t) \tag{1.20}$$

where $n(t)$ represents the noise and $h(t)$ the gravitational wave signal. The noise being a random process, its Fourier transform is replaced by its average power, as has been done in the proof of Khinchin's theorem. We assume that the average of the noise is zero. Therefore, by linearity of the Fourier transform, $\mathscr{N}(\omega)$, the Fourier transform of the noise, has also an average that is equal to zero. In addition, the noise is assumed to be a second order stationary process, which means that its first and second order statistical moments are finite. As a consequence, $\overline{n(t)n(t')}$ depends only on $t - t'$ and, if $\mathscr{R}_n(\omega)$ is the *two-sided noise power spectrum*, we have:

$$\overline{n^2(\omega)} = \frac{1}{2\pi} \int_{-\infty}^{+\infty} \mathscr{R}_n(\omega) d\omega. \tag{1.21}$$

When one does matched filtering in the context of gravitational waves, one tries to look if a given waveform is present in the signal. This means that $h(t)$ is known. It can take the generic

form, called the *binary inspiral chirp waveform* [33]:

$$h(t) = \frac{D}{d}\left[\cos(\phi)W_c(t-t_0) + \sin(\phi)W_s(t-t_0)\right] \tag{1.22}$$

This waveform depends on four different parameters:

- W_c and W_s: time dependent functions corresponding to templates of waveforms when the binary system is perpendicular to the line-of-sight of the detector and at a distance D;

- d: the effective distance between the detector and the source, without taking the inclination into account;

- t_0: a reference time, often taken as the time of arrival of the signal;

- ϕ: a phase which depends on the orbital phase of the merger as well as the angle between the plane of the binary system and that of the interferometer;

- D: is the canonical distance of the source, which corresponds to the distance of the merger when it is optimally oriented and produces the waveforms W_c and W_c.

Another simpler case that could be considered is that the phase ϕ defined above is known and included in the template W. In that case, the waveform takes the simpler form

$$h(t) = \frac{D}{d}W(t-t_0). \tag{1.23}$$

The value of the canonical distance can be used in order to normalize the waveform W as the product $DT(t)$ is independent of D, as $W \propto \frac{1}{D}$ [33].

In order to obtain a more compact presentation of the matched filter, one uses a Hermitian inner product, defined for any two complex functions A and B as:

$$\langle A|B \rangle = \int_{-\infty}^{\infty} \frac{A^*(\omega)B(\omega)}{\mathscr{R}_n(\omega)}d\omega. \tag{1.24}$$

In fact, for a real detector, the detection band is not infinite, as is assumed in this expression. The restriction to the real frequency band of the detector can be obtained by letting $\mathscr{R}_n \to \infty$ for the angular frequencies that are not within the range of the detector. By doing this, the value of the integral out of the frequency-band goes to zero, allowing to take the real frequency range into account.

The matched filter is the one that maximizes the signal over noise ratio. So, the transfer function of the filter can be written as:

$$\mathscr{K}(\omega) = \frac{\mathscr{C}^*(\omega)}{\mathscr{R}_n(\omega)}, \tag{1.25}$$

where $\mathscr{C}$ is an unknown function for the moment, and its output is

$$z \equiv \int_{-\infty}^{+\infty} \frac{\mathscr{C}^*(\omega)\mathscr{I}(\omega)}{\mathscr{R}_n(\omega)}d\omega = \langle \mathscr{C}|\mathscr{I} \rangle. \tag{1.26}$$

Based on these notations, the expected output of the filter is then written as

$$\overline{z} = \int_{-\infty}^{+\infty} \frac{\mathscr{C}^*(\omega)\mathscr{H}(\omega)}{\mathscr{R}_n(\omega)} d\omega = \langle \mathscr{C}|\mathscr{H}\rangle, \tag{1.27}$$

where $\mathscr{H}$ corresponds to the Fourier transform of the gravitational wave template.

Because $\overline{n(t)n(t')}$ is only dependent on $t - t'$, we have

$$\overline{\mathscr{N}(\omega)\mathscr{N}^*(\omega)} = \frac{1}{2\pi}\mathscr{R}_n(\omega)\delta(\omega - \omega'), \tag{1.28}$$

where $\delta(\omega - \omega')$ is the Dirac distribution. Based on the relation (1.28), the expected value of the square of z is given by

$$\overline{z^2} = \langle \mathscr{C}|\mathscr{C}\rangle + \langle \mathscr{C}|\mathscr{H}\rangle^2. \tag{1.29}$$

We define δz, the difference between the output of the filter and its expected output, hence

$$\delta z = z - \overline{z}. \tag{1.30}$$

The error on the measurement of z due to noise is then

$$\sqrt{\overline{(\delta z)^2}} = \sqrt{\overline{(z - \overline{z})^2}} = \sqrt{\overline{z^2} - (\overline{z})^2} = \langle \mathscr{C}|\mathscr{C}\rangle^{\frac{1}{2}}. \tag{1.31}$$

The optimal filter should maximize the ratio of the signal over the noise and can be defined based on the quantities introduced above. What is known is the gravitational waveform. Therefore, the optimal filter maximizes the signal-to-noise ratio (SNR):

$$\rho = \frac{\overline{z}}{\sqrt{\overline{(\delta z)^2}}} = \frac{\langle \mathscr{C}|\mathscr{H}\rangle}{\langle \mathscr{C}|\mathscr{C}\rangle^{\frac{1}{2}}}. \tag{1.32}$$

This expression corresponds to the expected filter output divided by its uncertainty due to noise [33]. The error on z comes from the noise that is present on the detector, which is a random process that can only be statistically described.

The Hermitian product defined by Eq.(1.24) respects the Cauchy-Schwarz relation. Therefore, we have:

$$|\langle \mathscr{C}|\mathscr{H}\rangle|^2 \leq \langle \mathscr{H}|\mathscr{H}\rangle \langle \mathscr{C}|\mathscr{C}\rangle. \tag{1.33}$$

Proof of the Cauchy-Schwarz inequality:

We define $\lambda \in \mathbb{C}$ as

$$\lambda = \frac{\langle \mathscr{C}|\mathscr{H}\rangle}{\langle \mathscr{H}|\mathscr{H}\rangle}. \tag{1.34}$$

This can be done because if $\mathscr{H}$ is equal to zero, the relation (1.33) is trivially zero. Therefore,

we assume $\mathscr{H} \neq 0$, and we have

$$0 \leq |\langle \mathscr{C} - \lambda\mathscr{H} | \mathscr{C} - \lambda\mathscr{H} \rangle| \tag{1.35}$$
$$\leq \langle \mathscr{C} | \mathscr{C} \rangle - \langle \lambda\mathscr{H} | \mathscr{C} \rangle - \langle \mathscr{C} | \lambda\mathscr{H} \rangle + \langle \lambda\mathscr{H} | \lambda\mathscr{H} \rangle \tag{1.36}$$
$$\leq \langle \mathscr{C} | \mathscr{C} \rangle - \lambda\langle \mathscr{H} | \mathscr{C} \rangle - \lambda^*\langle \mathscr{C} | \mathscr{H} \rangle + \lambda\lambda^*\langle \mathscr{H} | \mathscr{H} \rangle \tag{1.37}$$
$$\leq \langle \mathscr{C} | \mathscr{C} \rangle - \frac{\langle \mathscr{C} | \mathscr{H} \rangle\langle \mathscr{C} | \mathscr{H} \rangle^*}{\langle \mathscr{H} | \mathscr{H} \rangle} - \frac{\langle \mathscr{C} | \mathscr{H} \rangle\langle \mathscr{C} | \mathscr{H} \rangle^*}{\langle \mathscr{H} | \mathscr{H} \rangle} + \frac{\langle \mathscr{C} | \mathscr{H} \rangle\langle \mathscr{C} | \mathscr{H} \rangle^*\langle \mathscr{H} | \mathscr{H} \rangle}{\langle \mathscr{H} | \mathscr{H} \rangle^2} \tag{1.38}$$
$$\leq \langle \mathscr{C} | \mathscr{C} \rangle - \frac{|\langle \mathscr{C} | \mathscr{H} \rangle|^2}{\langle \mathscr{H} | \mathscr{H} \rangle} - \frac{|\langle \mathscr{C} | \mathscr{H} \rangle|^2}{\langle \mathscr{H} | \mathscr{H} \rangle} + \frac{|\langle \mathscr{C} | \mathscr{H} \rangle|^2}{\langle \mathscr{H} | \mathscr{H} \rangle} \tag{1.39}$$

The last line can then be rewritten as

$$|\langle \mathscr{C} | \mathscr{H} \rangle|^2 \leq \langle \mathscr{C} | \mathscr{C} \rangle\langle \mathscr{H} | \mathscr{H} \rangle, \tag{1.40}$$

which corresponds to the Cauchy-Schwarz inequality, as shown in Eq.(1.33).

The Cauchy-Schwarz relation (1.33) leads to an upper limit on the output of the filter. Therefore, we look at the conditions to fulfil in order to have the equality. This happens when

$$\mathscr{C} - \lambda\mathscr{H} = 0 \iff \mathscr{C} = \lambda\mathscr{H}. \tag{1.41}$$

This means that the maximum ratio is found when the transfer function of the filter is a multiple of the Fourier transform of the gravitational wave signal that is present in the detector. So, the optimal matched filter is a time reversed copy of the template but reweighed by the expected noise spectrum. The optimal filter takes the mathematical expression:

$$\frac{\mathscr{C}^*(\omega)}{\mathscr{R}_n(\omega)} = C\frac{\mathscr{H}^*(\omega)}{\mathscr{R}_n(\omega)}, \tag{1.42}$$

where C is a constant.

If we impose the normalization $\langle \mathscr{C} | \mathscr{C} \rangle = 1$, the optimal filter takes the form:

$$\mathscr{C}(\omega) = \frac{\mathscr{H} e^{-i\omega t_0}}{\sqrt{\langle \mathscr{H} | \mathscr{H} \rangle}}. \tag{1.43}$$

Using these notations, the output of the filter is given by

$$z(t_0) = \int_{-\infty}^{+\infty} \frac{\mathscr{I}(\omega)\mathscr{H}^*(\omega)e^{i\omega t_0}}{\mathscr{R}_n(\omega)} d\omega. \tag{1.44}$$

This corresponds to a Fourier transform, making that quantity easy to compute when the waveform is known (with a fast Fourier transform for example), whichever form it has.

As an example, we can consider the case where the waveform is given by Eq. (1.23) and show the values of the quantities defined above [33]. First, the expected output is

$$\bar{z} = \frac{D}{d}\langle \mathscr{C} | \mathscr{T} e^{i\omega t_0} \rangle, \tag{1.45}$$

where $\mathscr{T}$ is the Fourier transform of the T function present in the waveform.

The expectation value of the square of z is given by

$$\overline{z^2} = \langle \mathscr{C} | \mathscr{C} \rangle + \left(\frac{D}{d} \right)^2 \left(\langle \mathscr{C} | \mathscr{T} e^{i\omega t_0} \rangle \right)^2. \tag{1.46}$$

If we define

$$\mathscr{A}(\omega, t_0) = \frac{D}{d} \mathscr{T}(\omega) e^{-i\omega t_0}, \tag{1.47}$$

the SNR can be written as

$$\frac{\overline{z}}{\sqrt{(\overline{\delta z^2})}} = \frac{\langle \mathscr{C} | \mathscr{A} \rangle}{\langle \mathscr{C} | \mathscr{C} \rangle^{\frac{1}{2}}}. \tag{1.48}$$

Note that this expression in invariant with respect to the addition of a multiplicative constant. So, it does not change if we do $\mathscr{C} \to K\mathscr{C}$ with $K \in \mathbb{R}$.

If we impose the normalization condition $\langle \mathscr{C} | \mathscr{C} \rangle = 1$, $\mathscr{C}$ is given by the expression:

$$\mathscr{C}(\omega) = \frac{1}{\sqrt{\langle \mathscr{T} | \mathscr{T} \rangle}} \mathscr{T}(\omega) e^{-i\omega t_0}. \tag{1.49}$$

In this case, the output of the filter and the SNR are equal.

Chapter 2

Visualization of the event present in the data

2.1 Introduction

In this section, the tools for the acquisition of the data and the visualization of a gravitational wave event are presented. The software package used is *PyCBC*, which is specialized in the study and characterization of binary coalescences. It can be used in order to see if a merger is present and to study the objects that give rise to the signal [21].

The event chosen for this overview, and the following chapters, is *GW170814*, which is the first triple detection , found by the two LIGO detectors as well as the Virgo detector. This event was detected first in the LIGO-Livingston detector on the 14th of August 2017 at 10:30:43 UTC. Shortly after ($\sim$ 8ms and $\sim$ 14ms, respectively), the peak was also seen in the LIGO-Hanford and Virgo detectors. At the origin of this event, there is the merger of two black holes, of masses $30.5^{+5.7}_{-3.0} M_\odot$ and $25.3^{+2.8}_{-4.2} M_\odot$. The phenomenon took place at a luminosity distance[1] of $540^{+130}_{-210} Mpc$ [7]. The numerical codes used here are based on the tutorials provided by the *LIGO Open Science Collaboration (LOSC)*[2].

Table (2.1) gives all the parameters that are available for the GW170814 event. Most of them have names that are speaking for themselves and do not need to be further detailed. Others are more specific or less well known. The first such parameter is the *effective spin*. This quantity corresponds to the ratio of the spin of each black hole weighed by its mass over the sum of the two masses, projected onto he angular momentum:

$$\chi_{eff} = \frac{\frac{\mathbf{S_1}}{m_1} + \frac{\mathbf{S_2}}{m_2}}{m_1 + m_2} \cdot \hat{\mathbf{L}}, \tag{2.1}$$

where m_1 and m_2 are the masses of the black holes, $\mathbf{S_1}$ and $\mathbf{S_2}$ are their spins normalized by

---

[1]The luminosity distance is a distance defined based in the relationship between the bolometric flux (S) and the bolometric luminosity L as: $D_L = \sqrt{\frac{L}{4\pi S}}$ [34]

[2] which can be found at the address: `https://www.gw-openscience.org/static/workshop1/course.html`

the maximum spin of a Kerr black hole ($\frac{GM^2}{c}$) and $\hat{\mathbf{L}}$ is the direction of the angular momentum. This parameter is introduced because, nowadays, the spin of the individual objects cannot be completely determined by the detectors, even if this information is encoded in the wave. On the other hand, the effective spin can. It is also a constant of motion (at least to the second post-Newtonian order), which makes it a good measure to characterize the full coalescence [35].

The *chirp mass* is also a parameter that is proper to the theory of gravitational waves. It is related the masses of the black holes by the relation [36]:

$$M_{chirp} = \frac{(m_1 m_2)^{\frac{3}{5}}}{(m_1 + m_2)^{\frac{1}{5}}}, \tag{2.2}$$

When the waveforms of the gravitational waves are developed in terms of $\frac{v}{c}$ for the post-Newtonian approximation, the chirp mass is the leading term for the zeroth order. As a consequence, it is the parameter that is the best determined when the gravitational wave is observed [37].

Parameter	Value	Reference
Effective inspiral spin	$0.07^{+0.12}_{-0.11}$	[23]
Luminosity distance	$580^{+160}_{-210} M_\odot$	[23]
Final spin	$0.72^{+0.07}_{-0.05}$	[23]
Primary mass	$30.7^{+5.7}_{-3.0} M_\odot$	[23]
Secondary mass	$25.3^{+1.4}_{-4.1} M_\odot$	[23]
Chirp mass	$24.2^{+1.4}_{-1.1}$	[23]
Radiated energy	$2.7^{+0.4}_{-0.3} M_\odot c^2$	[23]
Source redshift	$0.12^{+0.03}_{-0.04}$	[23]
Peak luminosity	$3.7^{+0.4}_{-0.5} \times 10^{56} \frac{erg}{s}$	[23]
Sky localization	$87 deg^2$	[7]
GPS time	$1186741861.5s$	[7]
Right ascension	$03h11min$	[7]
Declination	$-44°57min$	[7]
L1 SNR	13.7	[23]
H1 SNR	7.3	[23]
V1 SNR	4.4	[23]

Table 2.1: Summarizing table for the different parameter values of the GW170814 event found throughout the literature.

2.2 Raw strain

2.2.1 Acquiring the data

In PyCBC, there exists a library, called *Merger*, which enables one to have direct access to the strain time series for the detected events of the O1 and O2 runs. Without any supplementary
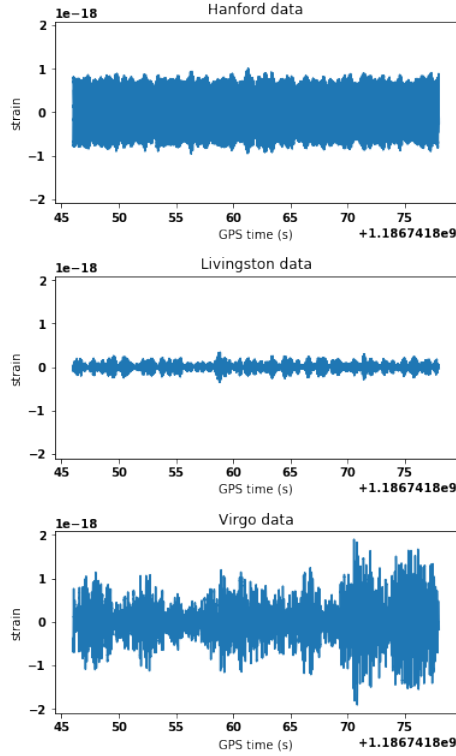
Figure 2.1: Raw strain in the 3 detectors. The y-axis is the same for the three detectors in order to enable the comparison of the variability of noise in the different detectors at the time of the event. The gravitational wave event cannot be detected in the signal without further treatment.

treatment, we get the strain in the detector for a 32s time interval centred on the time of the event. This strain has already been treated in order to take into account the characteristics of the detectors at the time of the detection. The obtained strains can be seen in Fig.2.1. It can be seen that the Virgo detector was more noisy during the O2 run. Indeed, one directly sees that the strain in this detector extends over a wider frequency-range than those of the two LIGO detectors and undergoes more variations. In addition, the LIGO-Livingston detector is also the one with the least noise.

These first manipulations of the data are done with the functions present in the *pycbc.merger* library. The event is downloaded using the command *Merger("GW170814")*. The strain is then directly found in each detector using the command *Merger.strain('Detector')*, where *Detector* takes the values H1, L1 or V1, corresponding to LIGO-Hanford, LIGO-Livingston and Virgo respectively. This returns a PyCBC *TimeSeries* object, which has its dedicated options giving information about the event, such as the duration in time, the start time and the end times, which are found with the commands *timeSeries.duration , timeSeries.start_time, time-Series.end_time*. The plots are made with the *matplotlib.pyplot* library of Python (as it will be the case all throughout this work).

Plots such as Fig.2.1 do not directly show the event signature: it is totally swamped in the noise

of the detectors. Indeed, the strain that comes out is

$$h(t) = \frac{\Delta L_y - \Delta L_x}{L}, \tag{2.3}$$

hence the difference of the lengths of each arm for each detector divided by their length. The raw data include the signal and the noise [38].

2.2.2 Sources of noise

In order to have a good understanding about the raw strain and how the gravitational wave is swamped in the noise, it is useful to have an overview of some of the major sources of noise. They are important to characterize because we want to measure a strain of the order of $h \sim 10^{-21}$ for arms of length 4 km for the two LIGO detectors and 3 km for Virgo. So, due to this high precision, the detectors have a high sensitivity and many small perturbations are detected.

Some common sources of noise are:

- *Shot noise*: for the precision envisaged here, the quantization of light as photons has to be taken into account. This noise is due to the photons arriving irregularly on the photodetector [39].

- *Radiation pressure*: there is an uncertainty on the exact position of the mirror due to the fluctuation of the action of the reflected photons [40].

- *Seismic noise*: it regroups the motion of the ground, which can have several causes, with major influences depending from the frequency range that is considered. From 1 to 10Hz, the noise is mainly due to human activities (such as the traffic), but also wind and rain. There is also a micro-seismic background that comes from the small motions of the tectonic plates. This gives rise to small surface waves that shake the detector and, as a consequence, the mirrors. This noise is diminished by the decoupling of the mirrors from the Earth with pendulum systems or active seismometers. Due to this noise, the low frequency region is inaccessible from Earth, which motivates project such as LISA, a space gravitational wave detector [4, 11].

- *Newtonian noise*: it takes into account the variation of the gravitational force applied on the mirrors. On Earth, the most important contributor to the variation of the gravitational force is the micro-seismic noise. This induces a variation of the mass density in the region under the detectors, leading to a variation of the gravitational potential affecting the test masses. Another source of Newtonian noise is every object with a mass that passes in the vicinity of the mirrors. Indeed, the detectors are so sensitive that the gravitational field of an object passing by leads to a detectable perturbation of the mirrors [41].

- *Thermal noise*: when the temperature is non-zero, the molecules of the mirrors, their coatings and the suspensions are not at rest. These different parts are thus vibrating. For the suspensions, the thermal motion leads to a swinging motion of the suspensions and a horizontal motion of the mirrors. Another noise that is present for the suspensions, called

the *violin modes*, corresponds to the excitation of the normal rotational modes of the suspension wires. That leads to peaks in the power spectral density. They are constituted by the fundamental mode of vibration, as well as its harmonics. For the mirror itself, the non-zero temperature leads to a Brownian motion of the atoms of the surface, leading to noise. Furthermore, in the volume of the mirror, the temperature fluctuations are not uniform. Therefore, there is a displacement noise that is due to the differential expansion from one place to the other. A last noise source for the mirrors is the fluctuation of the refraction index of its coating, which is a function of the temperature. So, if it is not uniform on the surface of the mirror, the index is neither [4].

- *Interaction with air molecules*: if the lase beam interacts with air molecules, it can be deflected from its path, leading to noise. This is avoided in the detectors by having an ultra-high vacuum in the pipes where the laser travels [4].

- *Diffusion and stray light*: the mirrors can diffuse a part of the light when it is reflected, hence producing background photons [4].

- *Power fluctuation of the laser*: even if the lasers are stabilized as much as possible, a faint variation in their power can and is detected, leading to spurious variations [4].

The two first sources of noise that have been described above are quantum noises, due to the quantum behaviour of the light. The other noises are less intrinsic in the sense that they come from external causes and could, in theory, be avoided.

All these noises are able to mask the signal. Therefore, the signal has to be cleaned in order to keep only parts where the signal of the gravitational wave is present. Moreover, the change must be such that the useful signal is not (even partly) taken out. The subtraction of the noise out of the data will be explained in the coming parts of this work.

2.3   First manipulation of the data

A first manipulation that can be made in order to have another view of the data is to zoom in on the event. This can be done in PyCBC by the use of *time_slice(start_time, end_time)*. It allows to focus on the part of the signal going from the *start_time* to the *end_time*, giving a close view depending on the selected time interval. This leads to the graphs presented in Fig.2.2.

This zoom enables us to see that the low-frequency part of the signal is dominated by the noise. In addition, the signal is not the same for all the detectors. This comes from the dependence of most noises on the specific detector [42].

When the analysis is done, we know that the smaller frequencies, below 15Hz, are dominated by noise. So, by cutting off the frequencies under this value, we get rid of some noises, without loosing the gravitational wave signal. In PyCBC, there exists the build-in function *data.highpass_fir(lowest_frequency, order)*, which enables to do a high-pass filter. The order of
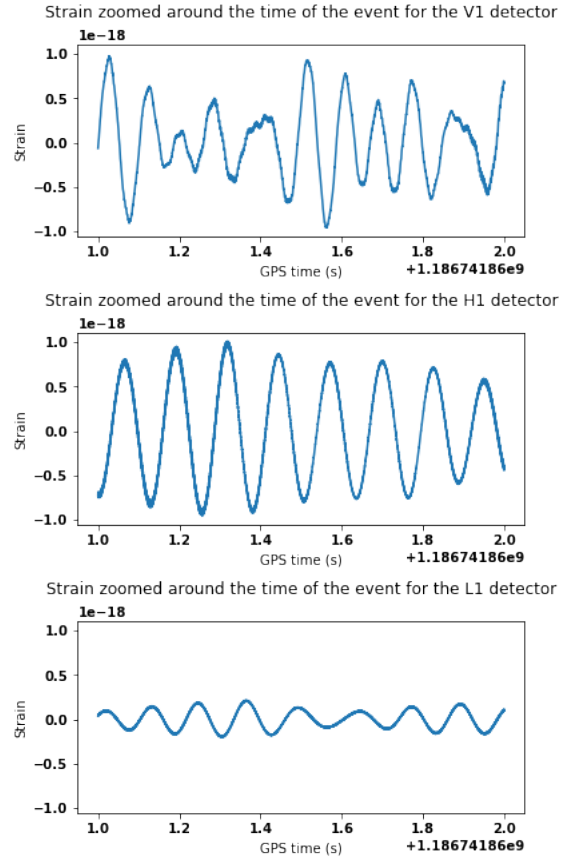
Figure 2.2: Zoom on the raw data around the event within an interval of 1 second centred on the time of the event.

the FIR high-pass filter is fixed at 512 in the analysis done here. Thus value is chosen because it is the one used in the PyCBC tutorials. If its value is increased, there will be fewer ripples in the band-passed data. Once high-passed, the time series obtained for the data do not yet present a clear signature of a gravitational wave event. Nevertheless, the amplitude of the signal is decreased and presents fewer long-period variations. The absence of a clear signature comes from the noise at higher frequency, which is still important enough to swamp the signal. The frequency cuts ore done in the frequency domain, which is obtained thanks to a Fourier analysis of the data. However, it is implicit, as the PyCBC command directly applies on the time series data. More manipulations of the data are thus needed in order to see the gravitational wave event appear clearly.

2.4   Power spectral density

The power spectral density (PSD) is used in order to model the noise that is present in the detectors at the time of the detection. In practice, we compute an estimate of it. This is done by the use of Welch's method, which is based on the Fourier analysis of the data.

2.4.1   Mathematical tools for the computation of the PSD: FFT, window functions and Welch's method

Welch's method is an application of the fast Fourier transform (FFT) algorithm in order to find an estimate for the power spectrum. So, before describing Welch's method, it is important to have a reminder about the FFT.

The FFT algorithm is an efficient way to compute the discrete Fourier transform (DFT) in the case of a finite and arbitrary number of evenly spaced sample points.

We suppose the data to be made of a real sequence of points x_n, which corresponds to values of x measured at times $t_n = t_0 + nT$, where t_0 is the starting time of the measurements and T is the time interval between two consecutive sample points. The sequence is assumed to contain N points. The discrete Fourier transform of this set is then a sequence $\mathscr{X}_k$ of complex numbers, called *Fourier amplitudes*, which is given by the formula:

$$\mathscr{X}_k = \sum_{n=0}^{N-1} x_n e^{-2\pi i \frac{nk}{N}}, \tag{2.4}$$

where $k = 1, 2, \ldots, N-1$.

The DFT of the signal represents the amplitude and phase of the sinusoidal components that reproduce the input signal.

As was the case for the continuous Fourier transform, it is also possible for the discrete case to

be inverted. Its inverse is given by the expression

$$x_n = \frac{1}{N} \sum_{k=0}^{N-1} \mathscr{X}_k e^{2\pi i \frac{nk}{N}}. \tag{2.5}$$

A useful property of the DFT is that it enables one to transform operations done on the functions in the time domain into equivalent and easier operations done on the functions in the frequency domain. For example, the differential operators that act on x become multiplicative ones in the frequency domain.

Based on the definition (2.4), one can write the relations for each $\mathscr{X}_k, k \in [0, \ldots, N-1]$ explicitly. This provides the relations:

$$
\begin{aligned}
\mathscr{X}_0 &= x_0 + x_1 + \ldots + x_{N-1} \\
\mathscr{X}_1 &= x_0 + x_1 e^{\frac{-i2\pi}{N}} + x_2 e^{\frac{-i4\pi}{N}} + \ldots + x_{N-1} e^{\frac{-i2\pi(N-1)}{N}} \\
&\vdots \\
\mathscr{X}_{N-1} &= x_0 + x_1 e^{\frac{-i2\pi(N-1)}{N}} + x_2 e^{\frac{-i4\pi(N-1)}{N}} + \ldots + x_{N-1} e^{\frac{-i2\pi(N-1)^2}{N}},
\end{aligned}
\tag{2.6}
$$

which can be written under the matrix form

$$
\begin{pmatrix} \mathscr{X}_0 \\ \mathscr{X}_1 \\ \vdots \\ \mathscr{X}_{N-1} \end{pmatrix} = \begin{pmatrix} 1 & 1 & \cdots & 1 \\ 1 & e^{\frac{-i2\pi}{N}} & \cdots & e^{\frac{-i2\pi(N-1)}{N}} \\ \vdots & \vdots & \ddots & \vdots \\ 1 & e^{\frac{-i2\pi(N-1)}{N}} & \cdots & e^{\frac{-i2\pi(N-1)^2}{N}} \end{pmatrix} \begin{pmatrix} x_0 \\ x_1 \\ \vdots \\ x_{N-1} \end{pmatrix}. \tag{2.7}
$$

Taking into account that the matrix elements are N^2 complex numbers, one sees that there are N^2 complex multiplications to perform as well as $N(N-1)$ complex additions [43]. This clearly shows that the number of operations to perform grows rapidly with the size of the sample. Therefore, the FFT transform algorithms have been introduced in order to perform the computation more rapidly and with fewer operations. The most common one is the *Cooley-Tukey* algorithm, which was implemented for high speed computers in 1965 and described in [44].

The method developed in this algorithm enables one to find the result of a DFT in less than $2N \log_2(N)$ operations by iterating over the array of the Fourier amplitudes. In order to find the algorithm, the total number of samples is assumed to be composite, hence

$$N = r_1 r_2. \tag{2.8}$$

In this case, the k and n indices used in Eq.(2.4) obey the rules:

$$k = k_1 r_1 + k_0, \quad k_0 = 0, 1, \ldots, r_1 - 1, \quad k_1 = 0, 1, \ldots, r_2 - 1 \tag{2.9}$$
$$n = n_1 r_2 + n_0, \quad n_0 = 0, 1, \ldots, r_2 - 1, \quad n_1 = 0, 1, \ldots, r_1 - 1. \tag{2.10}$$

Introducing these relations in the definition (2.4) of the DFT, it can be rewritten as

$$\mathscr{X}(k_1, k_0) = \sum_{n_0} \sum_{n_1} x(n_0, n_1) e^{-\frac{2\pi i k}{N} n_1 r_2} e^{-\frac{2\pi i k}{N} n_0}. \tag{2.11}$$

28

However, one also has:

$$e^{-\frac{2\pi i k}{N} n_1 r_2} = e^{-\frac{2\pi i}{N}(k_1 r_1 + k_0) n_1 r_2}$$

$$= e^{-\frac{2\pi i}{N} k_1 r_1 n_1 r_2} e^{-\frac{2\pi i}{N} k_0 n_1 r_2}$$

$$= e^{-2\pi i k_1 n_1} e^{-\frac{2\pi i}{N} k_0 n_1 r_2} \tag{2.12}$$

$$= e^{-\frac{2\pi i}{N} k_0 n_1 r_2}.$$

As a consequence, the sum over n_1 in (2.11) depends only on k_0 and n_0. It can be expressed as

$$x_1(k_0, n_0) = \sum_{n_1} x(n_1, n_0) e^{-\frac{2\pi i}{N} k_0 n_1 r_2}, \tag{2.13}$$

leading to the expression of the Fourier series under the form:

$$\mathscr{X}(k_1, k_0) = \sum_{n_0} x_1(k_0, n_0) e^{-\frac{2\pi i}{N}(k_1 r_1 + k_0) n_0} \tag{2.14}$$

In this expression, the $x_1(k_0, n_0)$ array contains N elements and the computation of each of them needs r_1 operations. So, the total number of expressions needed to find the array is Nr_1. Furthermore, once this array is obtained, Nr_2 extra operations are needed in order to find $\mathscr{X}$. So, this two-step algorithm requires a total of $N(r_1 + r_2)$ operations.

In practice, the algorithm is applied in m steps instead of two and the total number of operations is $N(r_1 + r_2 + \cdots + r_m)$ when $N = r_1 r_2 \ldots r_m$. Generally, the use of more factors leads to a minimization of the operations, as the values of the r_j factors in the sum become smaller. In addition, if all these factors are equal ($r_j = r \quad \forall j$), then $m = \log_r N$ and the total number of operations is given by $rN \log_r N$

If $N = r^m$ and T is the total number of operations, then

$$\frac{T}{N} = m.r \tag{2.15}$$

and

$$\log_2 N = m \log_2 r. \tag{2.16}$$

At the end, we have

$$\frac{T}{N \log_2 N} = \frac{r}{\log_2 r}. \tag{2.17}$$

This relation gives an estimate of the number of operations needed, depending on the value of r and the number of sample points that are taken into account. When plugging-in numbers in the relation, one finds that the most efficient value is $r = 3$. However, the gain is only of 6% with respect to $r = 2$ or $r = 4$, which have other advantages in terms of addressing and multiplication economy when working with a binary-based computer. Moreover, the ratio has a value 50% higher when $r = 10$, which translates to an equal increase of the number of computations. At the end, a composite value of N with a lot of small factors can be found, which can decrease quite substantially the number of computations done [44].

When Welch's method is applied to the gravitational waves, at some point, a DFT has to be computed. The use of the FFT algorithm described above helps to make the computation process of the PSD more efficient.

An additional tool that is needed in order to have a good understanding of Welch's method is the *periodogram*. It is defined as the squared-magnitude of the DFT of the x_n data points, divided by the number of points:

$$P(k) = \frac{1}{N} \left| \sum_{n=0}^{N-1} x_n e^{-\frac{2\pi i}{N} nk} \right|^2. \tag{2.18}$$

When we take the limit $N \to +\infty$, the expected value of the periodogram is the power spectral density of the process described by the data points [45]. So, the periodogram already is an estimate of the PSD. However, Welch's method does not use simple periodograms, which is motivated by a better statistical behaviour for the estimate.

A last concept that has to be introduced is the concept of *windows*. Indeed, the DFT's computed during the application of Welch's method are on windowed data, which means the data sequence multiplied by a window function. The principal reason is to avoid *power leakage*. The latter is intrinsic to the use of a Fourier analysis. Indeed, when a FFT or a DFT of a time series are computed, it corresponds to a decomposition of the signal onto an orthogonal basis, made of the vectors

$$\cos(\frac{2\pi}{N} nk) \text{ and } \sin(\frac{2\pi}{N} nk), \tag{2.19}$$

with $n = 0, \ldots, N - 1$

However, only the frequencies that correspond to those of the basis are projected on a single vector. All the others will have a non-zero projection on all the vectors that constitute the basis. This effect is due to the finiteness of the signal. This can be understood as a discontinuity at the boarder of the signal, where it is refolded by the projection onto the basis, leading to an additional contribution to the power spectrum.

Windows are functions decreasing the effect of this leakage. Windowing is done by reducing the order of the discontinuities that are present at the frontiers of the observed data, which are due to the refolding when the projection is done. Most of the time, it is done by using a function which multiplies the data (in the frequency domain) and sets as many orders of derivations as possible at zero at the borders, where the matching is done [46].

There exist several types of windows (such as Hann, Bartlett, Rectangular, ...). Several of them are detailed in Section 5.2 dedicated to the study of the influence of the window. The one used by default in the analysis of the gravitational waves is the *Hann* window, which can be seen in Fig.2.3 and which is defined as [47]

$$W(n) = 0.5 - 0.5 \cos\left(\frac{2\pi n}{N-1}\right) \quad \text{where } 0 \leq n \leq N - 1 \tag{2.20}$$

In section 5.2, where different windows are tested, it will be shown that it is the window that enables to find the highest signal-to-noise ratio when the matched filtering process is applied.

Now that all the necessary tools have been defined, we can turn to Welch's method itself [48]. Its aim is to estimate the power spectral density of the data. It uses slices of data which may overlap. First, the use of blocks of data instead of the full set allows to decrease the variance of
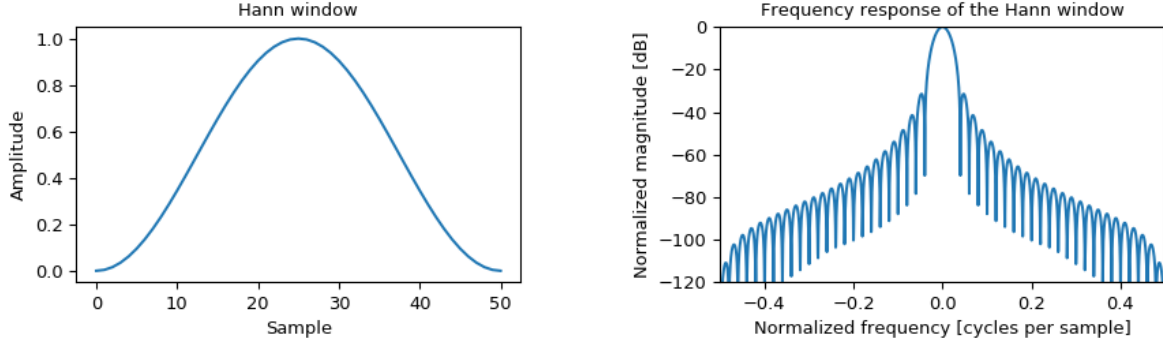
Figure 2.3: Left, the Hann window in the time domain, showing a smooth decrease to zero, which reduces the spectral power leakage. Right, its Fourier transform, showing its response in the frequency domain. Taken from [47].

the estimate. Therefore, it gives a result with a better statistical behaviour than using directly the periodogram of the full data set, as defined in Eq.(2.18) [49].

In Welch's method, the widths of the data segments are arbitrary. However, the computation of several shorter instances is often faster than the computation of the full sequence. The overlap of the data sequences have been shown by Welch to reduce the variance of the final estimator obtained with respect to a case where the data is decomposed in non-overlapping continuous sequences. This happens because the overlap enables to retrieve a part of the correlation that could exist between two successive points which would otherwise be in two different sub-samples. Moreover, it compensates somewhat the narrowing of the bands used, as data that are down-weighted in one block can give a more important weight in another [49].

The computation of the PSD is done as follows [48]: we start with our data sample x_j. Here, it corresponds to a sample of noise with the same characteristics as in Chapter 1. The spectral density of this sample is assumed to be $P(\omega)$.

The data sample is then divided in K sub-samples all having a length L and having their starting point shifted by D. These segments cover the entire time domain covered by x_j. We have the sub-samples:

$$
\begin{aligned}
x_{1,j} &= x_j \quad j = 0, ..., L-1 \\
x_{2,j} &= x_{j+D} \quad j = 0, ..., L-1 \\
&\vdots \\
x_{K,j} &= x_{j+(K-1)D} \quad j = 0, ..., L-1
\end{aligned}
\tag{2.21}
$$

where the notation x_{j+D} stands for $x(t_j + D)$.

Since there is the full coverage of the x_j space, there is also the relation $(K-1)D + L = N$.

Once these sequences are obtained, a data window W_j is applied. So, each of the data bins evaluated at time t_j are multiplied by the window function evaluated at the same time. The W

function can be chosen by the user in order to have the best response possible for the particular data looked at (the Hann window in the case of gravitational waves). This function is not specified here and can be chosen depending on the data that is analysed. Some windows have been proposed by Welch in [48]. This gives the series

$$x_{1,j}W_j, ..., x_{k,j}W_j. \tag{2.22}$$

The DFT of each sequence is then computed, leading to

$$\mathscr{A}_{k,n} = \frac{1}{L}\sum_{j=0}^{L-1} x_{k,j}W_j e^{\frac{-2i\pi kjn}{L}} \tag{2.23}$$

where $k = 1, ..., K$.

In practice, when this step is computed, it is done using a FFT algorithm, such as the Cooley algorithm explained above. This allows to make the process computationally fast and efficient.

The modified periodogram for each sequence is then given by

$$\mathscr{I}_{k,n} = \frac{L}{U}|\mathscr{A}_{k,n}|^2 \tag{2.24}$$

with

$$U = \frac{1}{L}\sum_{j=0}^{L-1} W_j^2$$

.

Eq.(2.24) corresponds to the power of the kth sub-sample, weighted by the square of the window for the time domain covered by the sub-sequence. It is a *modified* periodogram in the sense that it corresponds to the classical periodogram of the sub-sample (given by $L|A_{k,n}|^2$) divided by a weighting factor linked to the window used.

Finally, the estimation of the power spectral density is obtained by taking the average of all these modified periodograms:

$$\hat{P}_n = \frac{1}{K}\sum_{k=1}^{K} \mathscr{I}_{k,n} \tag{2.25}$$

Two interesting behaviours of this method, motivating its use for gravitational waves data analysis is that it can be computed efficiently via FFT algorithms and that it is able to handle long time series in a lighter and more stable way [49].

2.4.2   Practical computation of the PSD

The power spectral density can be built for each detector based on the data sample. It is a way to represent the sensitivity of the detector as it gives the square of the strain that the noise produces for each frequency.

Fig.2.4 also shows the frequency range in which the detectors are the most effective, i.e. the plateau in the PSD. In addition, it contains peaks which can be due to noise. Some peaks
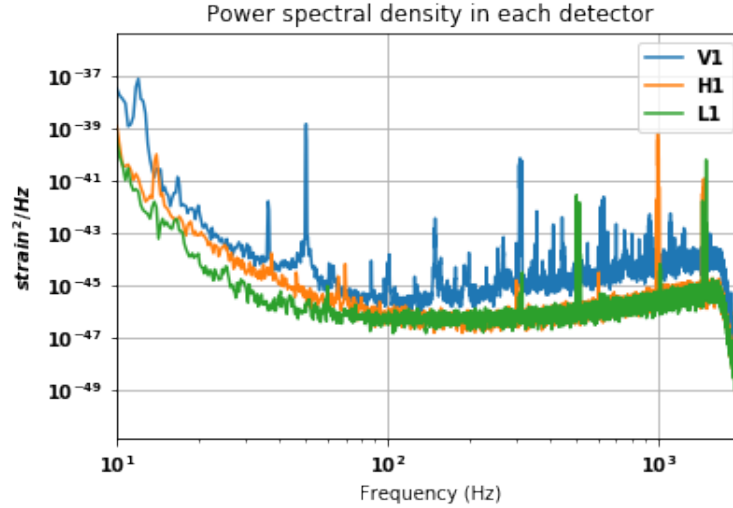
Figure 2.4: Power spectral density for the 3 detectors, represented in the range 10 Hz to 2048 Hz. and build for the 32 s of data centred on the GW170814 event.

are identified as the resonances of the suspensions. Other identified lines are used in order to calibrate the detector in frequency, as they are very precise. It is the case of the lines found at 60 Hz for the LIGO detectors and 50 Hz for the Virgo detector, for example. They correspond to the frequency of the alternating current distributed in each country. The harmonics of the different lines are present as well [50].

Fig.2.4 was calculated with the *.psd(time_interval)* command included in PyCBC [51]. This calculates the PSD of the detector by using Welch's method, taking segments of data that have a length of *time_interval*, taken as 4 seconds for Fig.2.4. The overlap is taken as 50% by default, and the window is the Hann window.

In Fig.2.4, we also see that the curve for the Virgo detector is higher than those for the two LIGO detectors, which are more or less at the same level. This shows that the European detector is less sensitive than the two American ones. In addition, the V1 curve seems to be more noisy than the others. Most of these smaller peaks are the violin modes of the suspensions, mentioned in Section 2.2.2. Those were more important in Virgo at the time of the GW170814 event observation due to the suspensions of the mirrors which, at the time, were made of steel cables holding the mirrors, which lead to a consequent thermal noise. This has been improved for the O3 run (going from April 1, 2019 to March 27, 2020[3]) by using silicate wires that are directly extracted from the mirrors [53]. Note that the PSD is computed while the gravitational wave signal is present in the data, but its impact should be minimal, as the event is short and spread over several frequencies.

---

[3]It should have gone until April 30 but was stopped due to the COVID-19 pandemia [52].

2.5 Whitening the data

The PSD can be used to clean the data. The operation of noise removal is called *whitening* the data. Its goal is to have a normalization of the power for all the frequencies with respect to the noise that is present. It takes the time series and tries to make the power spectral density flat. So, we would see the deviation from the mean of the strain more easily and all the frequencies contribute equally [21].

Mathematically, the computation is done as follows: we take the Fourier transform of the data. This is then divided by the square-root of the PSD computed as explained in the previous section before taking the inverse Fourier transform of the result [22].

For the code, we use the command *data.whiten(arg1, arg2)*, where data is supposed to be a time series. The whitening of the data also uses FFT's and a PSD computation done with Welch's method. Therefore, *arg1* represents the duration of the time interval over which the FFT is done whereas *arg2* is the duration of the time domain filter that is applied. In the code, both intervals have a value of 4 seconds. After this manipulation, the event is still swamped by the noise, even if there seems to be a peak around the event [21].

In order to see the event in the signal, the data is also band-passed. Indeed, one knows the frequency range in which a binary coalescence can be found. One can then to get rid of the large fluctuations that can mask the signal. After this, we have a time series where the frequency range is focused on a smaller range that includes the event.

The bandpass filter applied keeps the frequencies between 30Hz and 250Hz. This is done by the combination of a highpass filter and a lowpass filter respectively with the commands *highpass_fir(30,512)* and *lowpass_fir(250,512)*. These are included in the *pycbc.filter* library. The first argument is the cutoff frequency for the filter and the second is the order of the filter applied, which corresponds to the number of frequency samples that are present left and right from the central point of the time series (corresponding to the time of the event in our case) [21, 45].

After the whitening and the bandpassing have been done, it is possible to distinguish the gravitational wave signal in the data. The event peaks above the noise, as can be seen in Fig.2.5. Nevertheless, the exact form of the signal is not easy to see. We can have a better view by zooming on a smaller time slice around the event, as in Fig.2.6. The identification of the event is easier in the LIGO detectors, which shows once more that those were more sensitive at that time. The identification of the event in the Virgo data, with the naked eye is more difficult due to the lower sensitivity. In fact, the event in Virgo cannot be interpreted confidently as a gravitational wave without the two other detectors, as we will see throughout this work.

As can be seen in Fig.2.6, the event is not detected at the same time in all the detectors. This is due to the finite speed at which the gravitational wave propagates, i.e. the speed light. The GW170418 event was first detected in the LIGO-Livingston detector at 10:30:43 UTC and in the LIGO-Hanford and Virgo detectors with delays of, respectively, $\sim 8ms$ and $\sim 14ms$ [7]. One has to be careful that the event in the Virgo detector does not correspond to the biggest peak,
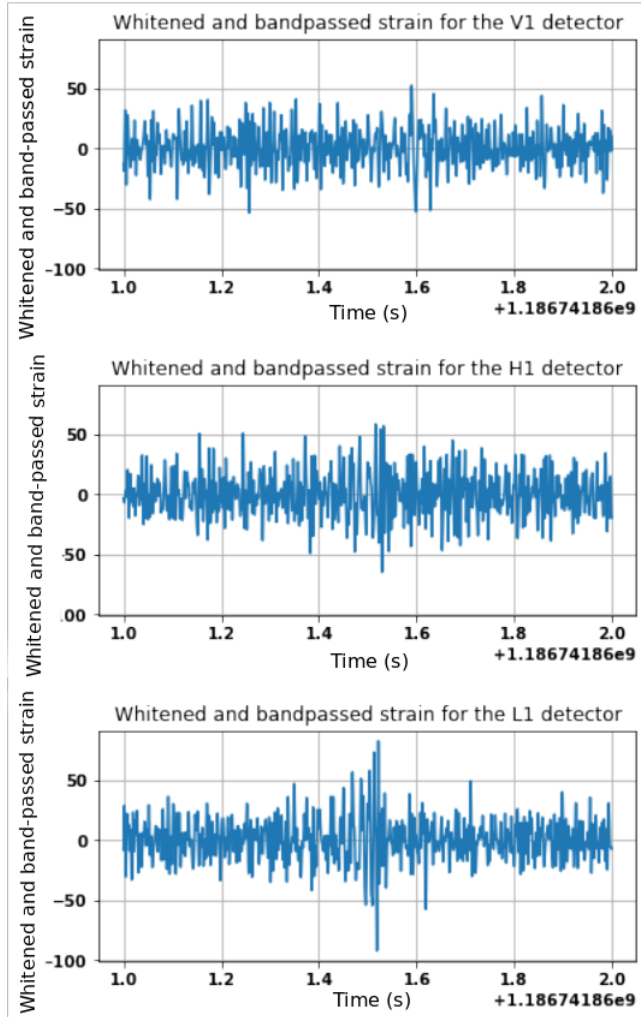
Figure 2.5: Whitened and bandpassed data for the three detectors, centred on the time of the merger. We see a higher variation at the time of the merger, with a progressive increase as the inspiral goes on.
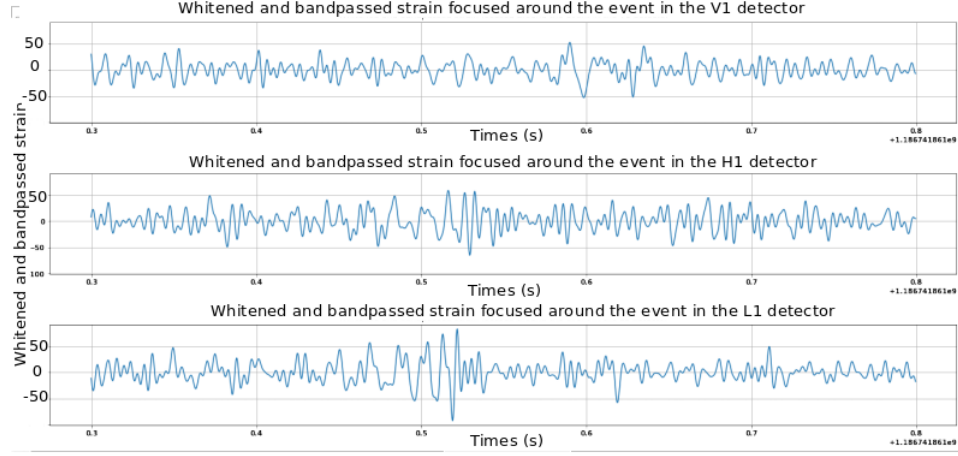
Figure 2.6: Whitened and band-passed strain, zoomed in around the time of the event. We can see a region where the oscillations get closer to each other with an increase in amplitude for the H1 and L1 detectors. On the other, such a patter cannot be distinguished in the V1 detector, showing its lack of sensitivity at the time of the event.

which is too far from the rest. With the knowledge of these times, it is possible to represent, on the same plot, the signal for each detector, with the correct time shift applied in order to superpose the signature of the event. By doing so, one can observe the similarities of the signals. This can be done via of the *roll(shift)* command. The *shift* argument corresponds to a shift applied to each point of the data. The command shifts the complete time series with this time delay. Fig.2.7 shows the superposition of the two LIGO detectors. Because Virgo has a different amplitude, a lot of noise and because the event is not well identified, its addition to the figure it is not very illuminating.
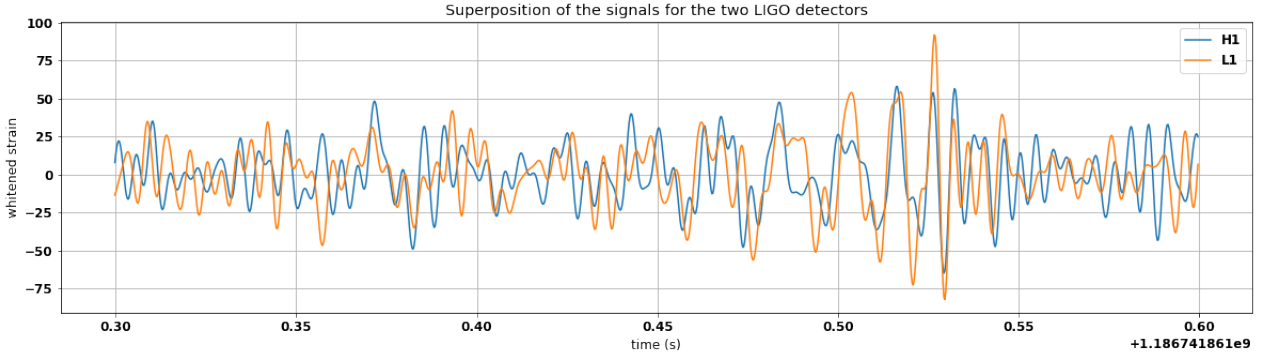
Figure 2.7: Superposition of the signals of the two LIGO detectors. Even if there is slightly more noise in the Hanford detector, the same type of global evolution can be see in both detectors, which is a reassuring observation in order to confirm the presence of a gravitational wave signal.

2.6   The Q-transform

The Q-transform in another way to represent and visualize the data. It is similar to a Fourier transform (it transforms a time series into the frequency domain) but, instead of considering equally spaced centres of intervals, one uses a geometric spacing, hence the points are separated equally on a logarithmic scale. This transformation gives a higher time resolution when looking at higher frequencies, where the frequency bins are wider [54]. In this section, we will first give the mathematical details behind the transformation before looking at its practical computation.

2.6.1   Mathematical details of the Q-transform

The Q transform was originally defined by JC Brown in 1991 to analyse musical samples in a way that fits better the human auditive system [54]. This method can be generalized and particularized to other cases where a geometric distribution of the bins can be useful.

When computing the DFT, the frequency bands have the same width. On the other hand, in some cases, it is interesting to have different separation for different values of the frequencies in order to have a mapping that fits better the explored frequency domain. The Q-transform provides such a possibility. Basically, it is done in the same way as the DFT but with a constant ratio between the centre of the frequency bins.

Before turning to the mathematical definition of the Q transform let us introduce, the *Gabor-Heisenberg theorem* [55]:

$$\Delta\omega\Delta t \geq \pi \tag{2.26}$$

Basically, this expresses that a broader time support of a function gives a narrower its frequency-support and vice-versa. The spectral width $\Delta\omega$ is proportional to the frequency itself. Therefore, the ratio $\frac{\omega}{\Delta\omega}$ is the same for all the angular frequencies [56].

The Q transform can then be defined starting from the *short time Fourier transform (STFT)* [57]:

$$\mathscr{X}^w(\omega, t) = \int_{-\infty}^{+\infty} x(\tau)w(t-\tau)e^{-i\omega\tau}, \tag{2.27}$$

where $w(t)$ is a window function as has been defined in Section 2.4, when we looked at the PSD. The STFT corresponds to the projection of $x(t)$ (the signal) onto a function that has an envelope which is a time shifted version of $w(t)$.

Based on Eq.(2.27), we define a window with a width inversely proportional to the frequency, hence

$$\Delta t_w = \frac{C}{\omega}, \tag{2.28}$$

where C is a constant.

Using the Gabor-Heisenberg theorem, the width in the frequency domain is given by:

$$\Delta\omega_w = \frac{\zeta}{\Delta t_w} = \frac{\omega\zeta}{C}, \tag{2.29}$$

where ζ is another constant.

The quality factor Q is then defined as

$$Q = \frac{\omega}{\Delta\omega_w} = \frac{C}{\zeta} \tag{2.30}$$

Finally the constant Q transform is defined as a STFT which has a window width that depends on the quality factor Q. It is written as:

$$Q_x^w(t,\omega) = \int_{-\infty}^{+\infty} x(\tau)w_Q(t-\tau,\omega)e^{-i\omega\tau}d\tau. \tag{2.31}$$

The window function w_Q used here can be chosen by the user. An example of what happens when the Connes window is used can be found in [58]. This is not the only choice possible. More information about the windows will be given after the definition of the discrete version of the Q transform, as it is the one that is used in the gravitational wave analysis.

The *discrete Q transform* is adapted from the continuous version in the same way the DFT is found based on the continuous Fourier transform. In this case, x is a discrete function of time. Therefore, the integral is replaced by a sum and the Q transform is written as [59]:

$$Q_x(m,k) = \sum_{n=0}^{N-1} x(n)w_Q(n-m,k)e^{\frac{-i2\pi nk}{N}}, \tag{2.32}$$

where N represents the number of samples.

Eq.(2.32) is not an expression that leads to tan efficient computation. The following definition proves to be better:

$$Q_x(m,k) = \sum_{n=0}^{N-1} \mathscr{X}(l+k)\mathscr{W}_Q^*(l,k)e^{i2\pi\frac{ml}{N}}, \tag{2.33}$$

where $\mathscr{X}$ represents the Fourier transform of the data sample and $\mathscr{W}_Q$ is a window function defined in the frequency domain and still dependent on the quality factor.

The advantage of the latter expression for the Q transform is that it can be computed in a simple way: we do the usual DFT of the data shifted in frequency, multiply it by an appropriate window function defined in the frequency domain, and then compute the inverse DFT. In this process, the Fourier transform of the data has to be computed only once. The inverse Fourier transform is then computed only for a specific k,.

Most often, the window chosen is not the Fourier transform of a time-dependent window but rather one that is directly defined in the frequency domain (such as the Hann and Hamming windows for example). The window should have a finite support in the frequency domain.
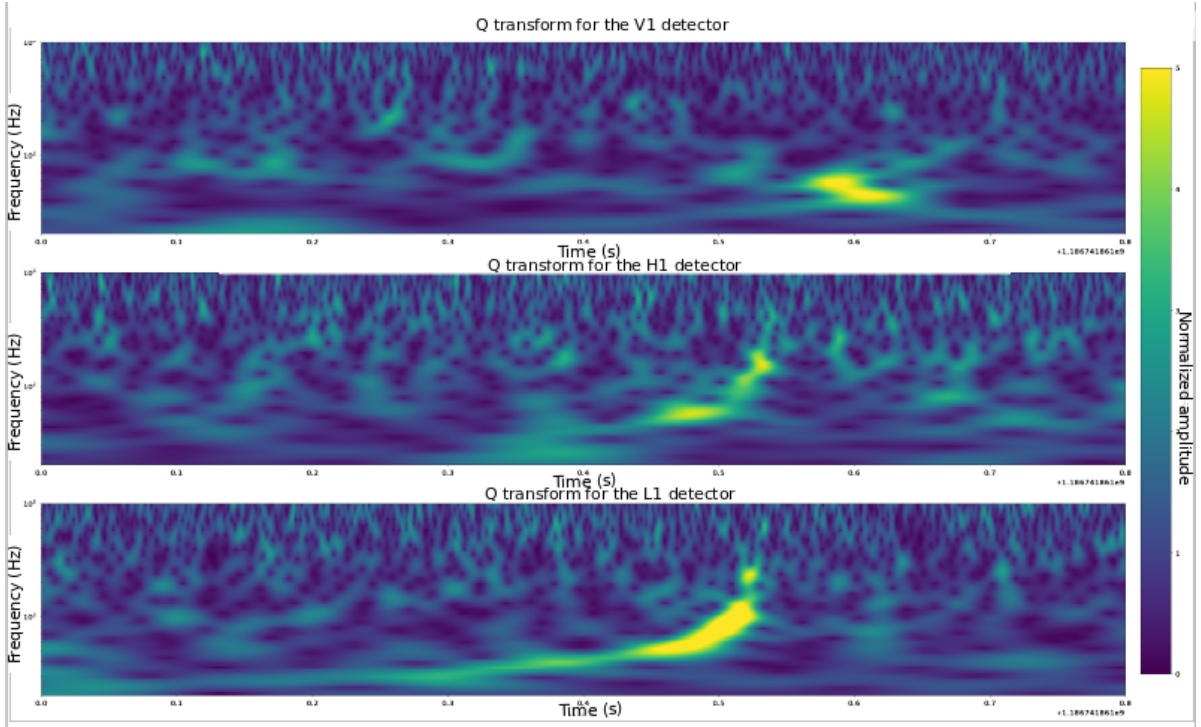
Figure 2.8: Qtransform in each detector of the whitened data for the GW170814 event. We see that the two LIGO detectors show a clear signature of the event whereas the Virgo detector does not display a clear typical banana-like shaped signature.

However, due to the Gabor-Heisenberg theorem, this means that the time resolution is higher when the frequency resolution is smaller. Therefore, the window should be a trade-off between frequency support and time localization. At the end, the window that is used is a classical window function with an argument depending on the frequency and on the Q factor, in order to choose the logarithmic frequency separation [58].

2.6.2   Practical computation

Fig.2.8 shows the Q transform of the whitened data for the GW170814 event. It represents the frequency density as a function of time and frequency. So, we see the evolution of the frequency content in the signal over time. The yellow parts correspond to a frequency that is more densely present, and that has a bigger contribution to the observed signal.

The Q transform helps to see the signature of the event (especially in the L1 detector). In the Virgo detector, it takes form of a patch rather than the clear evolution of the frequency seen in the LIGO detectors. The patch does not correspond to the bright yellow part, which is not the signature of the event. In fact, the trace of the event is the patch on the left of the sharp over-density. The latter is more than 100 ms after the signal in the LIGO-Livingston detector whereas the patch has a delay of 14 ms. This fainter signature casts a slight doubt about the triple detection, as we cannot say that the Virgo detector really detected the event. There is

rather an over-density falling in the correct spot to be seen as a signal (but it does not help for the parametrization of the event for example).

The evolution of the frequency, which is best seen in the LIGO detectors, can be understood by focusing on the different phases of the merger. The first one is the inspiral, when the two objects (black holes and/or neutron stars) rotate around each other, emitting gravitational waves. As they come closer, by conservation of angular momentum, their orbital velocity increases, leading to an increase of the frequency of the emitted wave. This can be seen by the increase of the lower tail of the banana shape as it goes on. The duration of this phase depends mostly on the chirp mass of Eq.(2.2) [60]. Then, the two objects merge, which happens just after the peak in frequency. The next step is the ring-down where residual emission occurs at lower frequencies. This last phase cannot be seen in the Q transform. Thus, what is observed is the increase of the frequency as the black holes come closer to each other before they merge. The computation of the different parts of this phenomenon and the details will be described further in the section on template generation.

The plots shown in Fig.2.8 are obtained directly with the command *qtransform(spacing, bins, q_range, freq_range)*, where *spacing* is the time spacing needed for the output image, *bins* represents the number of frequency bins for the output knowing that these are logarithmically spaced, *q_range* is the the range of the Q transform which we want to maximize (higher values are better for longer durations) and *freq_range* is the frequency range of the output. This command calls a build-in function that calculates the Q transform in an efficient way.

Note that, if the signal is quieter (for sources with lower masses or further away for example), the signature also appears less clearly. So, the Q transform can be a good diagnostic tool for the presence of a merger but it is not enough. Therefore, the search for a signal is not only made via the Q transform but also through *matched filtering*. Although it has been shown that a merger is not always clearly identified in the Q transform, in some cases, the waveform is not well enough known to be found through matched filtering and the presence of an event can be better detected by over-densities in the frequencies. Therefore, the LIGO-Virgo collaboration uses several pipelines for the data analysis and one of them is based on the Q transform, which can find events which are not yet modelled, such as pulsars, gamma ray bursts, etc. [58].

Chapter 3

Significance of the event

In this chapter, the GW170814 event is further analyzed. Now that the data has been whitened and visualized correctly, it is possible to set up a way to find the *significance* of the event. In order to do so, the data is prepared, which is called *preconditioned*. After that, the matched filtering technique described in the first chapter is used. This requires the construction of a model waveform which is matched filtered. For the different times, the signal-to-noise ratio is computed. Once this is done, a test, called the *chi-square test* is applied. It enables us to discriminate between the high SNR's that are found due to a glitch in the detector and the peaks due to the matching between the filter and the data. This test gets rid of many fictitious peaks. The significance of the peak that is found is also computed.

So, this section explains and illustrates how a signal is found in the time series of the detectors. The procedure is explained globally and we make the first triple detected event as an example. As has been explained in the first chapter, matched filtering is based on the work of Weinstein and Zubakov [27] and enables us to extract a signal swamped in noise, when its characteristics are known. In the case of gravitational waves, we try to see if, in the time series recorded by the detector, we find a signal that is looking like a gravitational wave template. In the example, two models are used for the templates. One, rather simple, where the masses of the two black holes are assumed to be equal, with a value given by the average of the masses encoded in PyCBC. For the other model, the template is made by using the central values presented in Table 2.1. In a real analysis, one does not know the characteristics of the waveform. Therefore, each segment of the data is compared with a bank of templates made of a large variety of waves. Once a signal is detected, one can focus on it and fine-tune the parameters of the event. The process described here is thus done for all the templates that are present in the bank [61]. However, processing numerous templates is CPU-intensive and is consequently not done in this work. The case of two different templates also shows how we can find the one describing best the event, as the SNR should be higher when the template is closer to the parameters of the event leading to the gravitational wave signal.

In this section, the numerical methods are described and the mathematics are explained. The numerical code used is based on the tutorials provided by the *LIGO Open Science Collaboration*

(LOSC)[1].

3.1 Preconditioning the data

Before trying to fit a waveform on the data, one needs to transform it to a form that is suited for matched filtering. Therefore, the data is high-passed in order to get rid of the low frequency noise. This is done with the *highpass_fir()* already described previously. In addition, the data is down-sampled from 4096Hz[2] to 2048Hz in order to have a lighter computational process. This step in not mandatory but reduces the computation time. These modifications of the signal lead to the presence of spikes in the data. Indeed, the data are wrapped in a cyclic way and the resampling leads to a discontinuity at the matching, giving extra power at the scale of the length of the applied filter. The peaks are removed from the data by cutting a part of the signal at the start and the end of the series. Therefore, one can use the *crop(start, end)* command included in PyCBC, where *start* is the number of seconds to take away at the start of the sequence and *end* is the number of seconds to take away at its end.

An extra function that must be computed is the PSD of the three detectors, as one will need them for matched filtering, one will need a model for the noise. In this case, a more precise PSD can be obtained by interpolating its estimate so that it matches the frequency interval of the data. This is done with the function *interpolate(psd, delta_f)* included in the pycbc.psd package, where *psd* is the PSD found similarly to that in Section 2.4 and *delta_f* is the frequency step of the data. The functions found this way enables us to have a PSD where each point corresponds to a frequency point of the data. The PSD is then passed as argument to the *psd.inverse_spectrum_truncation(psd, time_slice × sample_rate, low_frequency_cutoff)* function. It takes as argument the PSD and smoothes it out. *time_slice* is the length of the time windows taken to compute the PSD with Welch's method and *sample_rate* is the rate at which the data has been sampled (2048 Hz here). *low_frequency_cutoff* corresponds to the frequency used to high-pass the data. This operation returns a smoothed version of the PSD that accounts for the frequency cuts done to the data [51].

3.2 Making a template to fit the signal

Throughout this work, we will use two types of templates: *IMRPhenomD* and *SEOBNRv4*. Both are specific to binary black holes [62]. The former builds the template in the frequency domain and the latter in the time domain. The choice of the one over the other will depend on the what is the most useful in the context. We will see the difference that arise when we look at the case of neutron star binary mergers in Chapter 7.

As an example, matched filtering has been performed using two templates, built with dif-

---

[1] which can be found at the address: `https://github.com/gwastro/PyCBC-Tutorials`.

[2] This is the default sampling of the data available in PyCBC, other samplings can be found when the data is accessed differently.
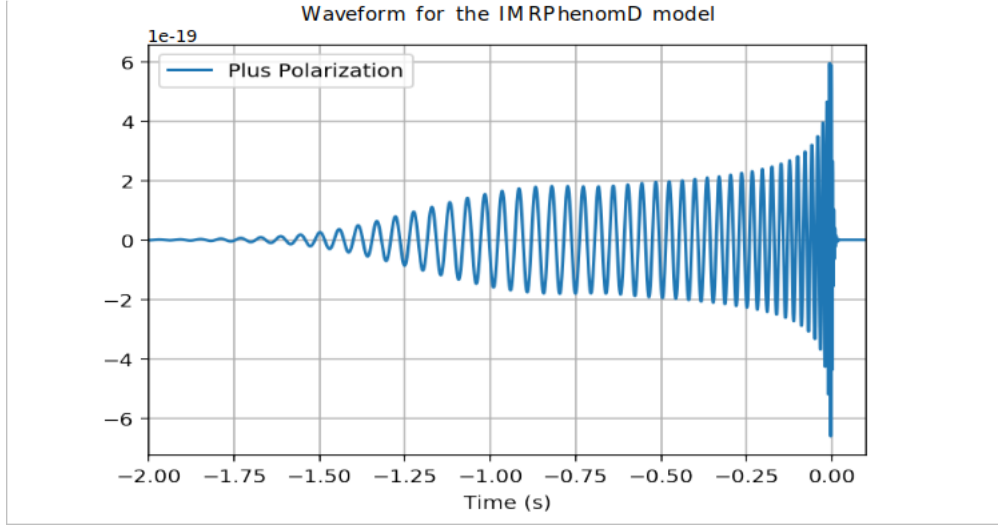
Figure 3.1: Plus polarization for the IMRPhenomD model in the time domain. The signal has been transformed by an inverse Fourier transform. We can see the inspiral where the amplitude and frequency increase slowly, followed by the merger, where the amplitude is maximum and the frequency is so high that we cannot distinguish the oscillations anymore. Finally, we see the ring-down, where we have a fast decrease of the amplitude, before it goes to zero.

ferent parameters and using the IMRPhenomD model. The first case is that of two black holes with the same mass. In the second, the parameters are fixed at the central values given in Table 2.1. In order to make one template with one waveform, it is enough to use the *get_fd_waveform(approximant, parameters, f_lower, delta_f)* function present in the py-cbc.waveform package. This takes as argument the model that one wants to use (noted *approximant*), the parameters of the objects (masses, spins, etc.), the lowest frequency in the range and the spacing in frequency. Some waveform models are not built in the frequency domain but in the time domain. PyCBC enables to make such models with *get_td_waveform(approximant, parameters, f_lower, delta_t)*. It takes the same argument as the frequency domain function, except that we give the time spacing of the points (*delta_t*) instead of the frequency spacing (*delta_f*) and that it returns both polarizations directly in the time domain.

It is possible to go from the time domain to the frequency domain by the application of the Fourier transform, with the *timeseries.to_frequencyseries()* function. It is also possible to go back to a time series by the application of the inverse Fourier transform, with the *frequency-series.to_timeseries()* command. Although the frequency domain often helps for the computations, we have a better view of the evolution of the system in the time domain.

Fig. 3.1 shows the time domain gravitational wave signal for the IMRPhenomD model (obtained after Fourier transform of the waveform).

The IMRPhenomD model is a phenomenological model. It assumes aligned spins and has been tuned to a lot of simulated mergers [31]. So far, it has been said that the gravitational wave van have two polarization. But, only on of them has been focused on. So, it can be interesting to plot both polarizations on the same plot in order to have a view of their difference. This is
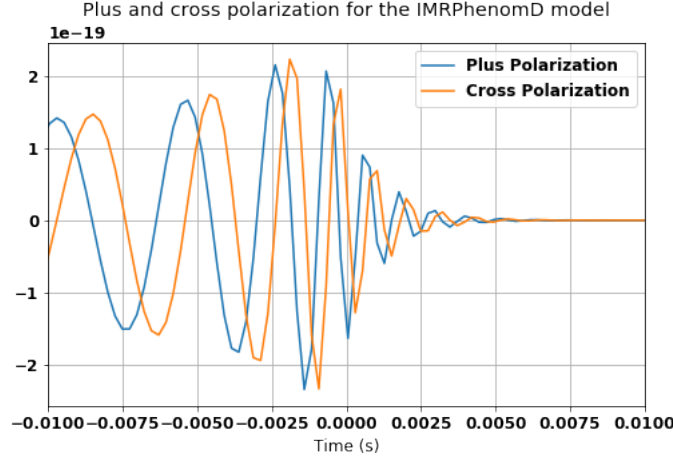
Figure 3.2: Waveform for the IMRPhenomD model showing both polarizations after inverse Fourier transform, zoomed around the time of the merger. We have a better view on the ring-down part, where the amplitude decreases to zero. A shift can be observed between the two polarizations.

done in Fig. 3.2, where it can be seen that the two polarizations have a slight shift between them. Therefore, the use of one or the other can give a slight difference in the time of the event. In addition, when carefully looked at, the figure shows that the amplitude is not totally the same. Indeed, the maximum of the cross polarization is slightly higher than that of the plus polarization. It can also be noted that the cross polarization becomes flat a bit later than the plus polarization in time. So, one sees that both polarizations are important for the analysis as they are not the same. The difference comes from the the phase of the signal. This is true as long as the orbital plane of the binary system is not precessing [4].

The SEOBNRv4 model is based on the effective one-body formalism with aligned spins. The idea behind this formalism is to use the analytical results found in this approximation, and use resummation methods in order to describe the complete waveform, including all the phases, even the non-perturbative ones. The model also relies on non-perturbative information that can be extracted from numerical simulations. The details about the equivalent one-body formalism can be found in [32].

Even if the waveform can easily be obtained, it can be interesting to detail further how such waveforms are actually built. They have to cover the whole cycle of the coalescence, hence the inspiral, the merger and the ring-down. The inpiral part can be computed in terms of the post-Newtonian approximation. This formalism enables us to have an approximate expression for the equations of evolution of the system. This approximation is mostly used when Newtonian gravity is still dominating but the relativistic effects have an influence on the evolution of the system. It describes the lowest order effects of relativity. Its expression takes the form of powers of $\frac{v}{c}$ and $\log\left(\frac{v}{c}\right)$ where v is the orbital velocity of the binary system and c the speed of light. This expansion depends on the energy as well as on the angular momentum of the binary system. In this approximation, at the zeroth order, one recovers the Newtonian expression. The complete analytical derivation of the expansion can be found in [4] and [29] for example. The derivation can also be found numerically. Even if this approximation is not too difficult

to put into practice, it is not valid anymore when the relativistic effects are dominating. That is the case when we are at the merger and the ring-down (it breaks down a bit earlier in fact). In these phases, one needs the full theory of general relativity. However, it is totally non-linear and no analytical solution can be found. Therefore, one needs numerical relativity. Knowing all this, the computation of the waveform is done in several steps. First, the inspiral is computed numerically with one method (Effective one-body, phenomenological or other based on the post-Newtonian approximation), which is not too CPU-expensive. The two other phases are computed separately with numerical relativity. This is often much more CPU-extensive and takes more time. After that, both parts are "glued" together in a process called *hybridization*. The basic idea in order to have the matching is to assume that there is a time region where both models overlap. Then, one proceeds to a minimization of the difference between the numerical model and the post-Newtonian one. At the end, we obtain a single curve, where each part is dominating in its own validity domain and the part where they overlap is a kind of mean of both approaches [30].

The exact waveform depends on different parameters. These are [63]:

- the masses of the two objects;

- the spins of the two objects. These are vectorial quantities and thus contain 6 parameters;

- the localization in the sky, which is expressed in celestial coordinates (right ascension and declination).

- the luminous distance of the source (D_L), given by $D_L = \sqrt{\frac{L}{4\pi S}}$, where L is the bolometric luminosity and S, the bolometric flux;

- the orbital angular momentum which is perpendicular to the orbital plane. It is described with two angles with respect to the line of sight. If the two spins of the two objects are not aligned with the total angular momentum, the orbital plane will precess along the sum of the spins and the angular momentum. This causes a variation over time of the inclination angle;

- the merger time, which is the time at which the amplitude of the signal is maximum;

- the phase at which the objects merge.

The last two points are a matter of convention because, before merging together, the two objects have orbited one around the other for a very long time (millions of years). The merger takes place in a few minutes or even seconds depending on the objects involved, and is taken as the time of the peak of the waveform.

In total, we have 15 parameters that are used to describe the waveform. This is the case in a quasi-circular orbit approximation. When the orbit is more eccentric, even more parameters are needed. Another case that requires extra parameters is the merger of neutron stars which shall be explained in Chapter 7. Indeed, contrarily to a black hole that is rigid, a neutron star can be deformed by the gravitational influence of its companion, and the two stars can be disrupted. These tidal deformations lead to a change in the waveform [63].

3.3 Signal to noise ratio and matched filtering

As described in Chapter 1, the basic idea behind matched filtering is to compare the signal with a template and find a time where both matches. It is the most efficient way to retrieve a signal hidden in white noise when its characteristics are known. If the Fourier transform of the signal is written $\mathscr{I}$ and that of the transfer function of the filter is written $\mathscr{H}$, one maximizes the signal-to-noise ratio

$$z(t_0) = \int_{-\infty}^{+\infty} \frac{\mathscr{I}(\omega)\mathscr{H}^*(\omega)e^{i\omega t_0}}{\mathscr{R}_n(\omega)} d\omega, \tag{3.1}$$

where $\mathscr{R}_n(\omega)$ is the power density of the noise and t_0 is the fiducial time at which the matching between filter and data is made [33]. This ratio is evaluated for all times and we get a graph of the statistic for each time, shown in Fig. 3.3, where we plot the real SNR for each time. This gives the signal-to-noise ratio representation, where the peaks represent times at which the signal and the template are supposed to match best.

Whereas the procedure of matched filtering can seem difficult to implement, the PyCBC module has a build-in function that enables to apply the procedure to two time series. It is used with the *pycbc.filter.matched_filter(S1, S2, PSD, low_freq_cutoff)*, where *S1* and *S2* are the two time series that are matched filtered. In the case considered here, S1 is the template that one wants to test and S2 is the data. The *PSD* is the power spectral density that has been computed before and is an estimate of $\mathscr{R}_n(\omega)$ in Eq.(3.1). The *low_freq_cutoff* is the lowest frequency at which the matched filtering starts. This function returns the complex signal-to-noise ratio of the matched filtering [64]. In order to avoid the increases of the signal to noise ratio due to the wrapping of the signal, we also cut out the first and last seconds of the time series. This is done with the *crop()* function, already introduced before.

The waveforms used are those obtained with the IMRPhenomD model applied to the two sets of parameters. The matched filtering procedure is applied to both in order to investigate the effect of a template that fits the data better. The result can be seen in Fig. 3.3, where we see a forest of peaks. We can understand which is the one corresponding to the event: it corresponds to a high peak in the LIGO-Livingston detector (which has the clearest signature) and to smaller companion peaks that are nearly superposed in the other detectors. In order to be the signature of a matching, these peaks should be bigger than the average of the other peaks that correspond to noise. When computing the signal-to-noise ratio, the peak of the event has the largest value when the parameters are those given by the LIGO-Virgo collaboration, whereas it is less high for the equal-masse model. In the case of the automatic analysis of the LIGO/Virgo data, each peak above a threshold level would lead to a trigger. There would thus be an alarm for both peaks in the LIGO-Livingston data but, since there are no peaks in the other detectors with a high significance, it would not be confirmed as a detection. This shows that the decoupling of the noises from one detector to the other enables one to discard artefacts present in the signal. In addition, as will be explained later, these peaks are re-weighted via a statistical procedure and the remaining peaks will be downgraded to glitches. The result also agrees with the work done by the collaboration, as the best parameters give rise to a higher SNR.

Fig. 3.4 gives a more detailed picture of the SNR in the detectors around the time of the event. One clearly sees the presence of 3 peaks in the signal with a time delay between them
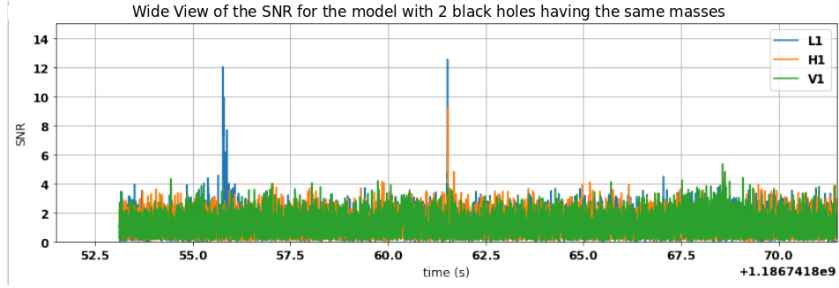
(a) Wide view of the SNR for the template with black holes having the same masses.
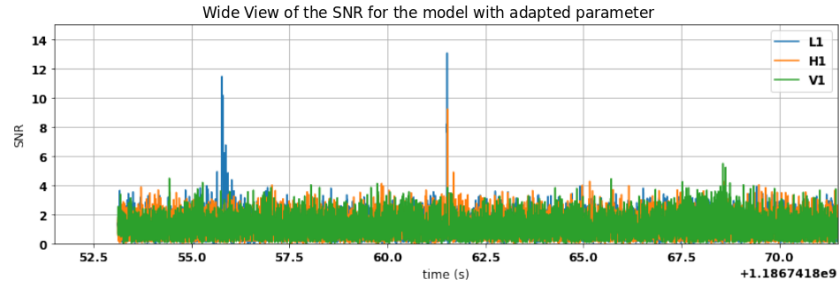
(b) Wide view of the SNR in the case of a system with parameters having the central values given in [7].

Figure 3.3: Wide view of the signal-to-noise ratio in the different cases. We see a glitch in the L1 detector as well as a higher SNR for the case where the parameters are more precise and better fitted to the event.
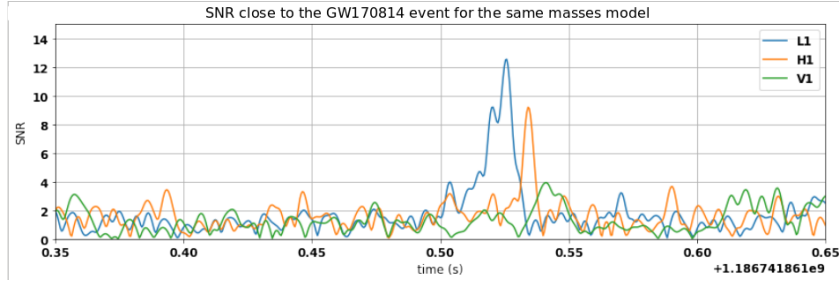
(a) Zoom of the SNR close to the time of the merger in the case of black holes with the same masses.
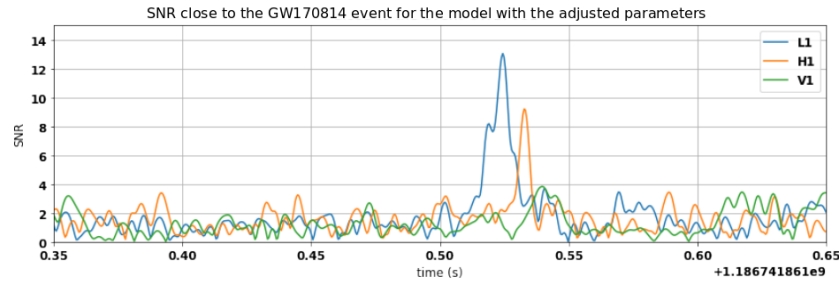
(b) Zoom of the SNR close to the time of the merger for the values of the parameters given in Table 2.1.

Figure 3.4: Zoomed view of the signal-to-noise ratio in the two different cases. We see that there are three peaks, one for each detector, at the time of the event. The two LIGO detectors give a clear signature, whereas the peak in the Virgo detector can be identified only through the presence of the peaks in the LIGO detectors.

Detector	Paper [7]	same-mass model	Parameters equal to the central values given in [7]
L1	13.7	12.4	13.1
H1	7.3	9.1	9.2
V1	4.4	5.3	5.5

Table 3.1: Overview of the different signal-to-noise ratios for different parameters settings. The ones computed in this work are found with the IMRPhenomD template. [7] uses a combination of templates which is not specified.

corresponding to the time needed for the wave to travel from one detector to the other. For both sets of parameters, we see that the two LIGO detectors present a clear peak above the noise, but for the Virgo detector, even in the zoomed case, one can observe several peaks with an amplitude with the same order of magnitude as the peak representing the event. So, the Virgo detector alone could not enable us to conclude that there is a gravitational wave event present. It also shows the importance of a network of detectors where several small peaks can be seen throughout different detectors, showing the presence of an event. For the case of two black holes with the same masses, the values of the peaks are lower than when taking into account more parameters. A comparison of the different SNR's found for the different cases is presented in Table 3.1

If we compare the values, the SNR found are a little lower than the one in [7] for the LIGO-Livingston detector. On the other hand, their values are a bit higher for the two other detectors. Nevertheless, the values found are relatively close to the ones that are reported. One also observes the same trend of decrease in the SNR from one detector to the other, with the same hierarchy for the strength of the signal in the different detectors. So, at this stage, even if the values for the SNR are not exactly the same as those found in the low-latency alert at the time of the detection and the GWTC1 catalogue [9], both the paper and the analysis done are consistent. The small differences that are present are probably due to the fact that some parameters have been set to zero here because their value could not be found in the literature.

Before looking at the significance of the peaks found in the matched filtering process, it is important to note that the smaller peaks present in the SNR time series are due to other transient signals and do not have an astrophysical origin. They can be due to a glitch in the detector or to other noise sources. Such a peak can be seen in Fig. 3.3 for the L1 detector between 55.0 and 57.5 seconds. There exists a test in order to remove these peaks from the data. However, such glitches rarely appear at the same time in the three detectors, e.g. the L1 peak in Fig. 3.3 has no counterpart in the two other detectors. The procedure used to get rid of the glitch in the signal can be found in [8], where a glitch present close to the merger has been subtracted in order to do the analysis.

3.4 Chi-square test

In order to have a numerical estimate of the quality of the fit, we use a chi-square test. This test was first used to veto some peaks not due to a signal but to noise. In this case, the chi-square test discriminates the peaks due to noise from those due to a real gravitational wave signal. The peaks due to noise arise when there is a glitch. Often, when the computations are done and, especially in the case of matched filtering, the noise is assumed to be gaussian. In fact, the noise is not totally gaussian and, in some cases, peaks of noise arise and have a Poisson-like distribution. These can have several causes as explained in the Introduction. In what follows, the mathematical set-up of the test is first explained, based on [33], then applied via its implementation in PyCBC.

3.4.1 Mathematical description of the chi-square test

In order to perform the test, the frequency band of the detector is divided into p smaller bands. So, the wide-band detector is seen as p non-overlapping narrow-band detectors with different frequency ranges such that all the bands put together cover the full frequency range of the detector. For each of them, a matched filter can be computed and one can look if it is compatible with the form of the template falling within the narrow-band. For the calculations done here, the frequency range of the detector is assumed to be $[0, +\infty[$ and is split in p intervals noted $\Delta f_1, \Delta f_2, \ldots, \Delta f_p$ and equal to

$$
\begin{aligned}
\Delta f_1 &= \{f | 0 \leq f < f_1\} \\
\Delta f_2 &= \{f | f_1 \leq f < f_2\} \\
&\vdots \\
\Delta f_{p-1} &= \{f | f_{p-2} \leq f < f_{p-1}\} \\
\Delta f_p &= \{f | f_{p-1} \leq f < \infty\}.
\end{aligned}
\tag{3.2}
$$

These intervals are chosen so that the expected signal contribution from an event is equal in each frequency band. As a consequence, these frequency-bands do not have an equal width.

For what follows, it is helpful to define a set of p different Hermitian products defined as in Eq.(1.24). These are thus given by

$$
\langle A | B \rangle_j = \int_{(-\Delta f_j) \cup \Delta f_j} \frac{A^*(f) B(f)}{\mathscr{R}_n(f)} df
\tag{3.3}
$$

where $j = 1, 2, \ldots, p$ and $(-\Delta f_j) \cup \Delta f_j$ means that we consider the interval for the negative frequencies as well as the positive ones.

With this definition, the Hermitian product defined for the whole detector can be retrieved by summation of each of these p products

$$
\langle A | B \rangle = \sum_{j=1}^{p} \langle A | B \rangle_j.
\tag{3.4}
$$

This is the direct consequence of the linearity of the integral combined with the non-overlapping and complete mapping of the frequency-band of the p narrow-band frequency intervals.

The test is done for waveforms that are assumed to be known and which have a form given by (1.22). The development could also be done in the case of a waveform with the form (1.23) but the case of a known phase does not correspond to reality (the development can be found in [33] for example). For the test, the fiducial time and the distance ratio ($\frac{D}{d}$) are assumed to be known. Based on this, the goal is to perform a statistical test which determines whether the waveform is consistent or not with the signal that is analysed. Therefore, one looks at the behaviour of $z(t_0)$ for the different frequency ranges. In the case treated here, the detector output is given by:

$$O(t) = n(t) + \frac{D}{d}\Big[\cos(\phi)T_c(t - t_0) + \sin(\phi)T_s(t - t_0)\Big] \tag{3.5}$$

where both ϕ and d are unknown. The two templates serving as model in the case of a perfectly located source, T_c and T_s, are supposed to be orthogonal to each other. In addition, they are also assumed to be normalized. So, one has, using the same notation as previously for the Fourier transform,

$$\begin{aligned} \langle \mathcal{T}_c | \mathcal{T}_c \rangle = \langle \mathcal{T}_s | \mathcal{T}_s \rangle = 1 \\ \langle \mathcal{T}_c | \mathcal{T}_s \rangle = 0. \end{aligned} \tag{3.6}$$

When the unknown phase is stationary, the orthonormal approximation becomes exact. When it is not the case, the exact orthonormality can be obtained through a Gram-Schmidt procedure.

In order to find the unknown phase, the idea is to do the filtering for each template individually and combine the two filtered data again. This is done here by combining the two real filter functions into one unique complex function. Therefore, the optimal filter used here is defined as:

$$\mathcal{Q} = (\mathcal{T}_c + i\mathcal{T}_s)e^{-2\pi i f t_0}. \tag{3.7}$$

With this expression and taking the orthonormality relation between both filter into account, the normalization of this optimal filter gives

$$\langle \mathcal{Q} | \mathcal{Q} \rangle = 2$$

.

Combining Eq.(3.5) and Eq.(3.7), the output function is complex and obeys the relation:

$$z = \Big\langle \mathcal{Q} | \mathcal{N} \Big\rangle + \Big\langle \mathcal{Q} | \frac{D}{d}(\cos(\phi)\mathcal{T}_c + \sin(\phi)\mathcal{T}_s)e^{-2\pi i f t_0} \Big\rangle \tag{3.8}$$

It follows that the expectation value of the output is given by

$$\overline{z} = \frac{D}{d}(\cos(\phi) + i\sin(\phi)) = \frac{D}{d}e^{i\phi}, \tag{3.9}$$

which is a complex number. It is such that its modulus corresponds to the distance ratio $\frac{D}{d}$.

Now that these quantities are defined, the p frequency bands are chosen. The templates $\mathcal{T}_c$ and $\mathcal{T}_s$ are assumed to cover the same frequency ranges and to be orthogonal in each of the p narrow bands. As is the case when the full range of the detector is considered, the approximation of orthogonality for each narrow-band becomes exact if the unknown phase is stationary. As a consequence of this assumption and Eq.(3.6), one has the relations:

$$\langle \mathcal{T}_c | \mathcal{T}_c \rangle_j = \langle \mathcal{T}_s | \mathcal{T}_s \rangle_j = \frac{1}{p}$$
$$\langle \mathcal{T}_c | \mathcal{T}_s \rangle_j = 0. \tag{3.10}$$

The signal in a given band is written z_j and is computed exactly as it was for the total frequency band but with the adapted Hermitian product. So one of the p Hermitian products (3.3) is used and one has:

$$z_j = \langle \mathcal{Q} | \mathcal{O} \rangle_j. \tag{3.11}$$

We define p quantities Δz_j that represent the difference between the value taken by the SNR in the jth frequency band and the expected value, hence

$$\Delta z_j = z_j - \frac{z}{p}. \tag{3.12}$$

One can then perform the calculation of the average values for the signal-to-noise ratio in the jth band, its norm squared, the norm squared of Δz_j and the expectation value of the Hermitian product between the conjugate of the output value in one frequency-band and in the total broad-band. The computation returns the values for these quantities [33]:

$$\overline{z_j} = \frac{1}{p} \frac{D}{d} e^{i\phi} \tag{3.13}$$

$$\overline{|z_j|^2} = \frac{2}{p} + \frac{1}{p^2} \left(\frac{D}{d} \right)^2 \tag{3.14}$$

$$\overline{z_j^* z} = \frac{2}{p} + \frac{1}{p} \left(\frac{D}{d} \right)^2 \tag{3.15}$$

$$\overline{|\Delta z_j|^2} = \frac{2}{p} \left(1 - \frac{1}{p} \right) \tag{3.16}$$

It is now possible to define the χ^2 statistic and to explore its properties based on the quantities defined above. What motivates the definition of this test is that the expressions defined previously do not depend on the presence of the signal. The statistic that enables to discriminate between the matching peaks and the glitches is then chosen as:

$$\chi^2 = p \sum_{j=1}^{p} |\Delta z_j|^2. \tag{3.17}$$

For our purpose, it is then useful to know what the expectation value of this test is. Based on

the previous quantities, the calculation gives:

$$\overline{\chi^2} = p \sum_{j=1}^{p} \overline{|\Delta z_j|^2} \tag{3.18}$$

$$= p \sum_{j=1}^{p} \frac{2}{p}\left(1 - \frac{1}{p}\right) \tag{3.19}$$

$$= 2\left(1 - \frac{1}{p}\right) \sum_{j=1}^{p} 1 \tag{3.20}$$

$$= 2p\left(1 - \frac{1}{p}\right) \tag{3.21}$$

$$= 2p - 2. \tag{3.22}$$

It is then also possible to show that, under the assumption of gaussian noise, the χ^2 statistic defined by (3.17) has a chi square statistical distribution with $2p - 2$ degrees of freedom (see for example Appendix A of [33]).

In the algorithm used for the practical computation, the χ^2 statistic is also normalized by the expectation value. So, when the gravitational waveform model matches the data, the statistic has an expectation value of 1. This normalized statistic is written χ_r^2 and its definition is:

$$\chi_r^2 = \frac{\chi^2}{2p - 2}$$
$$= \frac{p}{2p - 2} \sum_{j=1}^{p} |\Delta z_j|^2. \tag{3.23}$$

The value of 1 is obtained only in the case of a perfect matching between the waveform and the signal, which is never the case as the sought signal is swamped in noise and the observed signal is a mix of signal and noise. Therefore, the χ_r^2 statistic often approaches this value but does not reach it at the time of the event. This is observed in Fig. 3.5, which is computed for the GW170814 event for the two different models.

At the end, the normalized chi-square statistic is such that it is expected to have a value of one when the signal and the template match and a larger value when there is a mismatch. In addition, it is also equal to one when there is only gaussian noise [65].

3.4.2   Practical computation of the chi-square test

The description above can seem a bit difficult to put in practice as it implies a lot of operations. For the computation, we can use the *pycbc.vetoes.power_chisq(template, data, n_bins, psd, lowest_freq)* function which calculates the chi-square statistic based on the template and the data (first and second arguments) we want to match. The *n_bins* argument corresponds to the number of bins used for the computation. The choice of the number does not follow theoretical considerations but is found through numerical simulations. The value used here is 26 [65]. The next is the PSD of the detectors. *lowest_freq* is the lowest frequency cut-off, hence the lowest

frequency that is used for the definition of the bins. One can also specify the highest frequency for the bins but, for the present computation, no upper limit was used on the frequency. This function returns a time series with the value of the chi-square statistic for each time. In order to avoid the problem of wrapping the data at the level of the length of the filter, one also crops the first and last times of the series. The statistic is then normalized by the number of degrees of freedom.

The normalized chi-square statistics defined above and computed for each model is represented in Fig. 3.5.
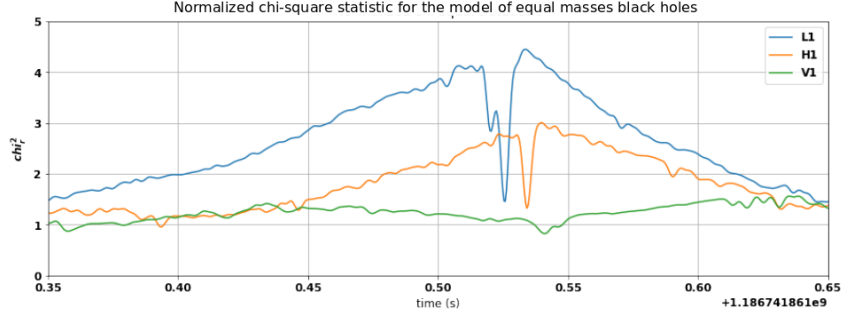
(a) Chi-square statistics close to the time of the merger in the case of black holes with the same masses.
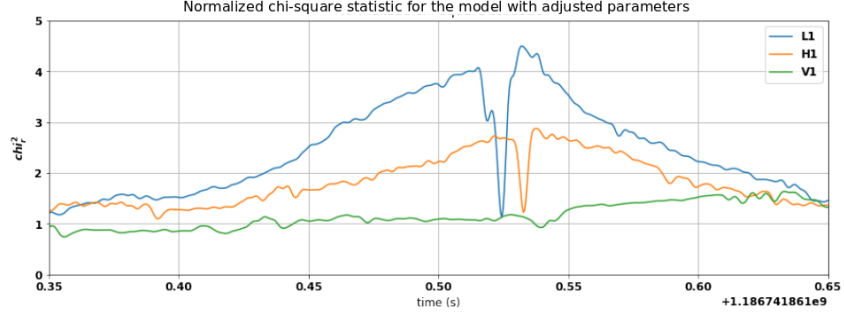
(b) Chi-square statistics close to the time of the merger for the model built with the central values given in Table 2.1.

Figure 3.5: Chi-square statistic for the two different models. We see that the test is closer to one in the case of the more adapted model. Moreover, the statistical behaviour is better in the LIGO detectors than in the Virgo detector.

The statistic is expected to be close to unity when the data matches the template. In both cases, the dip in the value found is well marked in both LIGO detectors. As was the case before, the statistic seems to be even better when the parameters from the LIGO-Virgo collaboration are used. So, the results are consistent with those of the collaboration. Here, we used only the central values. Allowing a variation within the error bars would produce a slightly better fit. For the Virgo curve, the dip in the value of the statistic is less marked but is still present

The general picture for each chi-square curve also shows an increase of the value before a quick drop to the minimum value at the time of the merger. This is a result of the gliding of the template relative to the data. Indeed, one can imagine that if the template matches best at

the centre, then before and after, when the superposition is only half done, it is the worst case, leading to a mismatch and an increase of the statistic.

By doing this kind of analysis, it is possible to illustrate the importance of different parameters as best results are found when they are chosen correctly. Each parameter leads to a modification of the template and the fit is well done only if the parameters are adjusted correctly.

The influence of the mass can be seen in Fig. 3.6, where, for the SEOBNRv4 model, one mass was kept fixed (at $30M_\odot$) whereas the second mass was free to change.
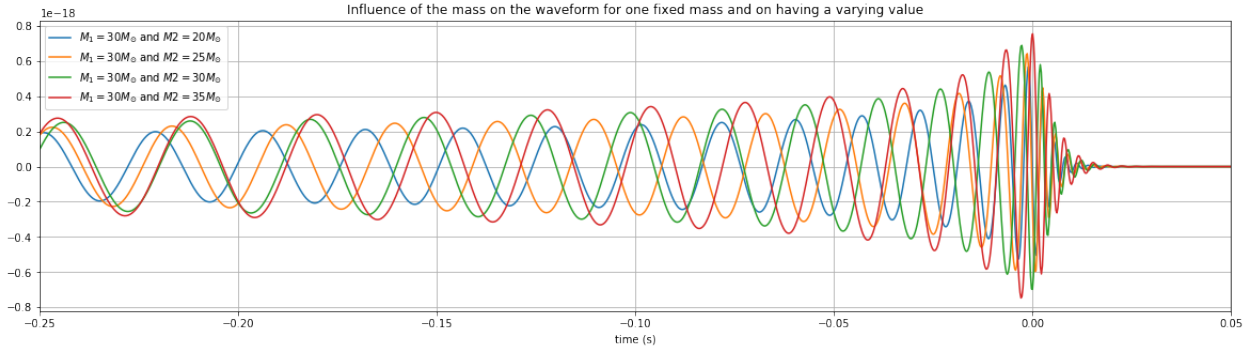
Figure 3.6: Variation of the waveform for the SEOBNRv4 model. We see that the amplitude, as well as the frequency are modified, from the inspiral to the ring-down phase.

Fig. 3.6 shows that if the masses vary within the range of values given in the paper [7], the waveform also varies so that it is possible to find an optimal value for the matched filtering.

The spin along the z-axis is also a key parameter, as can be seen in Fig. 3.7. It shows how the waveform can vary when the value of the spin is changed: the masses and the distance are fixed at the value given in [7], whereas the value of the spin along the z-axis is kept at the value given in GraceDB for the first black hole, while the value of the spin along the z-axis for the second black is varying. One can clearly observe that there is an influence of the spin on the waveform. Therefore, in order to find the correct fit, it is important to consider both masses and spins. So, when we want to find the correct parameters of an unknown event, we have to explore all the possible parameter combinations, leading to a huge search space, needing very powerful computers.

3.5   Down-weighting of the SNR

The SNR can be further manipulated and down-weighted at times that do not correspond to the matching with a signal. This gives a better view of the peak around the event by decreasing the importance of the peaks in mismatching regions, such as the spurious glitch peak. The idea is to scan the value of χ_r^2 over time and redefine the value of the output based on this value. Even if the SNR can present peaks at other times than that of the matching between the model
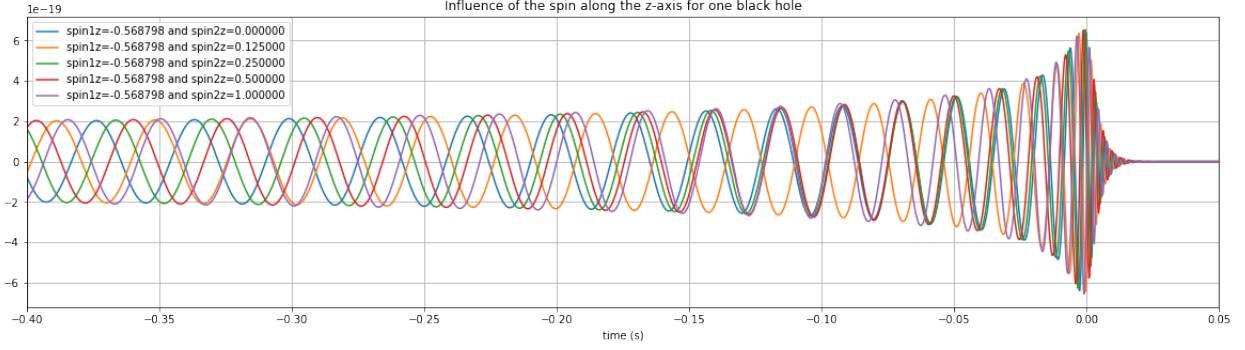
Figure 3.7: Variation of the waveform for the SEOBNRv4 model. The amplitude of the signal is not varying that much from one case to the other but the frequency is, as we can observe by the shift of the maxima from one case to the other.

and the data, the statistic is close to one only for a good matching between the template and the data. Therefore, after the normalized chi-square statistic has been calculated, we redefine the value of the SNR for all frequencies depending on the value of the statistic at that time.

We take then:

$$\hat{z}(t_0) = \frac{z(t_0)}{[(1 + (\chi_r^2)^3)/2]^{\frac{1}{6}}} \quad if \quad \chi_r^2 > 1 \tag{3.24}$$

and we keep the original value when $\chi_r^2 \leq 1$.
This relation is chosen empirically. The re-weighting is done when the statistic is higher than one since it is supposed to be equal to one when there is effect of the noise [66].

This new weighting of the statistic has the advantage to give a good separation between the background and the signal. In addition, $\hat{z}$ does not take higher values than z, even if the value of the χ_r^2 statistic is lower than one. The statistical values of the peak will be calculated based on the reweighed values [67].

Once more, the PyCBC library has a build-in function which enables us to compute the time series with the down-weighted value of the statistics. It corresponds to the function *pycbc.event.ranking.newsnr(snr, chi)* where *snr* is the signal-to-noise ratio time series that one wants to reweigh and *chi* corresponds to the time series of the chi-square statistic corresponding to the SNR. This function returns a time series which is the reweighed SNR given above. The results of this manipulation can be seen in Fig. 3.8, where they have been calculated for the two different models considered in this chapter.

Once the reweighing manipulation has been done, the time series that are found do not show the big noise peaks any more. The only remaining peak above the others for all the detectors corresponds to the event. By comparing Fig.3.3 and Fig.3.8, one can observe that the glitches have been removed, since the second big peak that was present in the LIGO-Livingston detector has been taken away. This confirms that this peak is not due to the matching with the template that was tested but was, in fact, a glitch in the detector. In other words, the peaks around the event keep more or less the same weight whereas the others are taken away. The small decrease in strength for these peaks is due to the output signal of the detectors being made of

56
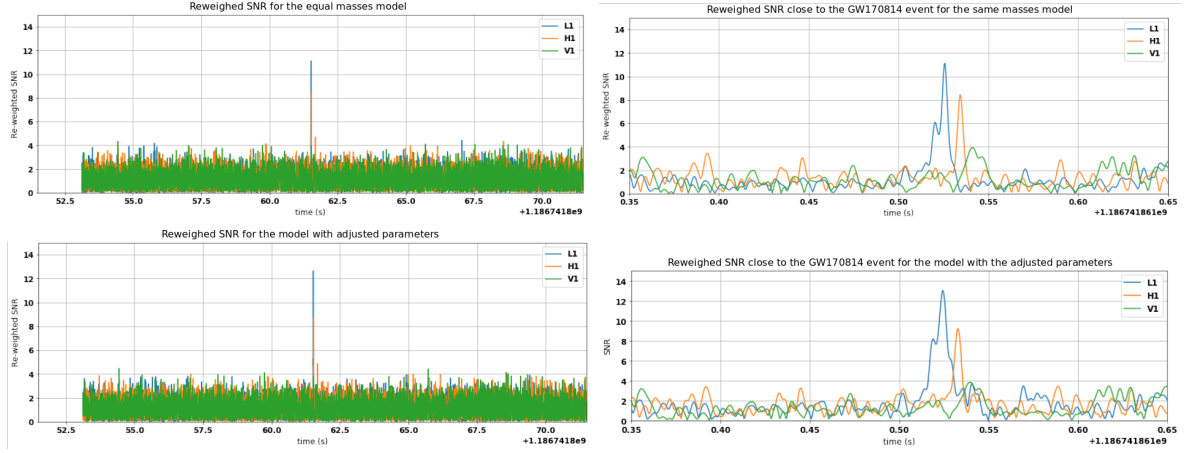
Figure 3.8: Reweighted SNR. The row above corresponds to the same-mass model and the one below to the different masses. The left column is the wide view and the right one is the view zoomed on the time of the event. We see that the glitch has been removed by the down-weighting of the noise. The decrease of the event peak is more important for the same-mass model than for the one with the correct values, as the chi-square test is worse in that case.

Detector	Paper [7]	Same-mass model	Parameters set to the central values given in [7]	Down-weighted case for the same-mass model	Down-weighted case for the adjusted parameters
L1	13.7	12.4	13.1	11.1	12.9
H1	7.3	9.1	9.2	8.2	8.8
V1	4.4	5.3	5.5	3.8	3.9

Table 3.2: Table comparing the SNR given in [7] and the SNR's found during the different computations, for the reweighed and non-reweighed cases.

the superposition of the signal and the noise, which gives a chi-square test a bit higher than 1. In addition, the hierarchy keeps on being respected for both models and the model where the correct parameter values are used is still the best. Thus, this down-weighting gets rid of most of the artefacts that are present due to noise. Note that the model with the same masses undergoes a bigger SNR decrease at the time of the event, as it fits less well the event and has a higher chi-square value at the time of the merger than the model with the adjusted parameters.

3.6   Calculation of the background and significance

In order to further confirm that the peak is due to a gravitational wave, one can look at the background and the statistical significance of the peak relative to the background. For this computation, the statistical significance is tested for the Virgo peak, to which a p-value will be

assigned. First, one checks whether its position in time agrees with that of the peaks that have been detected in the LIGO detectors.

The test is done in a frequentist statistical approach of hypothesis testing. We have a null hypothesis (noted H_0) and an alternative one (noted H_1). H_0 corresponds to noise, whereas H_1 corresponds to a gravitational wave event. In order to be able to do the test, the null hypothesis has to have a known statistical behaviour. In the case studied here, this is not analytically defined but it can be found numerically through the analysis of the background.The p-value represents the probability that the event is due to noise. So, the gravitational wave hypothesis can be accepted if the p-value is (very) low [68].

First, in order to find the p-value of the Virgo peak, we define a window, called the *coincidence window*, where the peak should be found based on the time of flight of the wave from one detector to the other. The window is the time interval in which the Virgo peak can be found based on the times of the peaks present in the two LIGO detectors. We then calculate the value of the peak in this window, which is the highest SNR value. In order to find the probability that the peak has this value only due to noise, we compare it with the value of the peaks found outside of the coincidence window. This scanning is done by letting a window with the same width than the coincidence window glide over the data. For each position of this window, the value of the highest peak is calculated. If this value is higher than that of the peak in the coincidence window, it is kept in memory. So, each time a value higher than the peak of the signal is found, we add a unit in the count of these higher peaks. At the end, the probability that the spike present in the coincidence window is only due to noise is found by dividing the total number of peaks with a higher value found by the total number of windows that have been scanned.

Now that the theoretical approach has been detailed, the numerical computation and results can be explained. Once again, instead of computing manually the time delay from the Virgo detector to each of the LIGO detectors, PyCBC proposes a build-in function that enables to calculate it: *pycbc.detector.Detector(D1).light_travel_time_to_detector(Detector(D2))*. *D1* is the detector from which one wants to start (V1 in the computation done here) and *D2* is the arrival detector (H1 or L1 for the computation). This function returns the time needed to travel from the *D1* detector to the *D2* detector, when going at the speed of light. Once these times are obtained, one demarcates the region for each of the two American detectors. The peak must then be present in the region where both regions overlap. This corresponds to the coincidence window and is the darkest region in Fig.3.9. One sees that the Virgo peak is indeed found in this region. It is this peak for which the significance is calculated. Fig.3.9 is taken for the equal-mass model. The corresponding figure for the different masses is similar, as the window depends on the time position of the peaks and not their exact values. An interesting way to represent the information calculated for the p-value is to plot the values of the peaks found in the noise and the p-value for the on-source data. This gives Fig. 3.10.
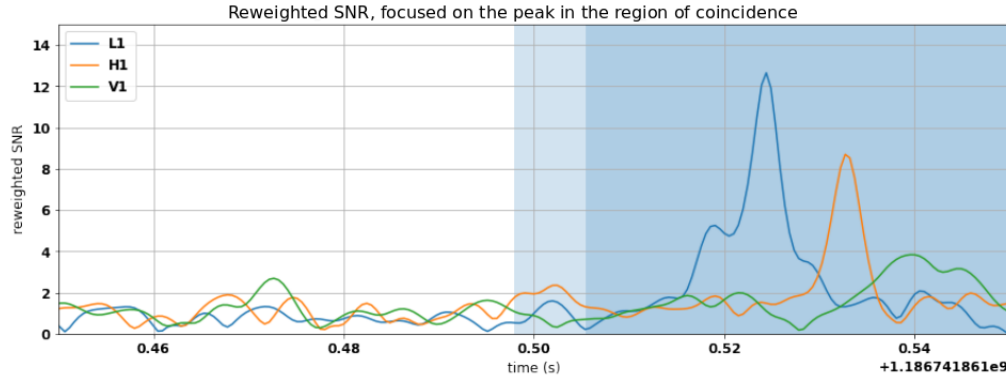
Figure 3.9: Coincidence region for the equal mass models. The darker region corresponds to the coincidence window, in which the Virgo peak is consistent with the times of the peaks in the two American detectors.
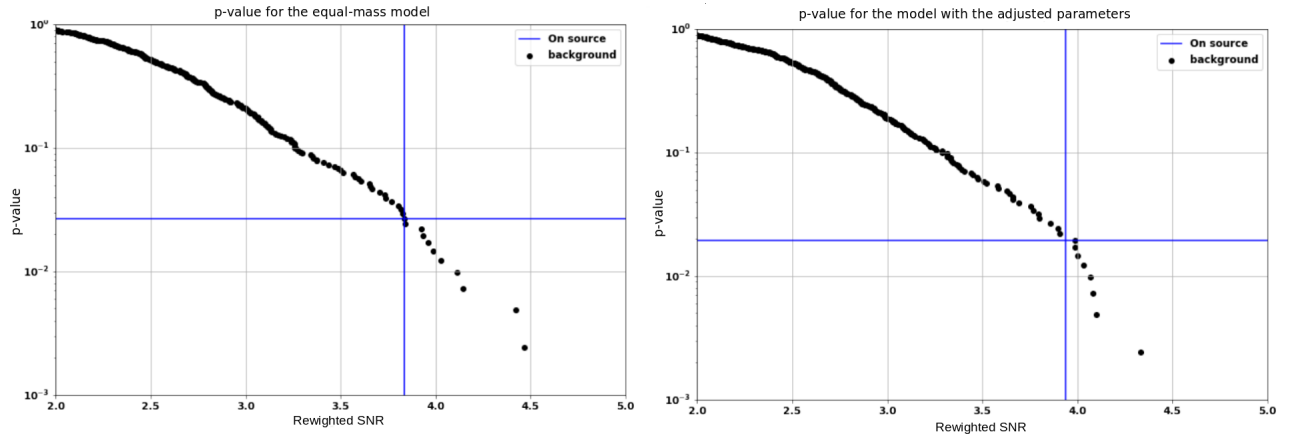
Figure 3.10: Graph of the peak values for all the windows with the on-source peak superposed, left for the equal-mass model and right for the different-mass model. The vertical line corresponds to the value of the peak found in the Virgo detector and the horizontal line shows the corresponding p-value. The p-value is lower for the adjusted model, making it even less probable to have been generated by noise instead of gravitational wave.

The p-values that have been found are 0.7% and 0.4%, respectively for the same-mass model and for the different-mass model. Those values are higher than the one given in the paper [7], which is 0.1%. The values found here are not the best because the models that are used are simpler than those of the paper, which optimized several other parameters and considered many more templates. That means that all the parameters are fine-tuned with respect to the detection. Note also that the value is higher for the same-mass model. This shows that the analysis done in this work, even if it digs less deep in the data, is coherent with the analysis that have been done by the LIGO-Virgo collaboration. Finally, even if the signal in the Virgo detector was not good enough to help in the parameter determination, it increases the statistical significance of the event.

3.7 The false-alarm rate

The false-alarm rate, noted FAR, is a statistic that is used to rank the events. It assesses how often events that are "louder" than (with a higher SNR) or equivalent to the event of interest occur, using a comparison with time shifted analyses [69].

For each detector, we have defined the reweighed SNR in Eq.(3.24). In order to compare the events, we combine the individual SNR into a *coincident SNR* by taking:

$$\hat{z}_c = \sqrt{\sum_{detectors} \hat{z}_{detector}^2} \tag{3.25}$$

where the sum is over all the detectors for which there is an SNR available.

The FAR is found by computing this statistic for time shifted data windows outside of the coincidence window and comparing them with the value found for the actual event. This ensures that there are no events in coincidence in the detectors.

This ranking value will depend on several parameters, more particularly on the template due to the non-gaussian behaviour of the noise, as well as the the detectors working during the detection of the gravitational wave [69]. The parameters are:

1. the total mass of the binary system, noted M,

2. the detectors that participate to the coincidence, noted P,

3. the detectors that are not vetoed, noted F[3],

4. the combined reweighed SNR rank of the event, noted R.

The total mass is divided into several bins and M gives the mass bin under consideration (3 bins where used for the 2 first LIGO scientific runs [69]). R is defined for the different time-shifted events and the event of interest by assigning the value 0 to the event with a given F,P and M that has the lowest combined SNR, 1 to the one with the next lowest value, etc. until all the events have a rank that is assigned. The FAR is then defined as the number of events that have a rank higher than the detected event, divided by the total time analysed in the shifted analysis (written T_A) [69]:

$$FAR_{PFMR} = \frac{\sum_{R_{ev} > R} Event_{PFMR_{ev}}}{T_A} \tag{3.26}$$

where $Event_{PFMR_{ev}}$ indicates an event found in the shifted analyses with a given mass bin, a given ranking and given detector status.

---

[3]The difference between P and F comes from the fact that the detector can have a peak that is present for the event and used for the coincidence but that is vetoed under some conditions. For example, the SNR could be too low for a single detector but become higher because of a peak present in the other detectors

However, it is more useful to have a FAR that depends only on the detectors that are working at the time of the event (the F parameter). If the ranked events are written $Event'_{PFMR_{ev}}$, the FAR becomes:

$$FAR_{FR} = \frac{1}{T_A} \sum_{R_{ev}>R} \sum_P \sum_M Event'_{PFMR_{ev}}.$$

(3.27)

This statistic can be seen as the time frequency of events with a SNR at least as high as that of the detected gravitational wave event produced only by noise [69].

Based on the FAR, it is possible to define the false alarm probability (FAP), which gives the probability to have an event that is louder than the one of interest and produced only by noise. It is given by:

$$FAP_{FR} = 1 - \exp(-FAR_{FR}T_A)$$

(3.28)

where we assume a Poisson statistic [69].

This statistic is important, as it is often used in the presentation of the events by the collaboration (see for example [6, 7, 8, 9]). However, it has not been computed in practice here, as it requires to do the full analysis for each of the time-shifted data slices that are considered and is computationally expensive.

Chapter 4

Finding the best fit parameters for the event

In this chapter, a Bayesian approach is used to infer the best-fit parameters for the event. Therefore, a prior, a likelihood, and a posterior are computed. First, only the likelihood is maximized. Secondly, the posterior is as well. Even though this approach can be adopted for all the parameters that enter the computation of a waveform, here it is used for the masses, the spins, the distance and the position in the sky to be less computing-power expensive. First, the fitting is done on a single detector to explain the concepts and the algorithm used. After that, the aim is to tune better the parameters by using the network of detectors to find the parameters and the position[1].

4.1   One detector: LIGO-Livingston

For the single detector best-fit approach of the parameters, the LIGO-Livingston detector, where the event is best seen, is used. The first operation to perform is to access the data and whiten them. This is done exactly as has been shown in Section 2.5 where the whitening technique is explained. After that, one computes a model template that is compared with the data. The maximization of the likelihood will then enable us to have a template that matches as well as possible the data, hence giving the most probable values for the parameters.

In the case of a single detector, the localization on the sky is not accessible, as it requires a sensitivity to the polarization or a triangulation base, which are not accessible for a single detector. Nevertheless, the model depends on the masses, the spins, the distance, the time, and the inclination. Because the fitting is done in the time domain, the model used to make the waveform is *SEOBNRv4*. It corresponds to the model already described in Section 3.2 [32]. An example of a waveform obtained with this model and using the central values for the parameters given in [7, 9] can be seen in Fig. 4.1. One can see that the waveform model used in this part

---

[1]This section is based on the examples of the LIGO collaboration that can be found at `https://github.com/gw-odw/odw-2018/tree/master/parameter_estimation`.
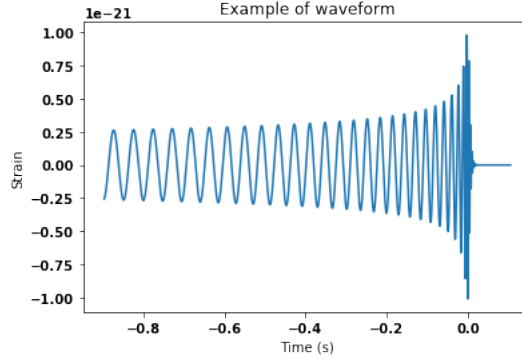
Figure 4.1: Waveform obtained with the SEOBNRv4 model for masses of 31 and 25 solar masses for the merging black holes and other parameters having the central values given in [9]

of the work is not the same as before when the model used was IMRPhenomD. It is convenient to use it here as it directly gives the template as a function of time. The waveform is made here with the *get_td_waveform( )*, which returns the plus and the minus polarization of the wave. One can see that the command is a bit different here as in the section dedicated to the models, as the waveform is made directly in the time domain. Here, only the plus polarization is used in order to fit the data, as only one detector is used. The inclination cannot be assessed as it is degenerate with the distance of the binary system. So, the distance that is given in this case is that of the merger when it is perfectly oriented above the detector.

Another crucial computation is that of the PSD. Indeed, in order to know if the model and the data fit well, the algorithm consists of the subtraction of the model from the data, followed by the comparison of the residuals with a model of the noise present in the detector. If the model and the data are similar, the subtraction should lead to only noise remaining in the signal. Here, in the simple computation that is performed, it is the power spectral density of the detector that is used as a model for the noise. In fact, the PSD models the noise perfectly under the condition that the noise is gaussian (with a zero mean) and second-order stationary. For the case analyzed above, the total duration of the sequence is 32 seconds, which means that the noise can be approximated as stationary. In the end, the PSD computation is done with Welch's method described in section 2.4 [48]. In the case of a *"real"* data analysis, more complex methods are used, such as *BayesLine*, where the posterior distribution function for the PSD is computed based on an MCMC (Markov Chain Monte-Carlo) [70]. However, here, the computation of the PSD is done with the PyCBC build-in function *.psd(time_slice)*, which calculates it by computing the average of the power spectral density for sub-sets of data with a fixed width [48]. The method with the MCMC is not used for this work because it is very CPU-expensive and is not mandatory to have satisfactory results. The PSD that is obtained using this method for a width of 4 seconds can be seen in Fig. 4.2. It is our noise model for this section of the work.

The PSD is also used in the computation of the whitened data, after the data is converted to a frequency series. This is easily done in PyCBC through the *.to_frequencyseries( )* command, which one then divides by the square root of the PSD.
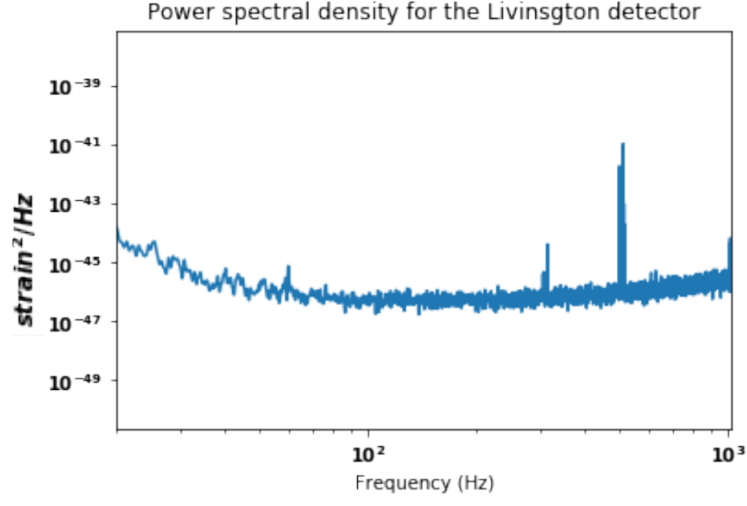
Figure 4.2: PSD for the Livingston detector, used as noise model for the determination of the parameters.

The next step is to define the likelihood of the detector. This function represents the probability to observe the data when the parameters determining the waveform have a given value. If the data is perfectly modeled by the computed waveform, then, once the model is subtracted from the data, there is only noise remaining. So, the likelihood is the measure of the probability that the residuals come from the noise. This can be done because the only probabilistic component present in the data is the noise itself. Mathematically, the inner product is written

$$\langle A|B \rangle = 4 \Re \left(\int_0^\infty \frac{A(\omega)B(\omega)}{\mathscr{R}_n(\omega)} d\omega \right) \tag{4.1}$$

where $\mathscr{R}_n(\omega)$ is the power spectrum of the noise.

If $\vec{\theta}$ is the array containing the parameter guesses, the likelihood for the template is the probability that the residuals come from the noise process:

$$p(data|\vec{\theta}) = \exp\left(-\frac{1}{2}\langle h(\vec{\theta}) - d|h(\vec{\theta}) - d \rangle\right), \tag{4.2}$$

where d represent the initial data.

The likelihood for the "noise only" hypothesis gives

$$p(data|n) = exp\left(-\frac{1}{2}\sum_{data}\langle data_i|data_i \rangle\right) \tag{4.3}$$

The left-hand-side of Eq.(4.3) corresponds to the probability to have the subtracted data given the values n for the noise. It corresponds to the definition of the likelihood given previously. It is used to divide the likelihood of the template given the data, giving the likelihood ratio. Because of the exponentials present in the right-hand-side of Eq. (4.2) and Eq.(4.3), instead of directly working with the likelihoods, one works with their logarithm, called the log-likelihood. In the algorithm, we maximize the log-likelihood ratio, which is the ratio of Eq.(4.2) over Eq.(4.3). In
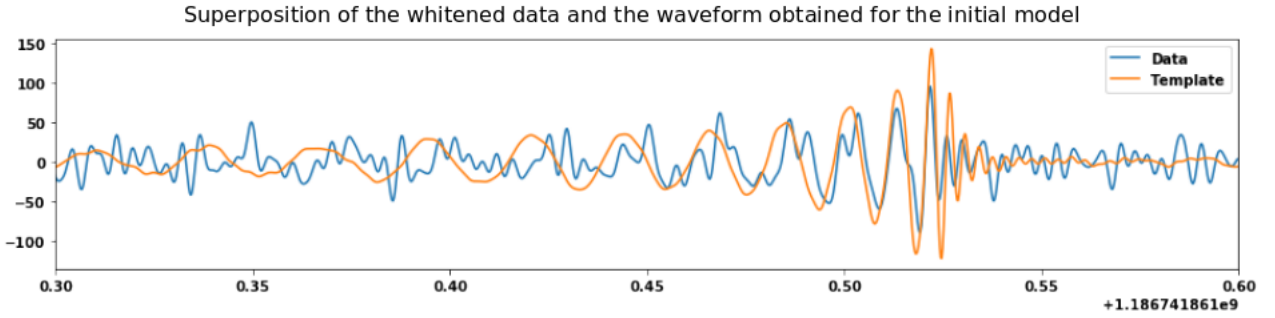
Figure 4.3: Superposition of the data and the initial template that will be adjusted for the L1 detector alone. This template represents the starting point of the minimization procedure.

practice, is done by taking the fast Fourier transform of the data. Then, a template is generated with the parameters fixed at the values that should be tested. After that, the log-likelihood ratio is calculated as half of the difference between the inner product of the template with itself and two times the inner product of the template and the Fourier transform of the data.

Once this is done, it is possible to try one single template, made with the central values of the parameters given in [9]. So, we take an initial array of values with masses of 31 and 25 solar masses, a distance of 580 Mpc and spins of -0.5687 and 0.1308. The log-likelihood of this parameter set can then be calculated. Later on, the parameters will be adjusted and the likelihood will change. Indeed, as the parameters are fitting the data better, the value of the log-likelihood should increase. The superposition of the model obtained with the initial array of values can be seen in Fig. 4.3. In this figure, we see that using the central values of the paper for some parameters and setting the others to zero, the waveform matches relatively well the signal by eye. Nevertheless, one can observe that there is a slight mismatch between the model and the data. This can be understood by the fact that there is no indication about the position of the source with respect to the detector. So, the optimal case is taken as if the source was put perfectly above the detector.

The next step is to maximize the likelihood or, equivalently, the log-likelihood. This is done here by minimization of the opposite of the log-likelihood. In order to do so, one uses the *minimize* function which is present in the *scipy.optimize* package. This function takes as arguments the vector of parameters that should be optimized, the function that has to be minimized, the starting values, and the method.

The method used is the Powell method [71], which is useful when the derivatives of the function that is adjusted are not accessible. Besides, it is also able to converge even if the initial values of the parameters are ill-posed. It is a conjugate direction method. The procedure is as follows: one starts from the best-known approximation of the minimum p_0 and searches down x linearly independent directions, written $\xi_1, \xi_2, ..., \xi_x$. For each $k = 1, \dots, x$ we compute $\delta_k = argmax(f(p_k + \delta_k \xi_x))$ and define the next parameter values as $p_{k+1} = p_k + \delta_k \xi_k$. Next, for each $k = 1, \dots, x - 1$, we define the new directions as $\xi_k = \xi_{k+1}$. This iteration is done until $||p_n - p_0|| < \epsilon$, where ϵ is the precision required for the estimate. This procedure converges with a good rate, even if the initial approximation is not good [71].
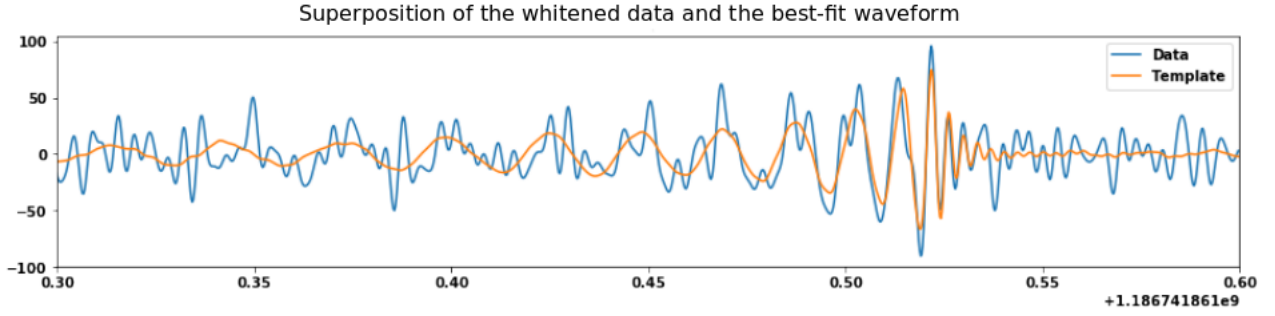
Figure 4.4: Adjusted template superposed to the data for the Livingston detector. We see that the global oscillations of the data are better followed and that the waveform looks a lot like the signal without the fluctuations due to the noise.

The use of Powell's method is suited in our context, as the starting values are not that well known, as the error bars given in [7, 9] show, and the function to minimize has no accessible derivatives. Moreover, in practice, the initial values that are found for the parameters come from the search of the maximum SNR by iterating over the parameter space. In the case of a single detector, the fitting enables us to find a template that reproduces quite well the data as can be seen in Fig. 4.4. This procedure also returns the values of the masses, which are 31.12 and 25.01 solar masses for the starting masses of the two merging black holes. On the other hand, the masses which are presented in Table 2.1 are $30.7^{+5.7}_{-3.0}$ and $25.3^{+2.9}_{-4.1}$ solar masses [7]. This means that the masses found with the minimization procedure are in the range given in the official catalog. So, this simple procedure is convincing. On the other hand, the distance found by this procedure leads to a distance of 1214 Mpc which is well beyond the range given in [7]. The difference comes from the fact that we do not account for the localization of the system nor its inclination.

In Fig. 4.4, one can see that the superposition of the data and the template is relatively good. At least, it is closer than for the first case shown in Fig. 4.3. So, one can say that the matching has improved. Indeed, the two curves follow the same pattern and have more or less the same amplitude around the time of the event. This shows that the minimization procedure has worked well because the difference between the gravitational wave signal of the detector and the template has decreased. The differences that remain are faster fluctuations of the signal, which are due to the noise.

An extra way to see if the model fits well the signal is to subtract the adjusted template from the data for the Livingston detector and take the Q-transform of the result. This is then compared with the Q-transform of the original data of the detector. As has been explained in section 2.6, dedicated to the Q-transform, and as can be seen in the Fig. 4.5, the gravitational wave signal in the data gives an over-density. If the signal is well modeled by the template, the subtraction should lead to the disappearance of this signature. Fig. 4.5 shows this clearly, which means that the simple model taken for a single detector leads to a relatively good model for the GW170814 merger in the LIGO-Livingston detector. In fact, the Q-transform shows some variations (seen through the changes in color at some places) that corresponds to the noise in addition to the signature of the merger. The subtracted case presents these patterns as well but not the yellow over-density due to the gravitational wave. This shows that the subtracted model is consistent
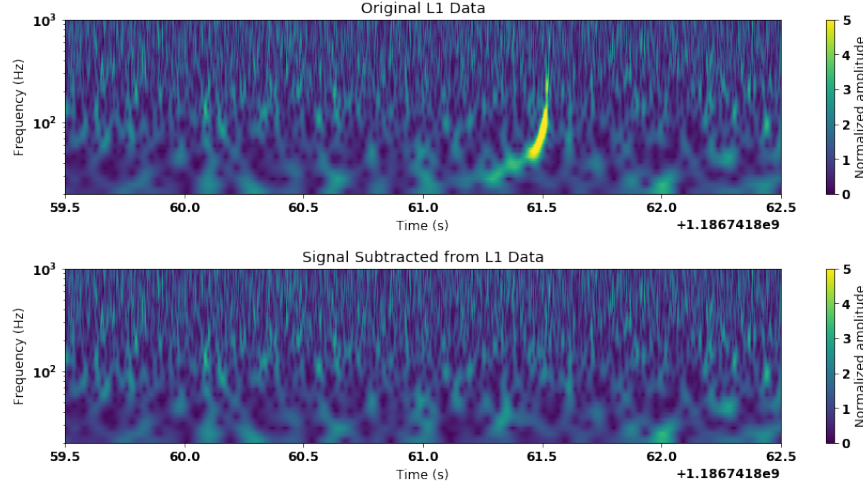
Figure 4.5: Above, the Q-transform of the raw data and below, the Q-transform when the model template is subtracted from it. We see that the banana-like shape of the gravitational wave signal has been subtracted well and that the only patterns remaining in the second Q-transform are similar to the noise fluctuations.

with the hypothesis that the residuals are only due to random noises.

4.2 Several detectors

As has been said in the previous section, where only one detector was considered, there is no possibility to have some inferences about the distance of the merger or its coordinates (right ascension and declination). Therefore, in this section, the case where 2 or 3 detectors are used is considered. Moreover, the constraints on the other parameters can also be improved by the use and combination of several dataset. The process is the same in the case of two or three detectors.

The first steps are the same as for one detector. So, the raw strain is downloaded and filtered. Also, the PSD for the different detectors is computed and is also used as a model for the noise. As was the case for the single detector case, it is also done with the PyCBC build-in command *.psd()*. The result of this operation gives, in the case of 3 detectors, a figure similar to Fig. 2.4. After that, the data for each detector is whitened to have a flat PSD response, exactly as has been done for 1 detector.

The main difference that appears, in this case, is the generation of the template. Indeed, in the previous section, only the masses, the distance, the spins, and the time are needed to generate the template. Here, some extra parameters are needed, such as the position in the sky, given in terms of right ascension and declination. These parameters can now be investigated thanks to the time delays between the detectors. When only one detector is used, the signal is detected as a mixture of the two polarization but those cannot be disentangled. On the other hand, the presence of several detectors enables us to have a sensitivity to the two polarizations of the

67

wave. Moreover, the time delay between the detectors enables us to have a base from which triangulation can be performed. So, the distance that could be found for several detectors is not, as was the case for a single detector, the distance if the source is perfectly above the detector but the distance for a given direction in the sky. An extra point that can be stressed is that, because all these parameters intervene directly in the optimization process and the generation of the waveform, they are changing the waveform. As a consequence, the waveform that each detector should see is different.

The template generation can be decomposed into two parts. The first is the same as for one detector but including the extra parameters in *get_td_waveform(approximant, parameters, f_lower, delta_t)*. This corresponds to the geocentric waveform. After that, the results found for both polarizations have to be combined with the antenna pattern of the detector, which is dependent on the localization of the source. This enables us to find the waveform that is seen by one particular detector, given the parameters and the localization. The waveform respecting the antenna patterns can be obtained directly with a build-in function of PyCBC. This function is *detector.antenna_pattern(right ascension, declination, polarization, time_of_event)*, where *detector* can be L1, H1 or V1. So, this function takes into account the position of the merger as well as the time delay between the detectors. This returns two arrays with the antenna pattern. The waveform perceived by one detector is then found by summing the two polarizations multiplied by their antenna pattern. The mathematical development is shown below [72].

The antenna pattern of the detectors is thus a way to take into account the geometry of the problem and explain how the waveform can change from one detector to the other for the same event at the origin. Understanding this is enough to do the computation. Nevertheless, it can be interesting to go a bit deeper into this concept.

Using the notation of [72], the detector can be considered as being in the $x - y$ plane, with the arms along the x and y axes. The gravitational wave can come from any direction, described with spherical coordinates relative to the detector axes, noted θ and ϕ. The two polarizations of the wave are h_+ and $h_\times$, which are defined relative to the axes in the plane of the sky, rotated by an angle ψ with respect to the axes of the detector. This geometry can be seen in Fig. 4.6.

Using this geometry, the response of the detector to the strain is given by

$$\frac{\delta L(t)}{L} = F_+(\theta, \phi, \psi)h_+(t) + F_\times(\theta, \phi, \psi)h_\times(t) \tag{4.4}$$

where the two functions F_+ and $F_\times$ are the antenna pattern functions of the interferometer. Starting from the geometry shown in Fig. 4.6, on can show the following expressions in the case of a single detector [72]:

$$
\begin{aligned}
F_+ &= \frac{1}{2}(1 + \cos^2(\theta))\cos(2\phi)cos(2\psi) - \cos(\theta)\sin(2\phi)\sin(2\psi) \\
F_\times &= \frac{1}{2}(1 + \cos^2(\theta))\cos(2\phi)cos(2\psi) + \cos(\theta)\sin(2\phi)\sin(2\psi).
\end{aligned}
\tag{4.5}
$$

Now that the concept has been explained for one detector, it is important to transfer this to a network of detectors, which is the case we are interested in. To compute this, the assumption
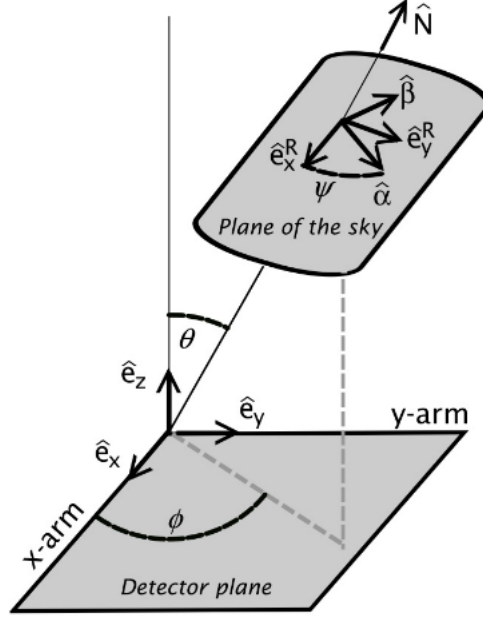
Figure 4.6: Geometry of the detector and the gravitational wave. The detector is in the $x - y$ plane with its arms aligned on the axes. The h_+ and $h_\times$ polarization of the gravitational waves are defined with respect to the axes defined in the plane of the sky, inclined and rotated with respect to the detector axes. Taken from [72]

that the noise is uncorrelated between the different detectors is made. In the case of detectors located at different sites, which is the case for the LIGO-Livingston, LIGO-Hanford, and Virgo detectors, this assumption is rather well respected, except in the case of major seismic events for example. To find the antenna pattern for each detector constituting the network, one needs to define common coordinates for all the detectors. The individual antenna pattern of a detector is then transformed into these common coordinates. These are chosen as Earth-centered spherical coordinates, noted (θ, ϕ). The source position is given in these coordinates and the wave polarization angle, ψ, is aligned with the spherical-coordinate grid. Additionally, the latitude and longitude of the detector are noted β and λ respectively. The orientation of the detector is also important. It is taken into account with the angle χ, corresponding to the angle with the axis pointing towards East measured in the trigonometric direction. For several reasons, such as design conception or topographic constraints, it may happen that the angle between the two arms is not exactly 90°. In all generality, it is written η. If one assumes that the celestial coordinates are aligned with the latitude and longitude so that the equators coincide for both systems of coordinates and that the celestial point (corresponding to $\theta = \frac{\pi}{2}, \phi = 0$) is in the zenith direction of the geographic location of each detector, then, the antenna pattern of one detector is given by [72]:

$$
\begin{aligned}
F_+ &= \sin(\eta)[a\cos(2\psi) + b\sin(2\psi)] \\
F_\times &= \sin(\eta)[b\cos(2\psi) - a\sin(2\psi)]
\end{aligned}
$$
(4.6)

with the a and b functions given by the expressions

$$a = \frac{1}{16} \sin(2\chi)[3 - \cos(2\beta)][3 - \cos(2\theta)] \cos\left(2(\phi + \lambda)\right) +$$
$$\frac{1}{4} \cos(2\chi) \sin(\beta)[3 - \cos(2\theta)] \sin\left(2(\phi + \lambda)\right) +$$
$$\frac{1}{4} \sin(2\chi) \sin(2\beta) \sin(2\theta) \cos(\phi + \lambda) +$$
$$\frac{1}{2} \cos(2\chi) \cos(\beta) \sin(2\theta) \sin(\phi + \lambda) +$$
$$\frac{3}{4} \sin(2\chi) \cos^2(\beta) \sin^2(\theta)$$

(4.7)

and

$$b = \cos(2\chi) \sin(\beta) \cos(\theta) \cos\left(2(\phi + \lambda)\right) -$$
$$\frac{1}{4} \sin(2\chi)[3 - \cos(2\beta)] \cos(\theta) \sin\left(2(\phi + \lambda)\right) +$$
$$\cos(2\chi) \cos(\beta) \sin(\theta) \cos(\phi + \lambda) -$$
$$\frac{1}{2} \sin(2\chi) \sin(2\beta) \sin(\theta) \sin(\phi + \lambda).$$

(4.8)

The two functions F given in Eq.(4.6) correspond to the antenna pattern that is computed with the built-in function of PyCBC. Our algorithm will thus compute the strain for each detector, taking the antenna pattern into account.

After the waveform has been computed for each detector, we must find the best-fit parameters by maximizing the likelihood. Given the assumption that the noise in the detectors is independent from one detector to the other, the network likelihood is the product of the single-detector likelihoods. Therefore, the log-likelihood is the sum of the individual log-likelihoods. In practice, for the computation and the maximization of the likelihood, the process is the same, except that, when the log-likelihood is computed, it is first done individually for each detector and the results are summed. By using this method for the GW170814 event and the two LIGO detectors, one obtains a curve shown in Fig. 4.7. It shows that the parameters found fit the data well. In this case, the two masses, the distance, the position on the sky, and the spins along the z-axis have been inferred. The values found are $31.1 M_\odot$ and $25.0 M_\odot$ for the two initial black hole masses, $602\,\mathrm{Mpc}$ for the distance. The position on the sky of the source has a right ascension of $0.66 = 2\,\mathrm{h}\,30\,\mathrm{min}$ and a declination of $-0.84 = -48°49'$. The spin components along the z-axis are -0.5665 and 0.1308 for the first and the second black hole respectively. Once again, these values have to be compared with the data given in [9], which are $30.7^{+5.7}_{-3.0} M_\odot$ for the masses, and $25.3^{+2.9}_{-4.1} M_\odot$ and $580^{+160}_{-210}\,\mathrm{Mpc}$ for the distance. The position in the sky has a right ascension of $03\,\mathrm{h}\,11\,\mathrm{min}$ and a declination of $-44°57'$ and the spin components are -0.5688 and 0.130793 for the first and second black hole. For the coordinates, the errors are estimated to be of the order of 5 to 10 degrees on the position, as can be seen on the skymaps in [7]. So, the values found in the simple computation above agree with the results published in the catalog [9]. The computations performed here can, indeed, be called simple, as they are done in a straightforward and less CPU-expensive way than what is done by the LIGO-Virgo collaboration.
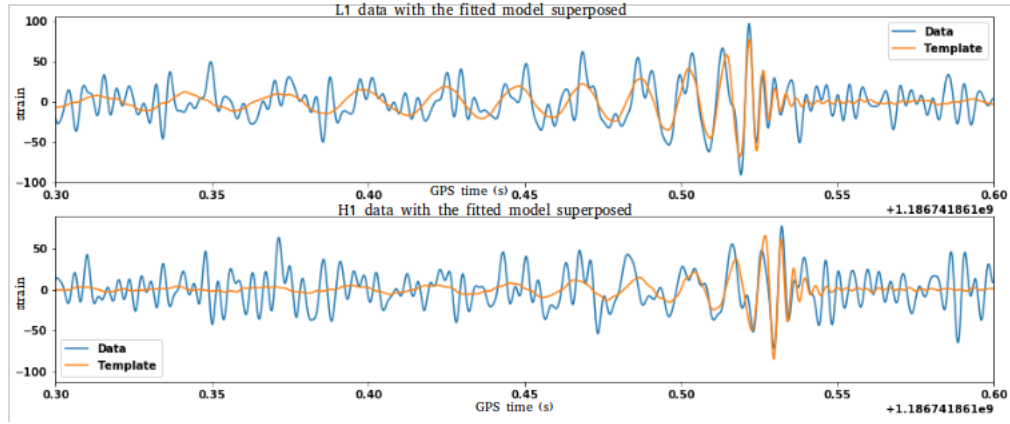
Figure 4.7: Above, the superposition of the data and the model for the LIGO-Livingston detector and bellow, the superposition for the LIGO-Hanford detector. We see that the waveforms found follows well the signal in both detectors.
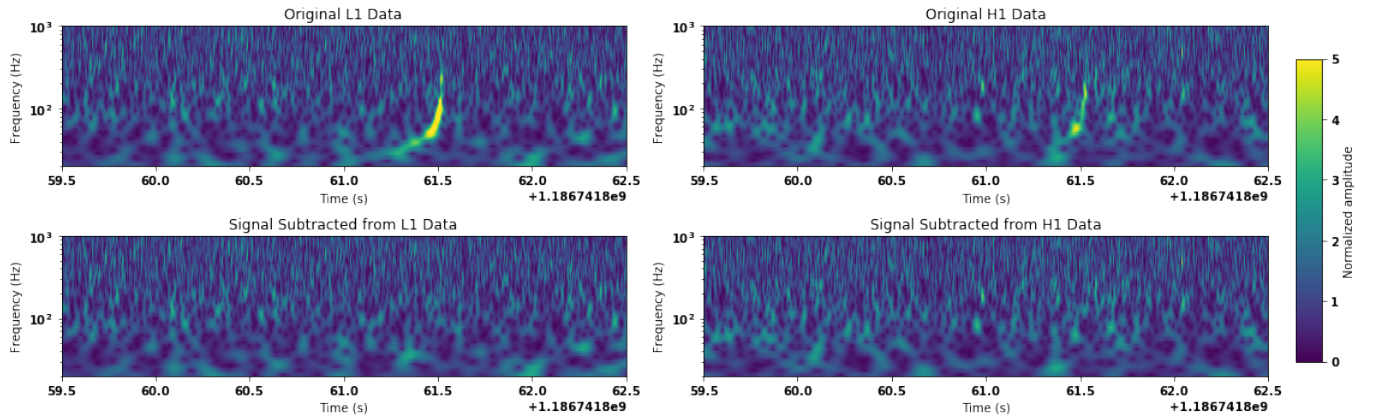
Figure 4.8: Left, the data for the Livingston detector and right, for the Hanford detector. Above, the Q-transform of the raw data and below that of the data where the model has been subtracted. We see that the signature of the event present at the start has been subtracted well.

71
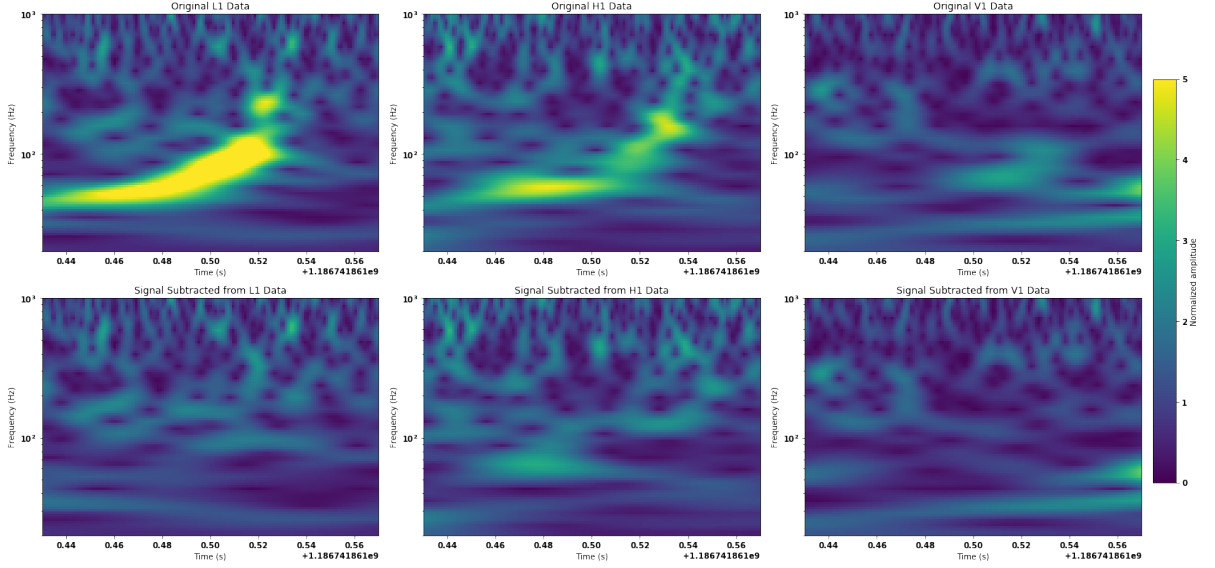
Figure 4.9: Left, the data for the Livingston detector; in the middle, the Hanford detector; right the Virgo detector. Above, the Q-transform of the raw data and below that of the data where the model has been subtracted. We see that the patch in the Virgo detector is not that well identifiable as a gravitational wave signal (it is not a banana-like shape). Nevertheless, in the three cases, the signal is well subtracted. There are still some faint over-densities remaining. However, those are not higher than the noise and are thus consistent with the noise.

Similarly to the single-detector case, one can also compute, for each detector, the Q-transform of the data as well as the Q-transform of the data where the model template has been subtracted. In Fig. 4.8, one sees that the signal is well present in the raw data and is effectively subtracted with the model that is computed through maximization of the likelihood. It is the case for both detectors, where the final Q-transform corresponds to noise only.

The approach used for the LIGO detectors can also be applied to the three-detector network. The computation is done in the same way, using the antenna pattern of the detectors and the time of flight between them. The problem here is that the signature of the event is not that easy to see in the Virgo detector. Therefore, the figures obtained in this case are more difficult to interpret. Nevertheless, we did the computation to have an inference on the parameters. As can be seen through the analysis of the results, the parameters that are the most impacted by the use of the third detector are the coordinates giving the position in the sky. They become closer to what has been found in [7]. Indeed, the use of the Virgo detector in addition to the two LIGO ones enables us to have a better definition of the antenna pattern. The third detector gives a base for triangulation, helping to find the position of the source in the sky. The values that have been found for the different parameters can be found in the Tab. 4.1.

Again, we consider the three Q-transforms before and after subtraction. This is shown in Fig. 4.9. The banana-like shape of the event in the V1 detector is only a very faint overdensity with respect to the rest. This shows that the signature of the event is not well defined in this detector. Still, one can see that it disappears once the model is subtracted from the data, as was the case for the 1- and 2-detector models. For the two other detectors, the signature is also

Parameter	L1 detector only	LIGO detectors	L1, H1 and V1
Mass 1 (in $M_\odot$)	31.12	31.14	31.14
Mass 2 (in $M_\odot$)	25.01	24.99	24.99
Luminous distance (in Mpc)	1214	602	618
Spin 1z	/	-0.5665	-0.5688
Spin 2z	/	0.1308	0.1331
Right ascension	/	2h30min	2h36min
Declination	/	-48°49'	-47°25min

Table 4.1: Table summarizing the value of the different parameters that have been inferred during the minimization procedure. These have to be compared with the values given in the table 2.1

subtracted. In addition, as can be seen in Tab. 4.1, the values found are in accordance with those given in the literature.

As can be deduced from the computation above, the maximization of the likelihood is enough to find the central values for the masses, the distance, the position, and the spins. But, it is possible to go further and be more precise by using the other important quantities that exist in the Bayesian approach. The final goal here is to find the *posterior density function* of parameters, which represents the probability distribution for all the parameters. The Bayes theorem gives the formula [70]

$$p(\theta|observations) = \frac{p(\theta)p(observations|\theta)}{p(observations)} \tag{4.9}$$

for the posterior, where θ corresponds to the unknown parameters and *observations* is the data, hence the strain. In this expression, $p(\theta)$ is called the *prior*, which represents the knowledge one has of the parameters before any observation. The term $p(observations|\theta)$ in the numerator is the likelihood, already used above. It corresponds to the probability to observe the data if the parameters in the model have the values θ. The denominator $p(observations)$ is called the *evidence*. It is a normalization factor and is useful when a comparison with another model has to be made but can be forgotten in the case of parameter estimation.

In fact, it is the logarithm of the posterior that will be maximized. The first thing to do is to define the prior. The case where only the likelihood is used is equivalent to adopting uniform priors for the parameters. This assumption makes sense for some parameters such as the time and the phase of the merger. On the other hand, for other quantities, one has some expectations: the sources of coalescence signals are expected to be uniformly distributed, which can be included in the prior. This is translated by a mathematical constraint on the declinations

$$p(\alpha, \delta) \propto \cos(\delta) \tag{4.10}$$

where δ is the declination and can take any value between $\frac{\pi}{2}$ and $-\frac{\pi}{2}$. This prior can also be expressed as a condition that depends on the luminosity distance D and the inclination ι of the

binary. This condition is

$$p(D, \iota) \propto D^2 \sin(\iota). \tag{4.11}$$

Taking this into account, the log-prior is then computed as

$$logprior = \log(\cos(\delta)) + 2\log(D) + \log(\sin(\iota)). \tag{4.12}$$

Finally, the log-posterior can be computed. According to Eq.(4.9), it corresponds to the sum of the log-prior and the log-likelihood of the network. The best-fit parameters can then, again, be computed by maximization of the log-posterior. This can again be done with the optimization function that is build-in in *scipy.optimize*. Using the log-prior, one ensures that the estimates of the parameters are consistent with their expected values.

4.3   The error bars of the estimated parameters

In the two previous sections, we found a point-like estimate of the parameters. Besides, this estimate was made only for a few parameters. Normally, the total number of parameters, for a binary black hole merger, is 15: the 2 initial masses for the black holes, their 2 spin magnitudes, the 4 black hole spin directions, the 2 angles describing the orientation of the orbit, the 2 angles giving the sky localization of the merger, 1 luminosity distance, 1 phase and 1 time of coalescence. When the computation is made by the LIGO-Virgo scientific collaboration, all these parameters are inferred. In addition, the error bars on these quantities are also computed.

One possibility is the use of a Markov-chain Monte-Carlo (MCMC) procedure. This leads to a statistical distribution for the posterior of the different parameters, giving the error bars around the central value that is found through the maximization process. The most common way to do this Markov Chain Monte Carlo is the Metropolis-Hastings algorithm [73]. In this method, a chain of points, corresponding to a representative sample for the posterior, is found in the long-term limit. First, a posterior $p(\theta|D, I)$ is defined. Then, one defines a proposal density, which is a symmetric function. Starting from the proposition θ_i one draws the next proposition θ_{i+1} and computes the acceptance ratio

$$A = \frac{p(\theta_{i+1}|D, I)}{p(\theta_i|D, I)}. \tag{4.13}$$

If $A \geq 1$, the proposed value is more likely and θ_{i+1} is added to the chain. On the other hand, if $A < 1$, then an extra step is needed. We draw a uniform random number r and check whether $r < A$. If it is the case, the drawing θ_{i+1} is added to the chain. Otherwise, θ_i is added again to the chain. To have a distribution, several samples of θ are considered, so that there is a series of estimations for each parameter. These make up the distribution inferred for the parameter in question [73].

Even if the procedure is not that difficult to implement, it is CPU-intensive (essentially due to the high number of parameters that should be adjusted) and will not be pursued here. In Python, there are some build-in functions for the implementation of an MCMC, such as *emcee* [73].

Chapter 5

Investigation of effects leading to variations in the analysis

In this chapter we look at the impact of the variations of some parameters on the results of the analysis. So, we let one of the parameters vary and see how the PSD and SNR are changed.

5.1 Value of the time slice in the PSD computation

As has already been stressed in Section 2.4 dedicated to it, the PSD is a crucial ingredient to detect the signal, as it is used as a model of the noise. To find the best-fit template for the signal, this characteristic must be as precise as possible. In this section, we look at the influence of its computation on the results. For example, we look at the effect of the variation of the duration of the time slices used for Welch's method on the elements of the analysis (shape of the PSD and SNR). The data used here is still the one directly given in PyCBC. Therefore, the PSD is computed for data slices with a duration of 32 seconds. As a consequence, it is not possible to take a time slice with a duration longer than 32 seconds. Moreover, since Welch's method is a calculation of FFT on smaller parts of the data, the case where the time slice is taken as the total duration of the data corresponds to the fast Fourier transform of the complete sequence.

5.1.1 Shape of the PSD

First, we can look at the change of the shape of the PSD as the time slice used is modified. In Fig. 5.1, one can observe how it evolves in the LIGO-Livingston detector starting from a time slice of 0.0032 seconds (which is $\frac{1}{10000}$ of the total signal) and ending at 32 seconds (corresponding to the full duration), multiplying each time the duration of the considered time-slice by a factor 10 from one step to the other.
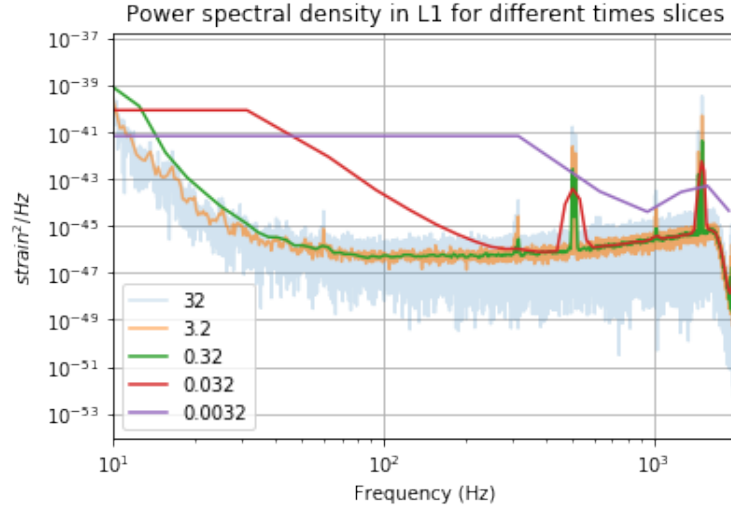
Figure 5.1: Evolution of the PSD for different time slices. We see that the bigger time slices lead to more details.

One can see that, as the time slice used increases, the details that can be found increase as well. Indeed, for 0.0032 s, the curve has a plateau until more or less 300 Hz before decreasing and having a peak above 1000 Hz. This shows that this time slice could not be used to evaluate the noise. The working frequency range in a given detector is marked by a flat part in the PSD. This part does not correspond to the one that is seen for the shortest time slice. By looking at the time slice of 3.2 s, which is the closest to the times used in the previous sections and recommended in the LIGO tutorials, one can see that this plateau ranges from 30 Hz to 1000 Hz. The same analysis is also applicable in the case of the 0.032 s time slice, even if the decrease starts earlier and if a second peak appears around 500 Hz. However, the plateau that should be present is still not there. When taking a time slice of 0.32 s, the curve begins to look like the curves used for the computations done previously. However, as can be seen in Fig. 5.2, it is still quite a smoothed version of it and some peaks are still missing. There is also a mismatch for the lower frequencies, where the value of the PSD is higher for the smallest time slice. The absence of some peaks can be problematic in some cases. For example, it is important to note that the peak at 60 Hz is missing, which is the peak due to the alternating current used to calibrate the data. If this peak is not present, it means that it cannot be used to calibrate the data. Furthermore, it also means that some frequencies in the noise are not modeled. Therefore, if one used the PSD made with the 0.32 s time slice at least one known peak has disappeared, but there are probably others, less known, that have also been removed, which can lead to errors in the analysis.

It has been said that a 3.2 s time slice is the closest duration to what is used in the LIGO tutorials. When looking at Fig. 5.1, one observes that the PSD taken with the 32 s time slices has the most details. What is wanted is a model of the noise, which allows to see where some frequencies are peaking out to remove them. The full FFT gives an image of all the frequencies present and has high variability. The interest of Welch's method is to estimate the PSD faster and using less memory storage than performing the complete Fourier transform [48]. The memory storage and speed are not that influenced here as the chosen time series are
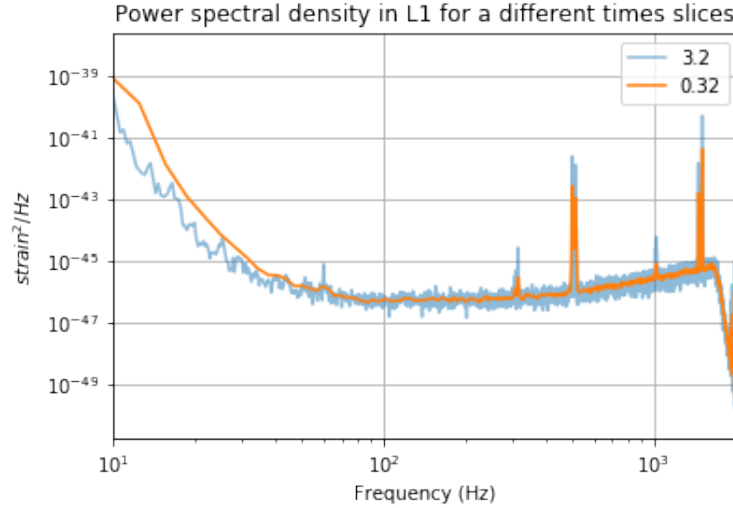
76

Figure 5.2: PSD for a time slice of 3.2 s and 0.32 s. We see that the 0.32 s case is smoother and that some peaks are removed, making it a worse model for the noise.

relatively short. However, in some cases, longer periods can be used to analyze the frequency content in the detector, and the advantage brought by this method become important.

Mathematically speaking, taking smaller time intervals amounts to taking bigger frequency bins. This explains the difference that can be observed in all the curves. Indeed, when the two shortest time intervals are used, wider frequency bins are used. This explains why there is a high plateau appearing for the lowest frequencies. Indeed, as has been said earlier, there is a lot of low-frequency noise that cannot be avoided. When computing the PSD with large frequency bins, all these noises that fall within the range covered will be associated and averaged in this bin, giving a high value. On the other hand, the use of a larger time scale for the computation enables us to have a better frequency resolution, explaining the numerous details present for the 32 s time slice. As a consequence, the many noises that are present in the lower frequencies give a global increase but it is less steep as the different contributions in frequencies are more distributed among the bins. This difference in resolution also enables us to understand how the peaks can become more visible with larger time scales. When a periodic signal is present at a fixed frequency, its contribution should be strong only for one precise frequency bin. But, when the time resolution increases, the frequency resolution does the opposite. Therefore, the power of a given frequency will be spread on a larger range, giving a flatter and wider peak.

To be consistent, the analysis done above must also hold in the case of other detectors. It is the case because the PSD's that are found for different times show the same types of curve shapes for all the detectors. This can be seen in Fig. 5.3, where the change of the PSD curve with the time slice used to compute it is the same. One also sees that the curve of the Virgo detector shows more peaks in the higher frequency domain for lower values of the time slice. These results come from the higher noise level present in this detector. It is also why the smaller and thinner peaks are more numerous in the case of a larger time slice. So, this difference in feature does not come from a different reaction of the data but is simply due to the difference in noise content for the detectors.
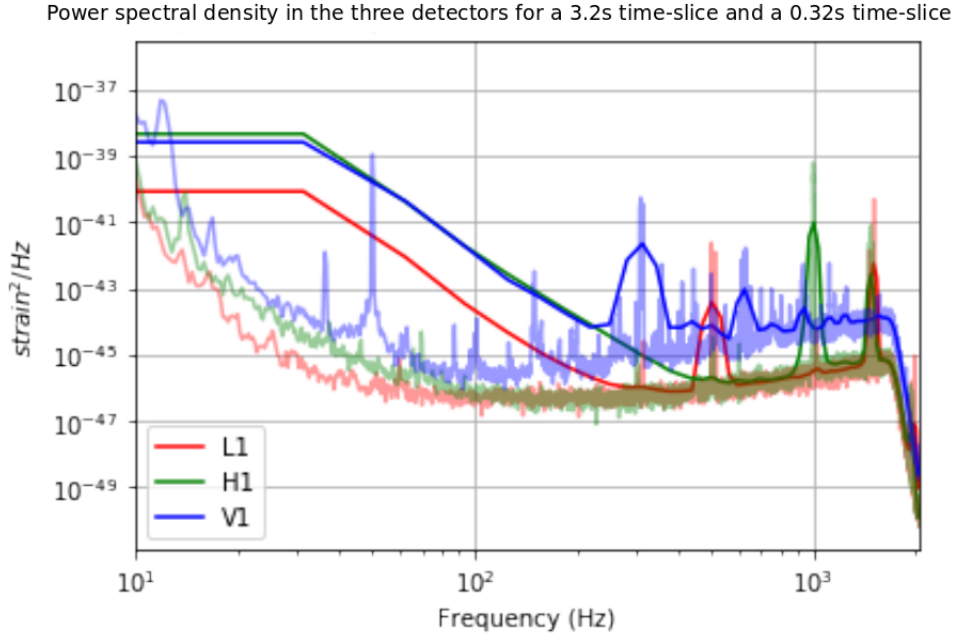
Figure 5.3: PSD variation in the three detectors for a time slice of 0.032 s (corresponding to the curves with fewer details) and 3.2 s (corresponding to curves with more details). We see that the three detectors react in the same way for different time slices. More peaks are present in the Virgo detector for both cases, due to the higher noise level present at the time of detection.

The computation of the PSD can also be made for different events to see if the response keeps on being the same. It has been done in this work and the features are the same for all the events. The figures are similar with some peaks being slightly more pronounced for one event or the other. The only major difference is for events coming from two different runs for the LIGO detectors. Virgo being active only in the second run, it cannot be taken into account for such a discussion. Indeed, between the first and the second runs, the sensitivity of the detectors has been improved for the lower frequencies. Therefore, the noise at these frequencies has been reduced as well as other noise sources [74]. So, between the data of the first and of the second run, some peaks have been taken away from the PSD spectrum, and the flat plateau where the detectors work best has been taken down and has been widened.

5.1.2 Value of the SNR

The PSD enters in the computation of a noise model, which in turn is used in the computation of the SNR using matched filtering. To see its influence, we compute the SNR in the case of two black holes with the same masses, as has been done in the previous sections (this model is chosen because the code goes a bit faster than for the other). In the previous chapters, the time slice was taken as having a value of 4 seconds, without overlap and using the Hann window. Here, only the time slice will be changed in the SNR computation, the other parameters are kept fixed.

First, we look at time slices with values from 1 to 20 s, by steps of 1 s, for the LIGO-Livingston detector, and the GW170814 event. An immediate observation is that for longer durations, the SNR gives a forest of peaks with higher values, even at places where the SNR should not be that high. Once the time slice has a duration of more than 19 s, the signal-to-noise ratio peak that should be present at the time of the event is not there anymore. In addition, there seems to be a decreasing trend for the SNR peak value at the time of the event when the time slice becomes longer. In Fig. 5.4, the SNR curve found for a 15 s and for a 20 s time slice are compared in a wide view. This shows clearly that the value of the time slice in the PSD has a consequent influence on the result. Indeed, for the biggest time slice, no signal can be found as the value of the signal-to-noise ratio does not show a clear peak. On the other hand, in the second case, a peak is present. However, one sees that the glitch peak that has been described in earlier parts of the work has a higher value than the one corresponding to the signal. Moreover, the value of the SNR found at the time of the event for the 15 s time slice is around 9.5 and is significantly lower than the value found for a time slice of 4 seconds, where the value was 12.4. This simple analysis also shows that the value of the SNR that is found depends on the value of the time slice taken for the PSD.
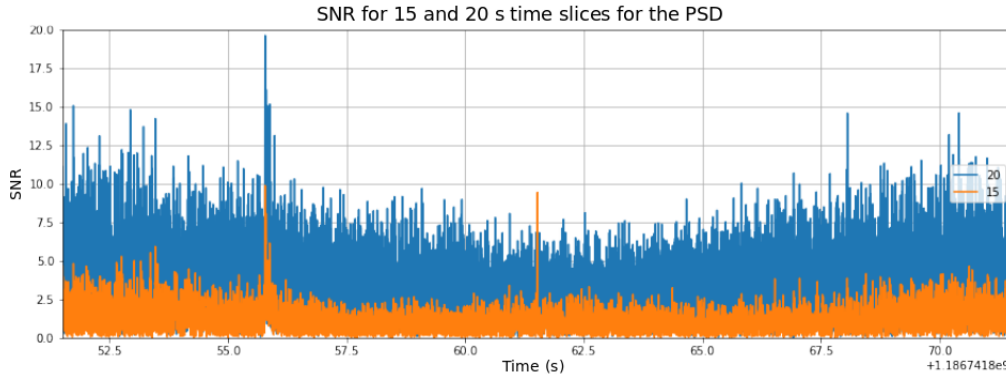

Figure 5.4: SNR for time slices of 15 s and 20 s. We see that the peak for the event cannot be seen anymore in the 20 s time slice data and a peak is only present at the time of the glitch. For the 15 s case, the glitch is higher than the SNR at the time of the event, but the latter is still present.

When looking for the significance of a peak and calculating the signal-to-noise ratios, a chi-square test was performed and used to reweigh the SNR. The goal was to get rid of the eventual peaks which were due to glitches in the detector. The test was performed for different time slices to see if, after reweighing, a peak could be found around the time of the event. The chi-square statistic is not good at all for the 20 s time slice. Indeed, it has a more or less constant value close to 6 everywhere, showing that, in this case, no peak is detected. The chi-square curve obtained in the case of the 15 s time slice looks a lot like the one already obtained in the case of the previous tests, even if the drop for the peak corresponding to the event is less important (we do not reach a value of 1), which shows that the matching is not as good. After that, based on this test, the reweighing is done. The spectrum is made less noisy in the case of both time slices, as can be seen in Fig. 5.5. However, for the longest time slice, there is no peak at all at the time of the event and the only peak that seems to appear is the one that is related to the glitch. In addition, for the 15 s time slice, the noisy part is decreased but the glitch peak is not
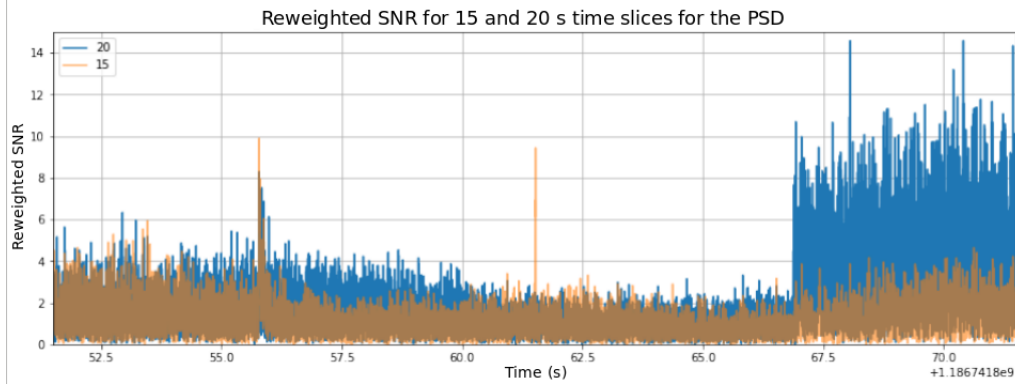
Figure 5.5: SNR for time slices of 15 s and 20 s, reweighed by the chi-square statistic. We see that for the 20 s time-slice, no event can be found and there is only a peak for the glitch. In the 15 s case, the glitch peak is still slightly higher than the event peak but the latter can still be found. We have much higher values that can be found further because there the down-weighting has not been done. This should not be looked at here.
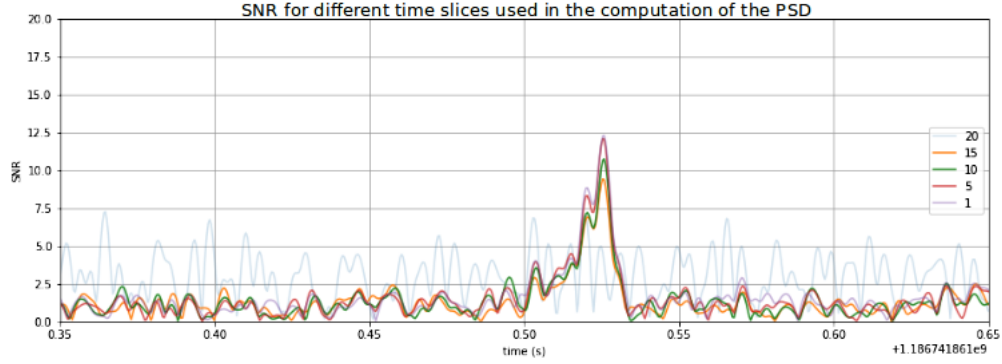
Figure 5.6: SNR for different values of the time slice used in the PSD computation, zoomed on the time of the event. We see that there is a decreasing trend as the time-slice becomes longer.

removed and keeps on having a higher value than the peak that should correspond to the event

According to Fig. 5.5, nothing is enabling us to conclude that there is an event. Moreover, if a peak would indicate an event, the first that one would look at is the one corresponding to the glitch as it has the highest significance (and is present in both cases). The second highest peak is for the 15 second time slice and corresponds to the event. But, it has a lower value than the one found for the 4 s time slice used in the basic approach depicted previously. So, this computation and these figures show that the time slice chosen for the computation is important as it can influence the value of its SNR and the trigger of an alert for the presence of the event.

The decrease of the signal-to-noise ratio as the value of the time slice decreases, is not totally true because there is an optimal value corresponding to a maximum SNR peak. Fig. 5.6 shows the evolution of the SNR that is found for a fixed event (still GW170814) and with the same window but changing the value of the time slice when the PSD is computed. The SNR curve is still computed for the simple model with equal masses.

Fig. 5.6 shows that the peak is not present for a time slice of 20 s. One also sees that the value found for the peak depends on the time slice that has been chosen. In this example, it is the highest for the shortest possible time. However, by looking at the SNR for other times, one can observe that the maximum value for the peak happens when the time slice is equal to 2 s, where the SNR has a vlue of 12.6 instead of 12.45 for 1 s. It is larger than the one that was found in the analysis, with a time slice of 4 s used in the computation, where the value found was 12.4. To see if the result found is consistent throughout different analyses, we look at the evolution of the SNR with the length of the time slice for different events. These are all analyzed in the same conditions as the previous one. The events are GW150914, GW151012, GW151226, GW170608, GW170104, GW710809, GW170818, GW170823 and GW170729. All of these have been analyzed with the equal-mass black hole model, where the mass is each time taken to be the mean mass of the two black holes given in [9]. In each of these cases, the 2 s or 3 s time slices gave the best results. Note that, in some cases (GW151226 and GW170823), the difference between the two times could not be determined . For other cases, 2 s and 3 s could clearly make a difference, sometimes 3 s is better than 2 s (for GW150914, GW151012, GW170819), and other times it is the opposite (for GW170608, GW170818, GW170729).

The tests were also performed for the LIGO-Hanford detector, where the same model was applied. Once more, the time slice of 2 s or 3 s gave the best results. For the Virgo detector, the results are a bit more difficult to interpret. Indeed, it joined the two other detectors only during the second run. Therefore, there are fewer events available to perform the test. The only events for which the test can be performed are GW178014 and GW170818. For each of these events, the time slice giving the maximum value was 3 s.

In addition, to verify that these results were not due to the equal-mass model, the computation of the change in the SNR has also be done for GW170814 with the model where all the parameters are equal to the central values given in [7, 9]. The conclusions drawn previously remain the same. This shows that they do not depend on the model. Therefore, for the next tests, we shall focus on the equal-mass model unless otherwise indicated.

To sum up, it seems that the best way to have a higher SNR is to take a time slice of 3 s, which also gives the best result in the three detectors combined case. One further question arises: the change in the PSD can make a peak in SNR to be above or below the threshold for detection? Indeed, when the analysis is made, there is a value for the SNR above which the event is seen as interesting and kept for further studies. Under this threshold, the peak is rejected. Therefore, in the analysis done above, there could be a situation where the limit is set at 8, and the SNR obtained with a time slice for the PSD of 4 s is 7.9 and that for a time slice of 2 s is 8.1. In the first case, the peak is discarded whereas, in the second case, it is kept and can give rise to further studies and the potential discovery of a gravitational wave signal.

An additional point to keep in mind here is that the influence of the PSD time slice is studied for time series of 32 seconds. The duration of the series probably changes the optimal value used for the time slice taken in the PSD. Nevertheless, the computations done above show clearly that this time slice influences the shape of the PSD curve, as well as the signal-to-noise ratio found at the end. The information about the time interval and time slices used during the analysis done is not given (see for example [6] or [7]). The influence of such parameters also shows how difficult it could be to reproduce the exact results given by LOSC as all these parameters, which

can seem unimportant at the beginning, have an influence on the final result.

5.2   Influence of the window used in Welch's method

Until now, the window that has been used is the default Hann window. However, this window can be changed. In this section, different windows are tested in the computation of the power spectral density. The time slice used is fixed at four seconds, conformally to the recommendation of the LIGO tutorials. However, to change the window, a different function has to be used, the *pycbc.psd.estimate.welch(data, seg_len, seg_stride, window, avg_method)*. It enables us to estimate the PSD with Welch's method but gives more freedom in the number of parameters that can be adjusted. The first argument is the data, followed by the length of the samples and the separation between the consecutive samples. The *window* argument is the type of window that should be used (and which we shall change here). The *avg_method* is the method used to average the PSD of all the segments. Here, one uses the default, i.e. the median. However, other methods are available such as the mean or the median-mean [75].

The windows are generated according to the number of elements present in the sample, using the the *scipy* command: *scipy.signal.get_window(windows, Num_sam, fftbins)*. The first argument enables us to specify which window model should be used, *Num_sam* is the number of samples that are taken in the window and *fftbins* is a boolean operator that is set as true by default, leading the generation of a periodic window. The different windows tested here to compute the PSD are the ones that are possible by default in the scipy package. An overview, without details, is given here [76]:

1. *boxcar*: It is also called the Dirichlet window. It is a window that has the same amplitude for all samples (set at 1 here).

2. *triang*: The window has an amplitude which has a triangular shape.

3. *blackman*: It is defined by the mathematical expression:

$$W(n) = 0.42 - 0.5 \cos\left(\frac{2\pi n}{N}\right) + 0.08 \cos\left(\frac{4\pi n}{N}\right). \tag{5.1}$$

   It has the particularity to smooth the discontinuities at the start and the end of the sample (a function with this feature is called an apodization function) and is often used for smoothing the values it analyses.

4. *hamming*: It is defined as

$$W(n) = 0.54 - 0.46 \cos\left(\frac{2\pi n}{N-1}\right) \quad 0 \leq n \leq N-1 \tag{5.2}$$

   It is often used to smooth the values found.

5. *hann*: It is the basic function used in Welch's method implemented in PyCBC. It is defined in Eq.(2.20). It is also a smoothing function.

6. *bartlett*: It is defined as:

$$W(n) = \frac{2}{N-1}\left(\frac{N-1}{2} - \left|n - \frac{N-1}{2}\right|\right) \tag{5.3}$$

It looks a lot like a triangular window but is such that the extremities of the window are set to zero. It is an apodization function but has the particularity to reduce the crests that are found in the frequency domain.

7. *flattop*: It is a fifth-order cosine window where the different terms are adjusted to have the main lobe as flat as possible. These kinds of windows are often used to measure precisely the amplitude of the signal in the frequency domain.

8. *parzen*: It is a non-parametric method that returns the best window based on the sample. Therefore, it uses a boxcar window with a certain width, combined with a kernel, which is often a hypercube or a gaussian kernel. Here, the latter kernel is used if the noise is expected to be gaussian [77].

9. *bohman*: Such a window is a convolution of two half-duration cosine lobes for the frequency domain. In the time domain, it is the product of a triangular window and one cycle of a cosine function. There is a term added to set the first derivative of the function to zero [78].

10. *blackmanharris*: It gives a 4 term Blackman-Harris window. These windows are a generalization of the Hamming windows described above.

11. *nuttall*: It returns a variant of the Blackman-Harris window.

12. *barthann*: It gives a modified Bartlett-Hann window which has its main lobe at the origin and the side lobes with decaying amplitude. It is obtained by a combination of several Bartlett-Hann windows [79].

5.2.1 Modification of shape of the PSD depending on the window used in Welch's method

The list presented above is not exhaustive as there are a lot more window functions in the scientific literature. It gives an idea about how many different windows can be thought of and could eventually be tested for the gravitational waves. However, our analysis is restricted to the use of the ones that have been introduced. All these windows have different characteristics and can be used in various contexts, depending on the precision required or the information one wants to find in the signal. Therefore, one expects the PSD found with Welch's method for different windows to be different. As can be seen in Fig. 5.7, it is the case. However, the differences that can be found are not that important for most of the windows. It can be seen that the influence of the window seems to be the most present for the lower frequencies, where the curve is more or less smoothed from the one to the other.

In Fig. 5.7, all the windows are not represented. Nevertheless, the main characteristics and differences relative to the Hann window (which is the central figure) are present. First, by

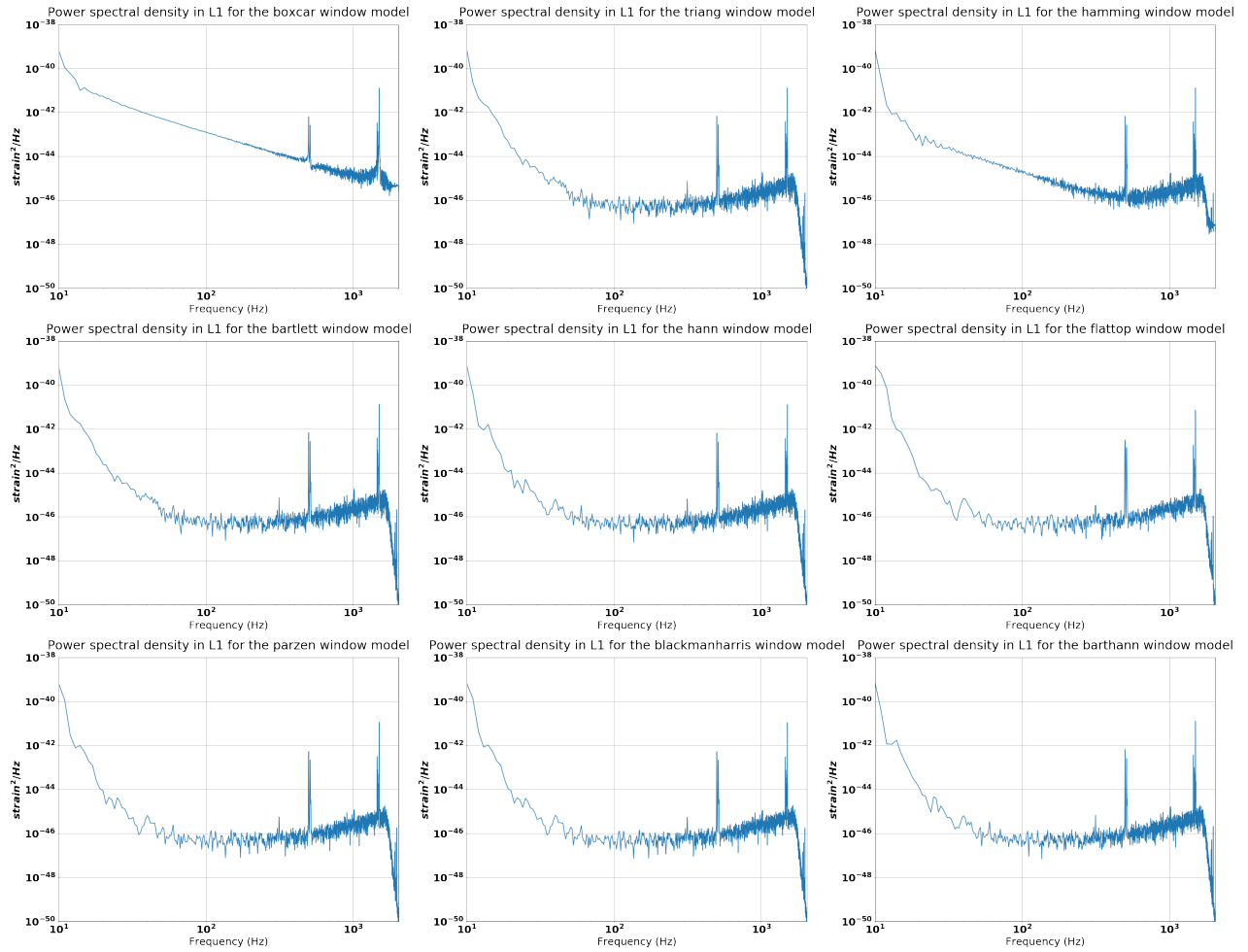Figure 5.7: PSD's found with Welch's method using nine different window functions. In most cases, the windows seem to behave in the same way for the highest frequencies. However, at smaller frequencies, the differences become more important. Still, some windows, such as the boxcar and hamming windows, behave much differently than the hann window used normally, which is at the center of the figure.

looking at the boxcar, one sees that the noise level is globally higher and that the plateau where the detector is considered as stable is not present. It is also the case for the hamming window, even if, at higher frequencies, it looks more like the default window. For all the other window models that are presented here, the PSD above 300 Hz seems to be the same, with the same frequencies peaking out and a relatively noisy curve. Note however that at lower frequencies, the curves are different for the various windows although the differences are not as large as that for the Hamming and boxcar windows. They consist in a number of fine details present. This region of the curve is very important as it represents the region in which one expects gravitational waves from a transient event. This can be seen, for example, in the Q-transform of the data for the L1 detector in Fig. 2.8, where one observes the signal ranging from 30 Hz to 500 Hz approximatively. Therefore, it does not seem to be a stretch to assume that, even if the differences look small, they will have some consequences on the data analysis later.

5.2.2 Modification of the signal-to-noise ratio depending on the window taken in order to compute the PSD

In this section, the PSD is computed using Welch's method with different types of windows. The SNR is then computed, and the chi-square statistic is calculated to reweigh the signal-to-noise ratio.

First, when the SNR is computed for the different windows, two major observations can be made: the peak corresponding to the event is changing in height from one window to the other and the height of the glitch peak before the event changes with the window that is used, in a way opposite to that of the event peak. So, when the event peak increases, the glitch peak tends to decrease. For some windows, such as the boxcar, the glitch peak has a higher amplitude than the peak associated with the gravitational wave event and would trigger further investigation before the event. On the other hand, for other windows such as the hann window, the glitch peak is less important than the event peak. So, the event would trigger further investigation before the glitch. However, in practice, the trigger is kept only when several detectors have a peak. So, the glitch would be discarded at the next step of the analysis.

Secondly, when the chi-square statistic is computed, it has the same behavior as in Section 3.2.4. The shape of the different curves is approximatively the same, but the value can be shifted up or down at the time of the event. Therefore, the chi-square is still close to one for the gaussian noise and increases as the template glides along the data. There is then a significant drop at the time of the event when the match is present. However, this drop is not the same for all the windows, and the value for the gaussian noise is not exactly one. For example, in the case of the flattop model, the fit is bad and the chi-square statistic is close to 2 far from the time of the event, where the expected value is around 1. In addition, it goes to values above 5 and drops to only around 1.5 at the time of the event. On the other hand, the value goes close to 1 for the hann window, or even for the boxcar window. Since the chi-square statistic should tell if the model waveform and the data are consistent, this change in value shows that the fitting is window-dependent.

Finally, it is possible to reweigh the SNR with the statistic calculated at the previous step and
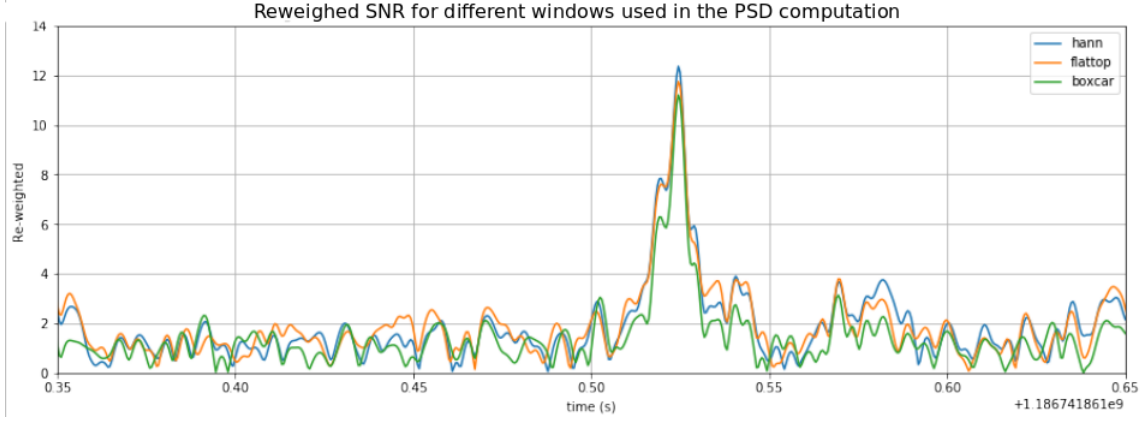
Figure 5.8: Reweighed SNR peak for the event when different windows are used in the computation of the power spectral density. We see that the value of the event drops from one window to the other. It is the highest for the Hann window and the lowest for the boxcar.

see how it evolves from one window to the other. The interest here is not the exact value of the peak that is found but the difference in height from one window to the other. A comparison between three different windows is made in Fig. 5.8. One sees that the value of the changes with the window in a significant manner. Indeed, between the lowest and the highest values, the difference is greater than 1. This again leads to the possibility to accept the trigger in one case and not in the other. One can also note that the maximum value found for the SNR is for the Hann window, which is the default in PyCBC, and the most suited in the case of gravitational waves. When looking at all the windows, others can provide a peak with a comparable value (barthann (which is based on the hann window) and bohman for example). However, these windows give rise to a more important value for the peak associated to the glitch in the SNR.

Chapter 6

Dependence of the results on the signal and noise characteristics

In this chapter, we look at the changes of the SNR from the characteristics of the signal and of the noise. More precisely, we look at the impact of a change in the length or amplitude of the signal, and in the noise characteristics and amplitude. This will help us understand not only the effect of non-gaussian noise but also the improvements that were needed to reach the current state of the art for the detectors. It also opens the perspectives for the coming years concerning the planned improvements.

6.1 Evolution of the SNR as a function of the fraction of the signal taken into account

When an analysis is made, it may happen that the full signal of the merger is not visible or that a glitch obscures a part of the signal. Moreover, in the case of neutron stars, it is interesting to detect the signal early to send an alert to the astronomers so that they can point their telescopes in the direction of the event to detect its electromagnetic counter-part live [80][1]. In addition, the detection of an event from only a fraction of the strain data would accelerate the search, only slightly for black holes and much more for neutron stars, as the signal of the latter has a duration of the order of 100 s v.s. 1 s for black holes. Therefore, it may be useful to know what fraction of the signal must be present to make the event detectable.

---

[1]For the case of the first neutron star merger GW170817, the electromagnetic counter-parts were discovered only later in the data [8].

6.1.1 The SNR of GW170814 as a function of the fraction of time taken into account.

In this section, we look at the value of the SNR for our reference event [7]. The operational mode used for this analysis can directly be applied to a neutron star merger (provided the template is adapted for such an event). This merger has bee described well in our previous chapters and the best-fit parameters are already known. Therefore, the subtraction of part of the signal from the data can be done with confidence.

Operating mode

After a subtraction of the gravitational wave from the data, the goal is to add it back piece by piece and see what fraction of it is needed for detection. Therefore, the first thing to do is to have a good model of the gravitational wave signal, which can then be used to subtract it from the data and keep only the noise. Therefore, we do a best-fit analysis of the event, as in Chapter 4. After this procedure, we obtain a template that represents at best our signal. However, we do not subtract it fully from the signal. Indeed, the amplitude of the template is non zero even more than 5 seconds away from the merger. But, it is of the order of 10^{-29}, which cannot be seen by the detectors. So, in our analysis, we will subtract only the *"visible"* signal, which corresponds to the part with a high enough strain amplitude to be detectable. This is done because we want to have an idea of the fraction of detectable signal that is needed for a detection to be possible. However, the full signal is much longer that that. So, we get rid of this part that cannot be used for detection anyway. The instruments, as can be seen in the PSD shown in Fig. 2.4, are sensitive to strains that have an amplitude above 10^{-23} to $10^{-22} \frac{strain}{\sqrt{Hz}}$ [81]. Therefore, in order to be conservative, we cut the waveform below $10^{-25} \frac{strain}{\sqrt{Hz}}$, which corresponds to a duration of 0.92 seconds. This will constitute what we consider to be the full signal in the rest of this section. This is very conservative, as we take 2 orders of magnitudes safety. After that, this visible signal is split into 100 equal parts. Those are then added one by one to the noise. Each time a fraction of the signal is added, the matched filtering technique is used. The template that we try to match here is the same as before and is built with the IMRPhenomD model with parameters equal to the central values given in [7, 9]. For each fraction of the signal, we retain the value of the SNR as well as the time at which it is found.

The addition of the fractions of the total signal was done once from left to right in time, i.e. from the inspiral to the ring-down and once from right to left, i.e. from the ring-down to the inspiral. Although the first scenario seems more sensible as it corresponds to the normal income of the signal in the detector for a low-latency search, the comparison of both cases can also show which part of the signal contains the most important information about the event and makes it the most recognizable. Moreover, between runs, the full data set is analyzed again to see if the data do not contain any event that has been missed. This data can be analyzed from right to left as well and, if we can ensure that only a given part of the signal is enough to determine its presence, the search could be performed only for that part. In that case, because fewer sample points are concerned, the analysis would be faster. This reasoning is even more important for neutron stars, where the data analysis takes much longer due to the total duration
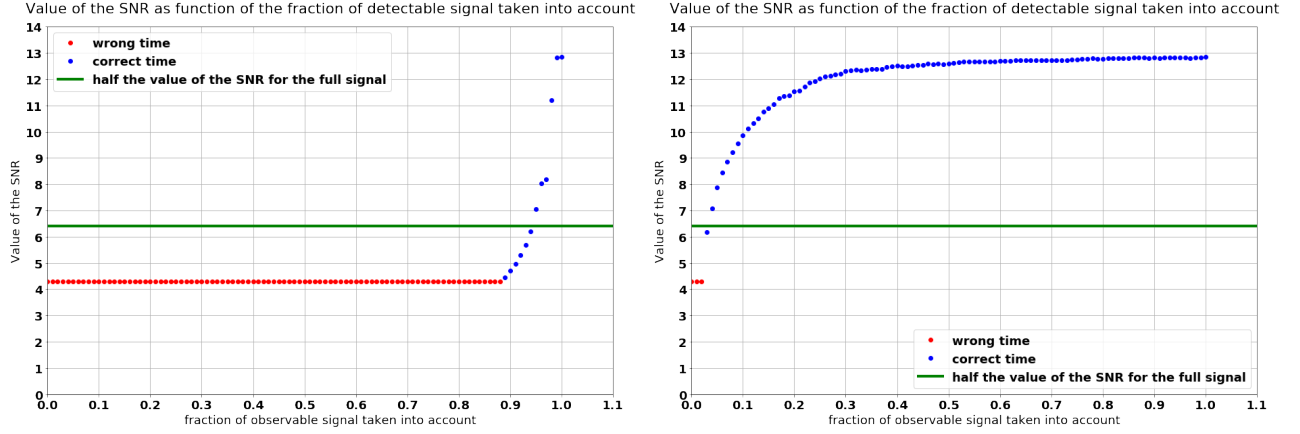
Figure 6.1: Left, the SNR as a function of the fraction of the signal present, added from left to right. Right, the SNR as a function of the signal present, added from right to left.

of the signal [8].

Results and discussion

The results are shown in Fig. 6.1. In the case where the fractions are added from left to right, we see that, at the start, the peak that is found is due to noise. Indeed, it has not a significant value and is not present at the correct time (red dots in Fig. 6.1). When looking if the peak of the event is at the correct time, we accept an error of 0.01 s because the presence of only the starting part of the signal leads to a slight time shift of the peak in the SNR, even if it is already due to the event. Once a significant fraction of the event is present (90%), the signal becomes detectable. This shows that the full detectable signal is not needed to find the event but a great deal of it is needed to detect it. The long period without detection at the start could be due to the conservative estimate of the detectable part of the signal that we have made. Indeed, for the first part of Fig. 6.1, the signal assumed to be detectable is fainter than the noise. So, the 90% fraction found here is the worst-case fraction. A study of the difference in the minimal fraction of the event needed to be detected as a function of the lowest limit of detectability would help to have a better idea of what is going on. Moreover, in this analysis, we used a cut-off frequency of 20Hz, which also removes a part of the inspiral signal. This parameter influence should also be tested to see if we could detect the event earlier by decreasing (or even dropping) this limit. When the analysis is done from right to left, the SNR is found as soon as 4% of the signal is included in the search. When 9% is included, the signal is already at the exact timing of the event. So, the detection relies on the final parts of the signal, with most of the information contained in the merger and the ring-down and less in the inspiral. One can argue that the search for a gravitational wave event can be accelerated by searching only for the merger and the ring down. The time needed for the matching in the analysis is then shorter, and would enable us to go faster.

It is then possible to look at the parts of the signal, in the time domain, that correspond to the event in both cases. This is shown in Fig. 6.2, where the original signal, as well as the
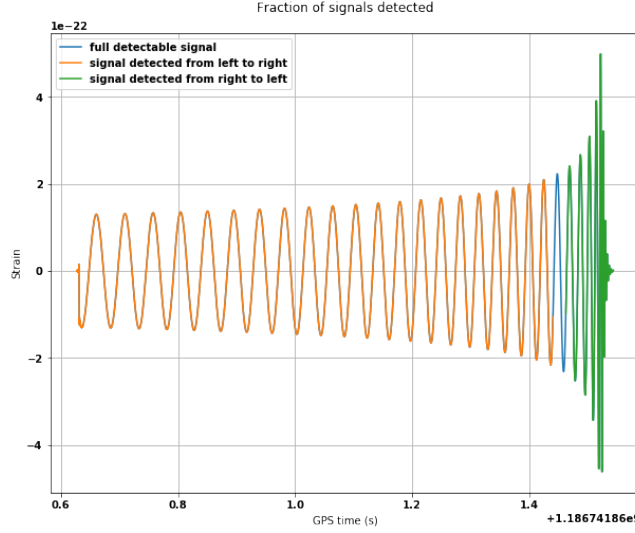
Figure 6.2: Fractions of the signal that lead to a detection when the analysis is made from left to right and right to left. We see that the two parts needed to find the signal in the two analyses do not overlap.

fractions of signal needed for detection from right to left and from left to right are represented. We see that for the case where 5% of the signal is needed, the corresponding part of the event is made of the merger and the ring-down, with a very small part of inspiral before. The other case corresponds to a much longer part of the signa made only of inspiral. Note there is a gap between the two parts, where the signal has never been included to give the detection. This shows that there is no need to go through the full inpiral to find the merger. So, there can be a time gap between the moment an event is detected and the moment its merger occurs. If this scales up to the case of neutron stars, it would mean that early detection is possible. Sending an alert for a live detection is possible provided the gap is big enough. However, note also that the SNR has a value of 9.5 only (for a single detector), which is not as significant as for the full event.

This study is preliminary. It will be interesting to look at these questions for the future detectors, such as the Einstein Telescope, where the signal will be longer and the possibility to use only a part of it even more interesting [10, 82, 83].

6.2 Evolution of the SNR as a function of the noise amplitude and characteristics

6.2.1 Signal swamped in gaussian white noise

When the matched filtering technique has been explained in Chapter 1, we made the assumption that the noise is gaussian and second-order stationary. However, these hypotheses are not true
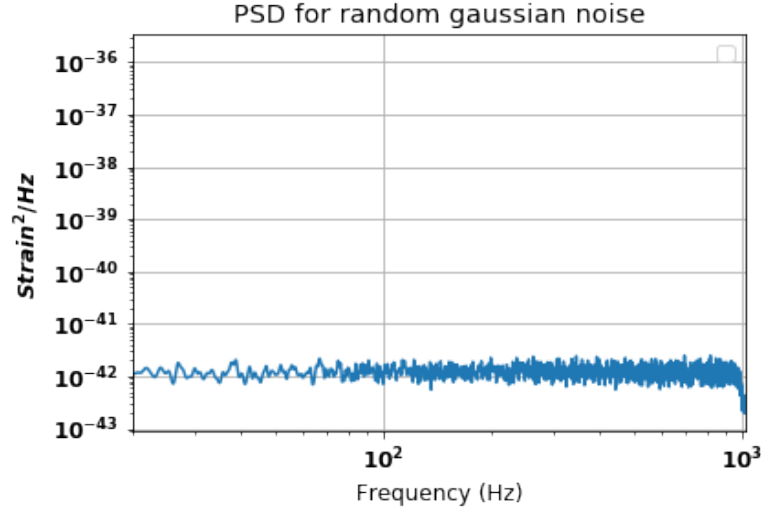
Figure 6.3: PSD of white gaussian noise centered at zero and with a standard deviation of 10^{-21}. It is flat for all the frequencies. The higher density at higher frequencies come from Welch's method.

for real detectors. As has been mentioned earlier, the detectors are subject to glitches and the noise sources such as the gravitational gradient, earthquakes, etc. are not stationary. Moreover, there are also poissonian noises that are present, which, by definition are not gaussian [84]. This section will look at the performance of the analysis tools on white noise and at the change of the SNR by this noise.

To do that, we have to make a signal. The gravitational wave signal is taken as the GW170814 event, built with the best-fit parameters found earlier. We then need to build gaussian noise, via a random gaussian generator (*scypi.stats.norm* from the *scipy.stats* Python package [85]). As for the real strain, the distribution is centered around zero. The standard deviation of the distribution is first set at 10^{-21}, which is higher than for the real noise for which the standard deviation is 10 too 100 times lower. The PSD of gaussian noise can be seen in Fig. 6.3. It can be compared with the PSD of the detector shown in Fig. 2.4. We see that there is a plateau for the full frequency range and that there are no peaks in the data as is the case for the real PSD (such as the 60 Hz line for example). Moreover, there is no increase in the global noise curve below 100 Hz as it is the case for the real PSD.

When the gravitational wave signal is injected in this noise, the SNR has a value of 13.5, which is a bit higher than for the real noise [7]. However, the typical amplitude of the noise here is 10^{-21}, whereas it is more of the order of 10^{-23} in the LIGO detectors at the time of detection. So, we see that the analysis works better in the case of gaussian noise. This follows from the hypotheses that were made during the derivation of the matched filtering technique, and opens the possibility to find a better matching algorithm in real noise.

Another interesting feature is the evolution of the SNR as a function of the amplitude of the white noise. The results of this change can be seen in Fig. 6.4. To analyze this, it is important to keep in mind that the maximal amplitude of the gravitational wave signal is of the order
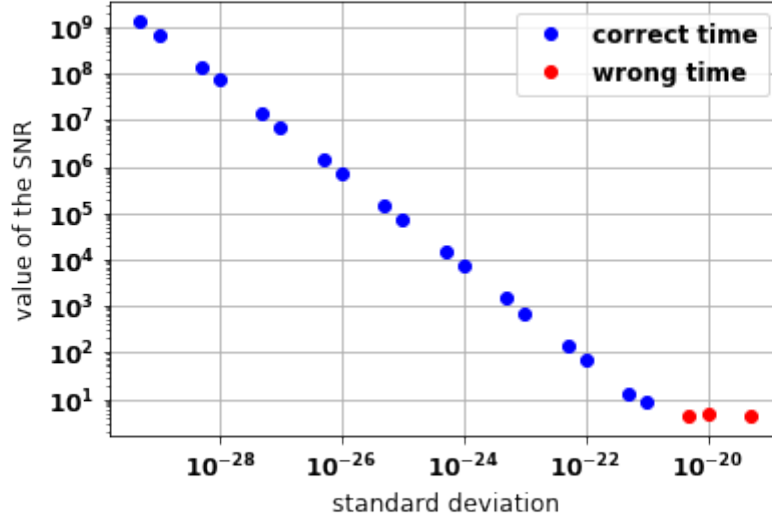
Figure 6.4: Evolution of the SNR as a function of the standard deviation of the gaussian noise.

of 5×10^{-23}, the same order as the noise [7]. For gaussian noise, the event can be found as soon as the noise has a standard deviation of 10^{-21}, which is approximatively 2 orders of magnitudes higher than the signal itself. The value of the SNR that is found only increases as the amplitude of the noise decreases. When the standard deviation of the noise is of the same order of magnitude as that of the signal (10^{-23}), the SNR has already a value of about 1000. We see that the matched filtering technique is far more efficient for gaussian noise than for the real noise. Although the noise sources are looked for and eliminated when possible, some sources cannot be avoided (such as the shot noise, the gravitational gradient drift, the earthquakes, ...). Therefore, there is no hope to find such high values for the SNR. However, the coming improvements of the detectors, as well as some new projects can lead to a decrease in the noise. This could already lead to an increase in the SNR of the current events, as well as the detection of other sources [74].

We see that the SNR is well fitted by a power law, where

$$SNR \simeq \frac{10^{20}}{\sigma}, \text{ if } \frac{10^{20}}{\sigma} > 1. \tag{6.1}$$

This behavior can be understood by the properties of white noise. If we have a gaussian noise and if the points are independently distributed, then the denominator of the signal-to-noise ratio in Eq. (3.1), which is the square-root of the autocorrelation function of the noise. This is equal to the standard deviation of the noise [68]. Therefore, it can be taken out of the integral and we divide the convolution of the template and the signal by a constant factor, which decreases with the standard deviation of the noise. Indeed, the result of the integral is the same, as the result of the matched filtering does not depend on the amplitude of the signal in the data [27]. So, this behavior explains how the SNR "explodes" as the value of the standard deviation decreases. However, as we have mentioned earlier, there is no way to transform the noise in the detectors into gaussian noise [74].

6.2.2 Evolution of the SNR as a function of the amplitude of the noise present in the detectors and as a function of the amplitude of the signal

For the existing detectors, such as LIGO, Virgo, and KAGRA, there are plans to enhance the sensitivity in future runs. It could lead to a gain of nearly a factor 10 in the sensitivity for the frequency domain ranging from 100 to 150 Hz [86]. There is another ground-based project that aims to do even better: the Einstein telescope[2]. It should go down to sensitivities of the order of 10^{-25}, which is more than a factor 10 better than the best we could do with current detectors. The detector should also be able to detect the signal in a broader frequency range, starting down at 3 Hz and going up to the end of the signal with the merger, leading to much longer signals (up to 20 hr. for neutron stars mergers). This would also increase the volume of the Universe that can be probed with the instrument as well as the detection rate [87]. Some detailed studies of the mass ranges, the detection rate, and the distance at which the objects could be detected have been made for the enhanced versions of LIGO and Virgo, as well as for the Einstein telescope (see [74, 82, 83, 87] for example). Here, we only look at the evolution of the SNR as a function of the amplitude of the noise, as well as a function of the amplitude of the signal, which is directly related to the distance at which the merger occurs.

For this purpose, we look for the GW170814 event, build with the best-fit parameters in a noise that is similar to the one present in the detector, except that there are no glitches. This noise can be build based on the PSD of the true signal detected for the event. So, we first build the power spectral density based on the true black hole merger signal, as has been done in Section 2.4 Then, we can retrieve a noise frequency series based on the PSD by the use of the PyCBC command *pycbc.noise.gaussian.frequency_noise_from_psd(PSD, seed)*. This function takes the PSD and a seed value as arguments. The latter should be fixed if one wants to return the same noise series when the computation is done several times. This function returns a colored noise frequency series, which has the same length as the PSD but also the same frequency step. The coloration of the noise is done by using the PSD itself to generate the frequency sample. Therefore, each frequency point is sampled from a normal distribution with a standard deviation calculated from the PSD at that frequency [88]. So, the final generated noise is not white anymore. First, to characterize the noise, we can build its PSD. This gives Fig. 6.5. The PSD that is obtained looks like the PSD we started with, except that there is a deviation for the lowest frequencies. Indeed, around 10-20 Hz, the PSD has a value of $10^{-44} \frac{strain^2}{Hz}$ for the noise build from the PSD. On the other hand, the original PSD (see for example Fig. 2.4) starts at a higher value of $10^{-41} \frac{strain^2}{Hz}$ and drops in a steeper way towards the plateau. The peaks present throughout the plateau are also different, some are present in both cases but with different values and others are completely removed or added. The frequencies at which these peaks are present, as well as their value, depend strongly on the seed that is chosen.

A first manipulation analyzes the data made of the addition of the generated noise and the best-fit template. This gives an SNR of 12.6, slightly lower than the previous one, but not significantly. The difference is probably due to the characteristics of the noise that have fluctuated. So, we can proceed to the analysis of the SNR as a function of the amplitude of the

---

[2]For more information about the Einstein Telescope project, see its web-page: `http://www.et-gw.eu/`
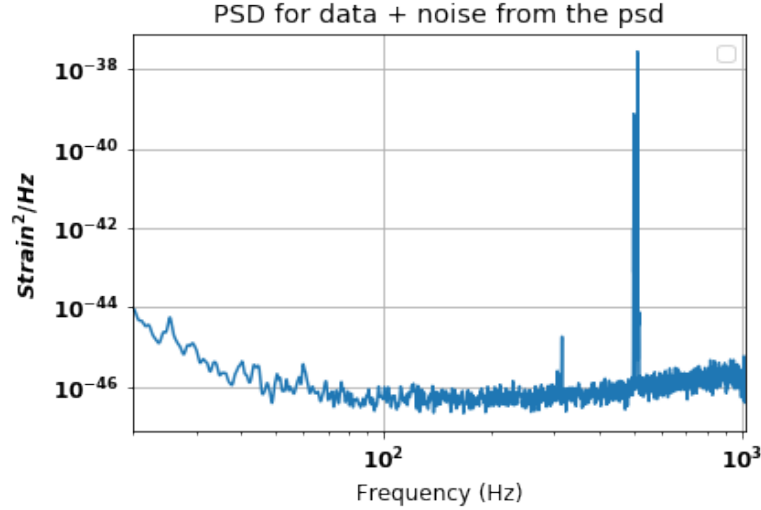
Figure 6.5: PSD built from the noise generated from the true PSD after the signal has been reinjected in the noise. This gives the same situation as for the other figures, where we make a PSD with a signal present.

detector noise in which the signal is swamped. We simply multiply the amplitude of the noise by a factor before the signal is reinjected. The multiplicative factor ranges from 10^{-4} to 100, the smaller values giving an idea of where we could go with the future detectors and the higher showing how important it has been, historically, to decrease the noise levels in the detectors to lead to the first detections.

If A is the multiplicative factor and B the multiplicative factor for the amplitude of the event (1 in the usual case, 0.1 when we divide by 10, etc.), we find the the SNR follows the law

$$SNR \simeq \frac{10B}{A}, \text{ if } \frac{10B}{A} > 1. \tag{6.2}$$

The result of this analysis can be seen in the left plot of Fig. 6.6, which shows the value of the SNR as a function of the multiplicative factor that is applied. We see that a noise ten times higher does not enable to detect the signal of this event, which explains why only a very loud signal could lead to the first detection (GW150914 [6]) and how the enhancement from the second to the third observation run could lead to an increase of the detection rate (11 events were observed in total during the O1 and O2 runs [9] and already more than 50 can be found on the public alert page *GraceDB* at the time of writing [89]). We also see that, in the case of a reduction by a factor ten of the noise in the detectors, we can have an SNR that goes above 100, making it very easy to spot the gravitational wave in the analysis. In addition, this means that events that have an SNR below the noise for the moment, mostly because they are too far, would become visible by a decrease of the noise. To check that, we redo the analysis with a changing amplitude of the noise but with a signal reinjected that is divided by 10 and by 100. This is equivalent to change the distance of the event and put it 10 or 100 times further, as the amplitude of the signal goes as $\frac{1}{distance}$ [33]. When this is done, we can observe that a division by 10 of the noise amplitude enables us to retrieve an SNR above 10 for the signal that comes from an event 10 times further. Similarly, the division of the noise amplitude by a factor
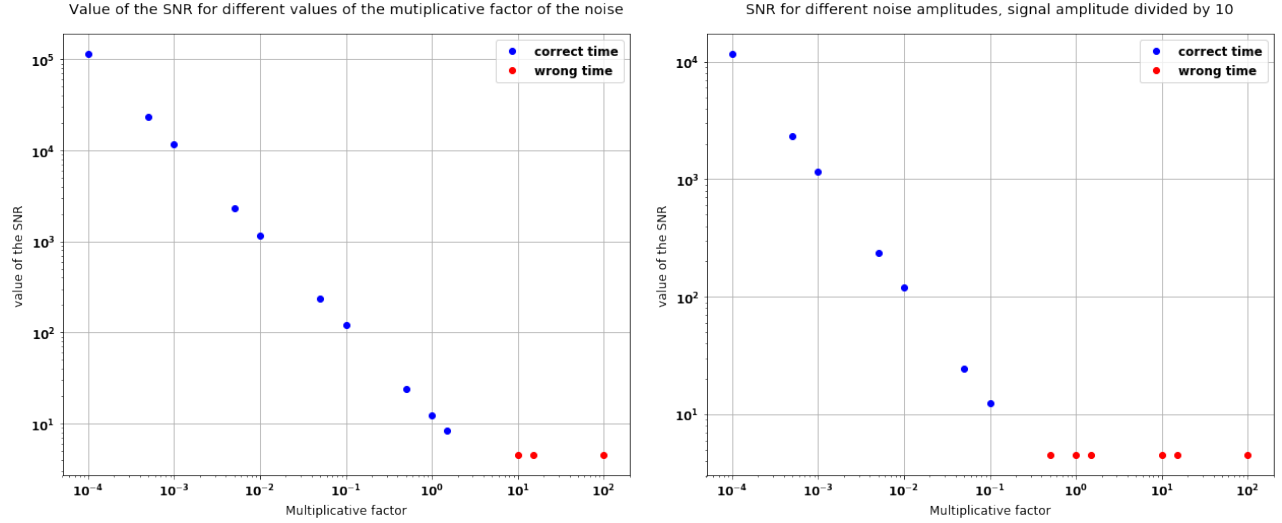
Figure 6.6: Left, the variation of the SNR value for the GW170814 event as a function of the noise amplitude. Right, the variation of the SNR for the GW170814 event as a function of the noise amplitude, when the event amplitude is divided by 10.

100 makes it possible to find the signal 100 times further (the case of the amplitude divided by ten can be seen in the right plot of Fig. 6.6). So, this means that the improvement done on the LIGO and Virgo detectors will enable us to increase the number of events that are seen, as fainter gravitational wave signals can be detected. This will be even truer in the case of the Einstein telescope, where the decrease in noise will be even more important. As a consequence, the volume of space that can be probed is multiplied by 1000 (as the distance is by a factor 10). Therefore, we can expect 1000× more events to be detected [82]. In terms of redshifts, it means that we can expect to observe redshifts up to 10 for the Einstein telescope, instead of the 0.1 to 1 redshifts currently observed in the LIGO-Virgo detectors [74, 82]. This also means that we will need to find ways to accelerate the searches of the events, as their frequency and their durations will increase. The use of smaller parts of the signal for detection could be part of the solution. Another very popular and widely studied alternative is the use of artificial intelligence for the search (on the full signal or part of it). Indeed, in this case, once the neural network has been trained, it can directly be used on the data to find the signal much faster than what is currently allowed by matched filtering (for more information see, for example, [90, 91]).

Chapter 7

Neutron stars overview

7.1 Interest of these objects and difference with black holes

Up to now, we have looked at the PyCBC tools, how they work and at the impact of some parameters, and at the variations from a change in the signal or the noise. We have focused of the GW170814 event, which is a black hole coalescence. However, as has been mentioned, there exists other types of events that can be detected with the matched filtering technique: binary neutron star mergers and black-hole neutron star mergers[1] [80]. These events are also very interesting and open new horizons in different fields. Indeed, the first binary neutron star event, GW170817 [8], has confirmed the prediction that such mergers could be at the origin of short-duration-gamma-ray bursts [92]. Indeed, the *Fermi* satellite detected such a burst in a time that is consistent with the detection of the gravitational wave (the signal in the gamma domain was found 1.7 s after the signal in the gravitational wave domain). Moreover, the detection was also made in other wavelengths, such as in X-rays (9 days later), in the optical and infrared (11 h later) and in the radio domain (16 days later) [93]. These multiple counterparts enabled the LIGO-Virgo collaboration to find more accurately the position of the event and to confirm that it was a neutron star merger. This event was reported to lead to a kilo-nova event, situated in NGC 4993, at a distance of 40^{+7}_{-15} Mpc [9, 8, 93, 94]. The possibility to link the gravitational wave signal to its electromagnetic counterpart gives access to the study of the Hubble constant: the amplitude of the gravitational waveform gives direct access to the luminosity distance of the source and the electromagnetic counterpart gives the redshift (at the time of detection, they found $H_0 = 70^{+12}_{-8} \frac{\text{km}}{\text{s Mpc}}$) [8]. The study of the time taken by the photons to reach the Earth was also a way to test general relativity, more precisely the Shapiro effect[2], the equivalence principle and Lorentz invariance [8]. In addition to the tests of general relativity, neutron star mergers could also provide a better understanding of the *r-process*, which is how part of the heavy elements (heavier than iron) are supposed to be created in spatial objects [96, 92, 93]. Another extra property that could be studied with this kind of events is the equation of state

---

[1]Other signals, such as continuous signals or signals coming from yet unknown objects are also looked for but this is done with other techniques and is not successful so far.

[2]For more explanations about the Shapiro effect, see [95].

of the neutron stars [92]. However, during the O1 and O2 runs, GW170817 is the only neutron star merger that has been reported. With only one detection, it is a bit difficult to make strong conclusions about these things but we see that their observations could lead to much new knowledge.

From the point of view of the analysis, there are some differences that exist, even if the tools that are described earlier in this work remains valid. First, the lower masses of the objects lead to a longer inspiral phase, which means that the coalescence is visible much earlier in time and for a longer period before the merger happens. Indeed, from a first order development, the time during which the event is detectable before the chirp is given by [37]:

$$ t_c = \frac{5}{512} \frac{M}{\mu} \left(\frac{GM}{c^3} \right)^{-\frac{5}{3}} \left(\pi f_0 \right)^{-\frac{8}{3}}, \tag{7.1} $$

where $M = m_1 + m_2$, the sum of the masses of the components, $\mu = \frac{m_1 m_2}{m_1 + m_2}$ is the reduced mass and f_0 is the lowest frequency that the detector is sensitive to. This shows clearly that the time is very different for two neutron stars (140 seconds if the two neutron stars have a mass of one solar mass) and for black holes, where it goes down under a second. This difference in length can be seen in Fig. 7.1.
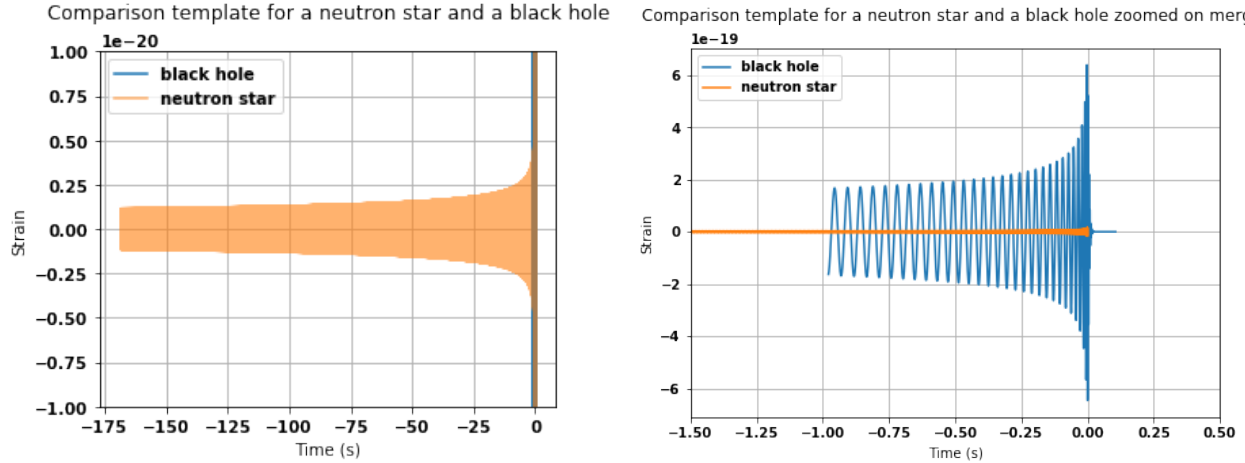
Figure 7.1: Waveforms build for a binary neutron star merger with masses equal to the central value of the masses for the GW170817 event given in [9] and for a binary black hole merger with masses equal to the central masses given for the GW170814 event in [7]. The waveforms are placed in order to have their merger happening at the same time. Both events start when their frequency is above 20 Hz. Left, we see a long-time view, with the neutron star signal having a larger amplitude early on. Right, we see a view zoomed on the merger time for the event, where the black hole signal becomes much larger.

Another difference between both objects is the amplitude of the signal. The neutron star will present a wider signal than the black holes earlier in time. However, once we are closer to the merger and that the signal becomes detectable, the black hole signal is much broader. This explains why neutron star took more time to be discovered and why we think that we will

observe more of them as the strain sensitivity of the detectors gets better [74, 92]. Indeed, here, the amplitude of the signal is one order of magnitude higher for the black holes at the time of the merger, making it easier to spot for the detector (this relation depends on the relative distance of the two events). This difference can also be seen in Fig. 7.1. The first-order development of two rigid bodies rotating around each other gives an evolution of the amplitude of the waveform over time as [37]:

$$A(t) = \frac{\pi G m_c}{c^4 r} \left(\frac{(t - t_c)c^3}{5 G m_c} \right)^{-\frac{1}{4}}, \tag{7.2}$$

where $m_c = \frac{(m_1 m_2)^{\frac{3}{5}}}{(m_1 + m_2)^{\frac{1}{5}}}$ is called the chirp mass. It is the parameter that appears at the first order in $\frac{v}{c}$ and is, therefore, the best constrained one when the gravitational wave is observed. As we see, this chirp mass appears at the numerator and will increase as the masses of the components increase, leading to larger amplitudes for systems with heavier objects.

Another difference between neutron star and black holes is the tidal effect. Indeed, contrarily to black holes that are almost rigid (at first order[3]), the neutron stars undergo tidal deformation during their merger (either for binary neutron stars merger or a neutron - black hole merger) [98, 99]. These tidal deformation effects are taken into account in the templates that are used for the search, as they are important for the full evolution of the orbit [8]. This tidal effects, once detected, would enable us to understand much better the equation of state of neutron stars. However, at the moment, the sensitivities of the detectors are not sufficient to study it. It will become more relevant with the next generations of detectors [92]. This leads to the introduction of extra parameters, which are the tidal deformability of the neutrons stars and the combined dimensionless deformability [8].

At the end, in addition to the combination with the electromagnetic counterpart, there are more effects that should be taken into account for the neutron stars, leading to more physics that could be probed. However, from a pure data analysis point of view, the tools remain the same when the matched filtering is done. Nevertheless, the differences in the shape of the signal lead to some differences when we try to analyse the data. First, because the duration of the signal is longer, all the functions take more time to compute. Another consequence of the length is that a small difference in the template can make a huge difference at the end, making the exact subtraction of the signal in the time domain difficult. Indeed, a small difference leads to a slight shift between the two waveforms. Even if this is not very important at the start, it becomes more important as time goes on. This means that in order to fit the parameters, we need to know all of them with high accuracy. Moreover, this fit becomes too CPU-extensive to be done here. For the GW170817 event, when it was detected, the study was done using bayesian inference and combining two million different templates at different times to cover the full signal and retrieve the parameters [8]. Despite this difficulty in the time domain, an approximated method in the frequency domain will be used here. It gives satisfactory results for a basic analysis.

---

[3]the tidal effects of black holes are very weak but could be probed later, when a higher accuracy is reached in the detectors and the models [97].

7.2 Matched filtering for the GW170817 event

In this section, we look at the matched-filtering technique applied to a neutron star merger. It is done with fewer details than what has been done for the GW170814 event. Nevertheless, the main differences are explained.

The data used here is not one of the strains that are contained in the PyCBC catalogue by default. Indeed, these are made of 32 seconds of data, which is too short for a neutron star signal to be seen and analyzed. Instead, we use the bulk data files that are provided by LIGO[4]. These gwf files contain the data already cleaned from the major glitches. Therefore, although it was present for the treatment in [8], here the big glitch in the LIGO-Livingston detector, just before the merger, is not present anymore[5]. This file can then be read with the *pycbc.frame.read_frame(location, channel, start_time, end_time, duration, check_integrity)*, where the first argument is the file name, the second the channel that we read (the corresponding detector). The three next correspond to times and duration of the signal and the last verifies the internal integrity of the frame file [100]. For our analysis, inspired from the example that can be found on the PyCBC site[6], we take a start time 224 seconds prior to the time of the merger and an end time 32 seconds after the time of the merger given in PyCBC (found with *merger.time*).

In order to whiten the data and do the matched filtering, we need the PSD. This is built exactly as in Section 2.4 for the analysis of the GW170814 event. As has been said, the PSD is a way to characterize the noise that is present in the detector. Therefore, it does not depend on the signal that is present [50].

Before doing the matched filtering, we can look at the Q-transform of the data. This can be seen in Fig. 7.2, where we show the signal for the L1 interferometer. We can see that the signal has a longer duration than for black holes, as the tail in the lower frequencies is longer. After that, when the merger happens, we see that the strength of the signal is less important. Those two observations are coherent with the particularities explained in the first section of this chapter. It is important to note that it is not because the signal is less strong during the merger that it means that the SNR that is found is lower. Indeed, if we compare the SNR that is found for GW170814 and GW170817 for the two American detectors, we have the values 7.3 and 18.8 resp. in LIGO-Hanford and 13.7 and 26.4 resp. in LIGO-Livingston [7, 8].

The next step is to use the matched filtering of a template on the data in order to determine the masses. Therefore, we explore the mass space and see which values give the maximum network SNR. The latter is defined as [101]:

$$NetSNR = \sqrt{\sum_{detectors} SNR_i^2},$$

(7.3)

where the sum runs over the detectors used for the detection and SNR_i is the signal-to-noise

---

[4]They can be found at the address `https://dcc.ligo.org/public/`

[5]In order to see how the glitch can be removed, see [8].

[6]see: `https://github.com/gwastro/PyCBC-Tutorials/blob/master/examples/gw170817_mass_estimate.ipynb`
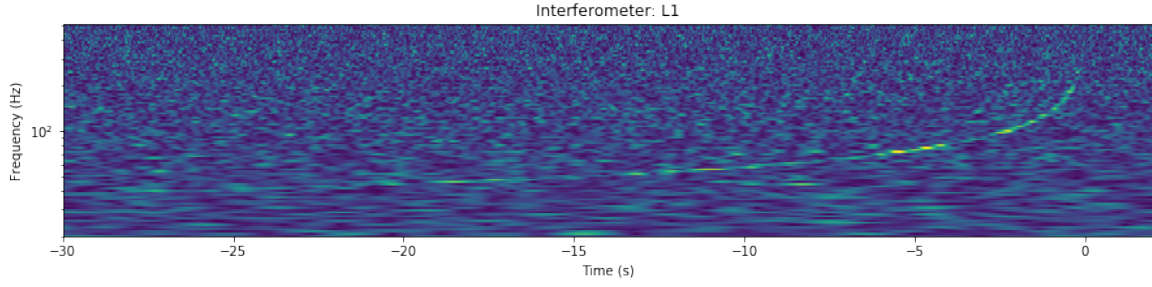
Figure 7.2: Q-transform of the GW170817 event in the LIGO-Livingston detector, zoomed on the event with 32 seconds prior the merger and 2 seconds after it. The signal has a longer duration than that of a black-hole merger. It is also less sharp, showing that there is less power present.

ratio in one specific detector.

We compute the value of this network SNR for all the masses possible and keep track of the highest value. In our case, we have explored values for both masses from 1 to 2 $M_\odot$ by steps of 0.01. We also neglect the value of the spins, which are set to zero. We are able to find a maximum value of the network SNR of 32.8 with a SNR of 26.9 in the L1 detector and one of 18.7 in the H1 detector. We can compare this with the values stated in the GWTC1 catalog of detected gravitational waves for the O1 and O2 runs. The value given for the network SNR is 33 [9]. For the individual detectors, the detection paper [8] gives values of 26.4, 18.8 and 2.0 in the L1, H1 and V1 detectors respectively. We see that they accounted for the European detector in the SNR, although they did not use it for the characterization or the sky localization of the source. Indeed, the binary neutron star horizon of the detector was less important at the time and the event was not well situated with respect to the plane of the detector [8]. This horizon is the distance at which the detector can observe the merger of two neutron star happening in a plane perpendicular to that of the detector [102]. We see that, even if the spins have not been adjusted here, the SNR is relatively high. In this scenario, the matched filtering is also done with the *macthed_filter()* command explained in Section 3.2. However, in this case, the series that have been passed to the function are frequency series. and the data was first transformed by the *TimeSeries.to_frequencyseries()* function of PyCBC, which returns the Fourier transform of the data [103]. As has been said in the previous section, when working in the time domain, a slight difference in the values of the parameters leads to an increasing difference between the signals as time goes on, making a slight mismatch grow larger over time. This is avoided in the frequency domain.

The template model that is used here in order to do the matched filtering is the *TaylorF2* model. This is a template that is built from the post-newtonian approximations. It has the advantage to be fast but can have some inaccuracies for the highest frequencies, where the approximations used in the post-Newtonian approach break down [62].

A way to check if this approach is coherent is to subtract the template built from the masses found from the Fourier transform of the data and then build the Q-transform of the difference (from the inverse Fourier transform of the difference). When this is done, the signal disappears

from the data, as the elongated banana shape is not seen any more. This proves that the signal is well subtracted.

We could try to have a better fitting of the parameters via a best fit method. However, this approach is too heavy for a single computer. Another aspect that could be explored is the determination of the values of the spins. However, this would require a lot of time and was not done here.

7.3   Possibility to detect the merger early on

In Section 6.1 we looked at the evolution of the signal-to-noise ratio in a binary black hole coalescence as a function of the fraction of the signal taken into account. This determined if it was possible to detect the signal based on only a fraction of it (a part of the inspiral or only the merger and ring-down). However, no electromagnetic counterpart is expected in such a case (although some claim that such counterparts could have been detected in the gamma ray domain (see [104] for example)). Moreover, due to the shortness of the detectable signal, it could only help to accelerate the search. Here, we look at the possibility to detect a neutron star merger in advance with the matched filtering technique. In such a case, an electromagnetic counterpart is expected and has been detected for the GW170817 event [8, 92, 93, 96, 98]. However, the electromagnetic counterparts are found afterwards, with a backward search. Hence, once the gravitational wave event is detected, we look for the counterpart in the data at times that are consistent with the event. If it was possible to detect the event enough in advance based on its inspiral, one could send an alert to the astronomers so that they could look at the event happening live. This would trigger a multi-messenger network of detectors that would track the neutron-star-merger evolution in its last phase, giving extra information about these objects.

7.3.1   Method of search

In order to correspond to a real detecting scenario and for computational reasons, the analysis is done slightly differently than in the case of the black hole merger. Due to the length of the signal and the difficulty to have a precise waveform, we cannot represent it fully and subtract it well from the data. Instead, we look at the raw data in windows of 256 seconds, with starting times ranging from 356 seconds prior to the reported time of the GW170817 event to 50 seconds prior to the event in the case of the LIGO-Livingston detector. In order to see if the analysis was consistent, it was also done for the LIGO-Hanford detector, with starting times ranging from 356 to 206 seconds prior to the event. The difference between both is due to the data quality. Indeed, the H1 data is noisier after the event and leads to the presence of artefacts once the ending times are situated too late after the merger. Therefore, we look less far in the future. This does not lead to a problem as we want to detect the event in advance. We try to detect a signal, with the matched filtering technique and template adapted for the event, for each time window, shifting the start and end times by 1 second before redoing the analysis.

Two scenarios have been tested: one where only the data window is considered and one where

we add a 90-second time padding of detector noise after the window. Indeed, when the matched filtering technique is performed with the *matched_filter(...)* function of PyCBC, returns a time series with a complex SNR for each time [64]. However, the times returned are those provided to the function. If we do not add the padding, there can be an increase in the SNR meaning a possible event but the time at which the merger will happen is outside of the window. In the case where some detector noise is added afterwards, we have the possibility to look slightly ahead in time (up to 90 seconds here), which means that when the signal is matched, the correct time may be found.

In the latter case a problem can arise. The addition of noise is made by merging two time series. If the characteristics of the glued signals are too different, it could lead to the same type of signatures as glitches in the detector. Moreover, as we consider data entering the detector over time, we do not have the possibility to use future data that would have been cleaned of the signal. Two approaches were considered here and their results can be seen in Fig. 7.3. In the first case, we added colored gaussian noise built from the PSD of the time window that is considered. Matched filtering technique has been designed for such noise so that, when only a part of the signal is present, the gaussianity of the rest of the data would facilitate the analysis and give a more precise time [27]. Remember that the advantages of such noise have been shown in Section 6.2. However, the real noise has other components [40, 105, 106], so that the sample points that we add are rather artificial and quite different from those that we had before. This leads to glitches with over-densities in the frequency domain. Therefore, this was not used for this analysis because it would probably lead to artefacts. The other approach that we ended up using was to paste 90 seconds of data from earlier times in detectors, where no signal was found: we select 90 seconds of data ranging from 1187007040 to 1187007130 seconds (in GPS time). When a matched filtering analysis is done on these segments (for black holes or neutron stars) for different masses, no SNR above 5.6 is found. Moreover, if we look at their Q-transforms, no typical banana-shaped signature is present. This window is then simply pasted behind the considered window. Because this series is made of random noise characteristic of the detector, when it is added, there is no big glitch as was the case for the gaussian noise. If we look closely at the Q-tranform of the window containing the event with this noise added, we can see that there is a very small over-density at the highest frequencies. However, it is above the values that enter the signal and does not influence the analysis.

We also considered two different types of templates to find the signal in early segments and compared this partials SNR with that of the full signal. The first template is built from the *IMRPhenomD_NRTidal* model, which is a phenomenological model built by hybridizing EOB waveforms for the inspiral with numerical relativity waveforms for the final phases, taking the tidal effects into account [62]. For this model, the parameters are the central values given in the GWTC1 catalogue [9]. Matched filtering analysis for the full signal gives SNR values of 15.2 and 14.1 for LIGO-Livingston and LIGO-Hanford respectively, i.e. a lower SNR than what has been reported in [8, 9]. This difference is due to the length of the signal, the lack of some parameter values (such as the spin) and the fact the several templates have been used to fine tune the signal in [8], whereas here we use only one template and no fit. The other template that we consider is built with the *TaylorF2* model where we use the masses that gave the maximum SNR's reported in the previous section. The SNR values are 26.9 and 18.7 in the L1 and H1 detectors. This is thus a way to see if the signal could be detected earlier for a template that gives a higher value of the SNR once the full signal is present.
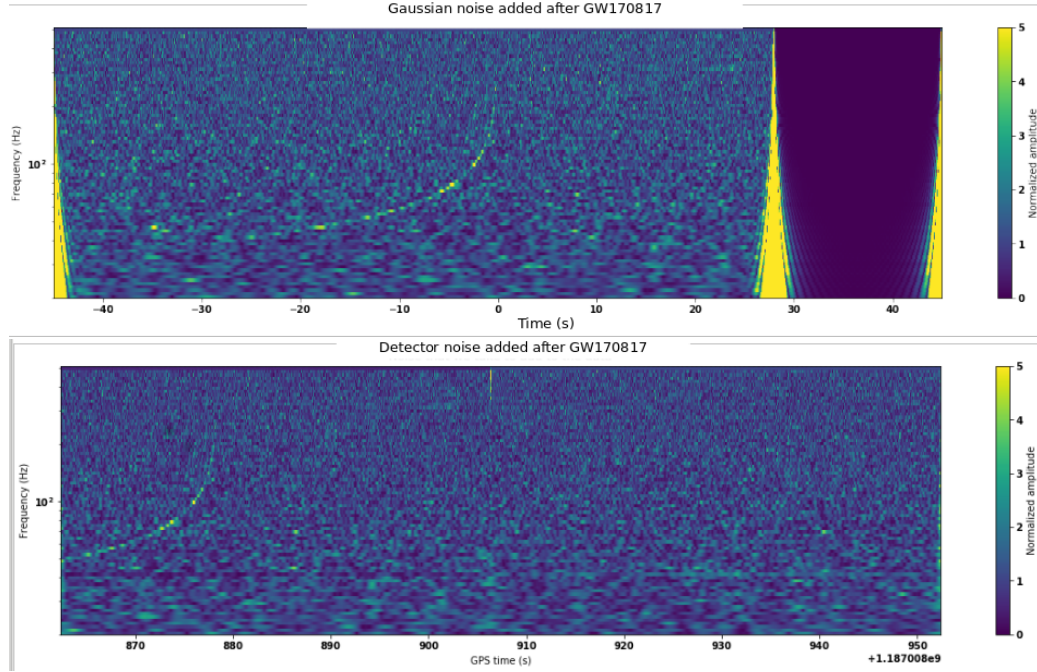
Figure 7.3: Above, the Q-transform of the time series obtained after having added 90 seconds of gaussian noise behind the data window ending 2 seconds after the merger. Below, the Q-transform obtained for the time series where 90 seconds of detector noise has been added to the same data window with the merger. The top image is not placed at the time of the event and the time axis is the time relative to the merger. The other image is placed as it is used in the procedure. We see that the addition of gaussian noise leads to an important glitch, making the first method unusable. The addition of true detector noise leads to a small over-density, as can be seen at the top of the image but it is out of the detector range.

7.3.2   Results

In order determine whether we could find the merger in advance, we compute the SNR as a function of the ending time of the window, which corresponds to the time remaining before the merger happens. The four different cases considered for the L1 detector can be seen in Fig. 7.4. The corresponding cases for the H1 detector are not represented but have the same type of behaviour, except that the increase of the SNR happens only 1 or 2 seconds before the time of the merger.

First, in all cases, we see an increase of the SNR that is similar to the one in the left panel of Fig. 6.1. We can also see that the evolution is less clean. This is probably due to the way in which the analysis is done here, with the simple appending of noise behind, instead of subtracting cleanly the signal out of the data and then reinjecting fractions of it. In addition, we see that the correct time of the increase of the signal is situated 20 seconds before the merger in the IMRPhenom case with noise added and a second or two earlier for the other case. This means that for a neutron star signal, we can detect the signal once about 80% of it is present, i.e. a smaller fraction than for black holes.

When looking at the signals here, we see that there is the possibility to predict the merger 20 seconds before it happens (and more or less 21 seconds before the first gamma ray counterpart can be detected). The prediction that an event will happen can be made with and without noise appended. However, the advantage of the first method is that it predicts the time at which the merger should happen. We also see that the exact template is not that important to make the detection possible. Indeed, we tested two different templates here in order to see whether it made a difference. We see that the time at which the event can be detected does not change between the two cases. So, we can say that an early detection is possible regardless of the exact wave model. An additional important point is that our analysis is very simple and fast. However, this is because we know the template. If it is not known, several templates could be used in parallel to do the early detection. The problem that can be noted here is that the delay of 20 seconds is too short to permit a live detection of the electromagnetic counterpart (at least for the gamma rays and neutrinos, as the delays for the other wavelengths are of the order of days [93]). However, it is important to note that we are working with O2 data, hence dating from before 2018. Nowadays, the O3 run is going on and, before starting, the components of the detectors have been updated to decrease the noise [74]. These data are not publicly available yet and it is not possible to investigate if the decrease of the noise leads to an earlier detection although it is probable that it is the case.

Because our analysis is not computationally heavy, if the time gain is important enough with the improvements of the detectors, we can imagine that it would be possible to set up a pipeline that would track the possibility to see a binary neutron star early on by having several computers looking for the evolution of the SNR for a 100 second time slice every second, each with different masses taken into account. With such a system, each processor should highpass the data, make the PSD and do the matched filtering (with clean detector noise added behind). When the increase of the SNR is observed, it is the sign that a merger is coming and an alert can be sent. The value of the minimum SNR should be optimized to maximize the time before the merger while avoiding false positives. At this stage, it is an idea that would deserve further study in
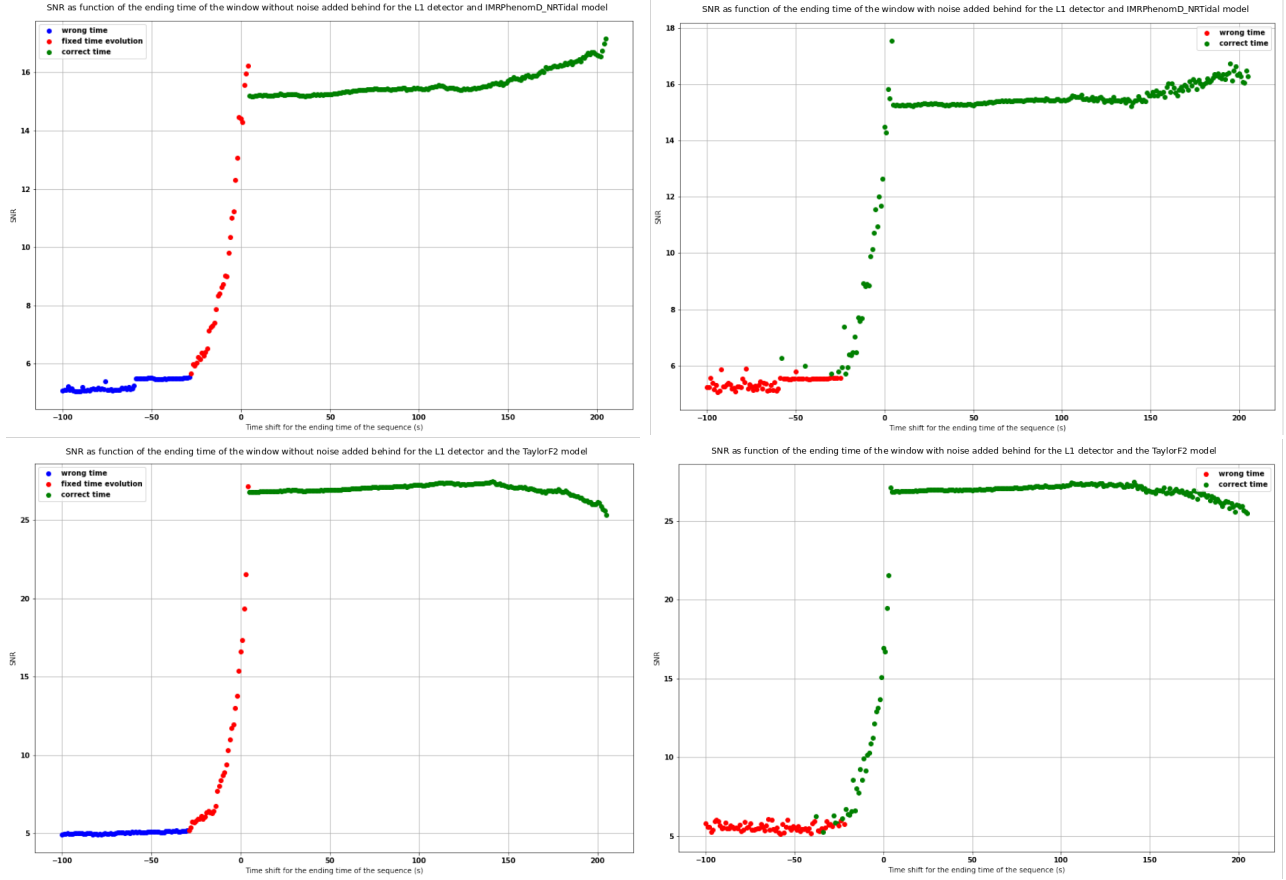
Figure 7.4: The left column corresponds to the cases where no noise has been added after the considered window whereas the right column corresponds to the cases where the detector noise has been added after the considered data window. The points labelled "fixed time evolution" correspond to the increase of the SNR that happen at a fixed time and looks like the expected evolution for a merger that would enter the window. However, this time does not correspond to that of the event (as this time is not in the considered window yet). We see that there is an increase of the SNR found in any case, but, in the case where noise is added, the time at which the increase will happen can be predicted. We can find the event more or less 20 seconds before it happens.

the perspective of improving the multi-messenger detector system for the neutron star mergers.

So far, we have only considered the case where the neutron star merger is present for a few hundreds of seconds. However, if one considers the Einstein telescope project, the neutron star merger signals will be detected once a frequency of the order of 3 Hz is reached, making the duration of the signal of about 20 hours [87]. Moreover, if we compare the fraction of signal that should be seen for the black holes and neutron stars in our case, we see that the longer signal needs a smaller fraction. As a consequence, for such long signals, the detection will probably be possible several hours before the merger happens. If we consider 80% of a 20 h signal, there would be 4 h signal remaining, which is a lower limit on the remaining time as it seems that the fraction of the signal needed to detect it decreases when the full duration increases. So, we can think that for this new detector, the multi-messenger system will be more effective with longer delays between the prediction and gamma ray counterpart. In addition, there is also the fact that the detection can be made with only a fraction of the signal. This gives the possibility to gave a tractable low-latency search, where we can rapidly detect the event before taking more time to analyze it.

Chapter 8

Overlapping signals

What happens when two gravitational wave signals come close to each other in one detector? This can seem a bit of a stretch for the O2 data, as the detection rate is not high enough (with 12 events reported in the O1-O2 catalog [9]). However, in the coming years, with the expected improvements of the detectors [74] and the introduction of the Einstein Telescope [82, 83], we expect the detection rate and the duration of the signals to increase. This leads to a higher probability of overlapping signals, especially for the Einstein Telescope, where the neutron star signal can go up to 20 h [37]. Therefore, it is probable that two binary neutron star merger signals overlap or that there is a binary black hole merger event placed somewhere in the signal of the neutron star merger. The black hole mergers will also become longer, even if they will not stretch to hours, but rather to a dozen minutes. There will also be many more detections, up to several hundreds per day [82]. In the end, there will be a relatively high probability of overlap between the events. This section looks at the possibility to disentangle two different signals when they overlap, depending on the time gap between the two mergers of the coalescences. We will look at three different cases: two binary black hole mergers, one binary black hole merger and one binary neutron star merger, and two binary neutron star mergers[1].

As before, we use the data of the second run.This section gives preliminary results on matched filtering for double events rather than a thorough study of the real cases observed or expected ones. We keep the waveforms for black holes shorter than 1 second, and for neutron stars more or less 100 seconds. The scaling of the event duration depends only on the characteristics of the detectors [4], so that the relative duration of the binary black holes mergers and the binary neutron stars mergers will remain the same. So, the results found here are a good indicator of the problems that could arise when matched filtering is used in the next generations of detectors.

---

[1]Note that it is possible to detect the merger of a neutron star and a black hole, which could then be superposed to other events. However, such an event has not been reported so far in any catalog, even if 5 events of this type can be found on the Public Alerts page of GraceDB [89] (number of events for the 23rd of March 2020).

8.1 Injection of the signal: black hole mergers

In this chapter, we inject a second event at various times in such a way that its merger (taken as the maximum amplitude of the signal) is at a chosen time interval of the other merger. Then, we compute the matched filtering to find one event or the other. Because of the small computational power available compared to that of the LIGO-Virgo collaboration, we adjust the template to the event that is sought (i.e. we do not explore a range of templates). So the template is fixed but we let the masses vary to see if we retrieve the correct ones.

One crucial aspect here is the amplitude of the injected signal compared to that of the pre-existing one. Indeed, if this amplitude is too large, the matched filtering technique will always detect the injection, even if we use a waveform adjusted for the other event. This can be seen in Fig. 8.1. It shows that, when the maximum strain of the injected signal is more than 1.5 times that of the pre-existing signal, the detected event is the loudest. However, the masses found do not correspond to those of the injection. For the right-hand part of the figure, where the injection is louder than the signal, on sees that there are a few correctly placed points. These are the points where the injected signal is added at the time of the event. Indeed, to determine the best found signal, we added it at 320 different times, ranging from 16 s before the event to 16 s after it. So, some times are very close to that of the real event and the detection is made at the time of the event (we accept errors of 0.01 seconds on time). Another important region in Fig. 8.1 is that of the transition. We see that it is not a strict limit where we go from only the detection of one event or the other, but there is a moment where we detect a bit of both. The interpretation proposed here is that, when the amplitude ratio is of the order of 1.5, the SNR values for both events are close to each other for a template with parameters corresponding to the GW170814 event. The SNR of the injection becomes higher at times when it interacts constructively with the noise. A particular case of that is when the time of the injection is close to that of the glitch present in the GW170814 data.

The behaviour described above can be seen in Fig 8.2, where we compare the values of the SNR for different times between the mergers of the injection and GW170814. There are 3 cases here: one with the masses equal to those found for the GW170814 rounded to the unit (the crosses), one with higher masses (the triangles), and one with lower masses (the dots). In any case, the primary mass of the signal is kept at $31 M_\odot$ and the secondary mass changes from one situation to the other (respectively 25, 30, and $17 M_\odot$). Higher masses mean a larger amplitude for the signal. So, we see that in the case of the higher masses, we find an SNR around 28.5 and always at the time of the injection. This high SNR is obtained even if the template used for the matched filtering has its parameters adapted to the GW170814 event, with the corresponding masses, distance, and spins [7, 9]. The high amplitude is, indeed, obscuring the other event. The smaller variations of the SNR are due to noise fluctuations in the detectors, where the noise can slightly raise or decrease the value of the SNR. The same is observed in the second case, where the amplitude is also more important. We see that for the last case, where the amplitude is lower than that of the GW170814 event, the SNR is of the order of 12.8 for all times. There is an exception when the two signals become close to each other. It leads to the increase of the SNR when they interfere constructively, and a decrease when the interference is destructive.

In Fig 8.3, we look at the evolution of the SNR as a function of the time shift when the amplitude
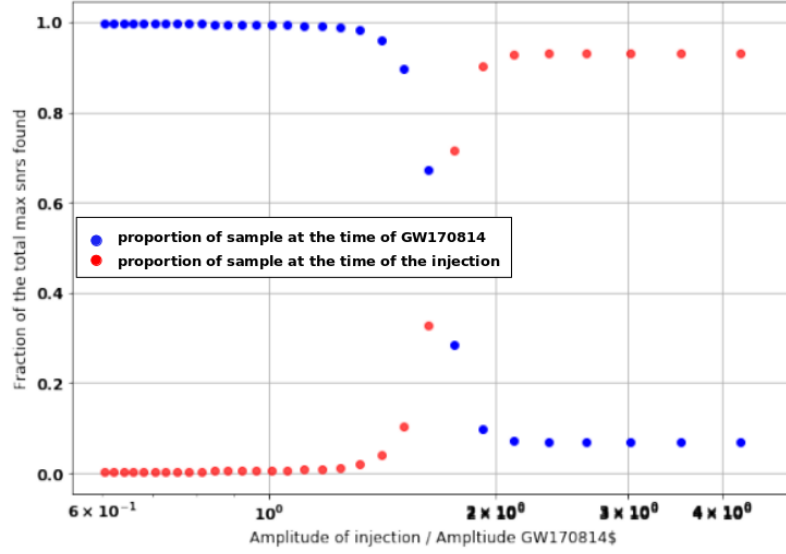
Figure 8.1: Evolution of the fraction of points that are found at the correct time of the event as a function of the amplitude of the injected signal. We compare the GW170814 event with the signal of a binary black hole merger with masses 50 $M_\odot$ and 45 $M_\odot$. The amplitude is modified by changing the distance of the event. The relative amplitude is given by the ratio of the maximum strain for both signals. Once the amplitude of the injection is more than 1.5 times that of the event present in the data, it is always detected, even if the template is adjusted for the other event.
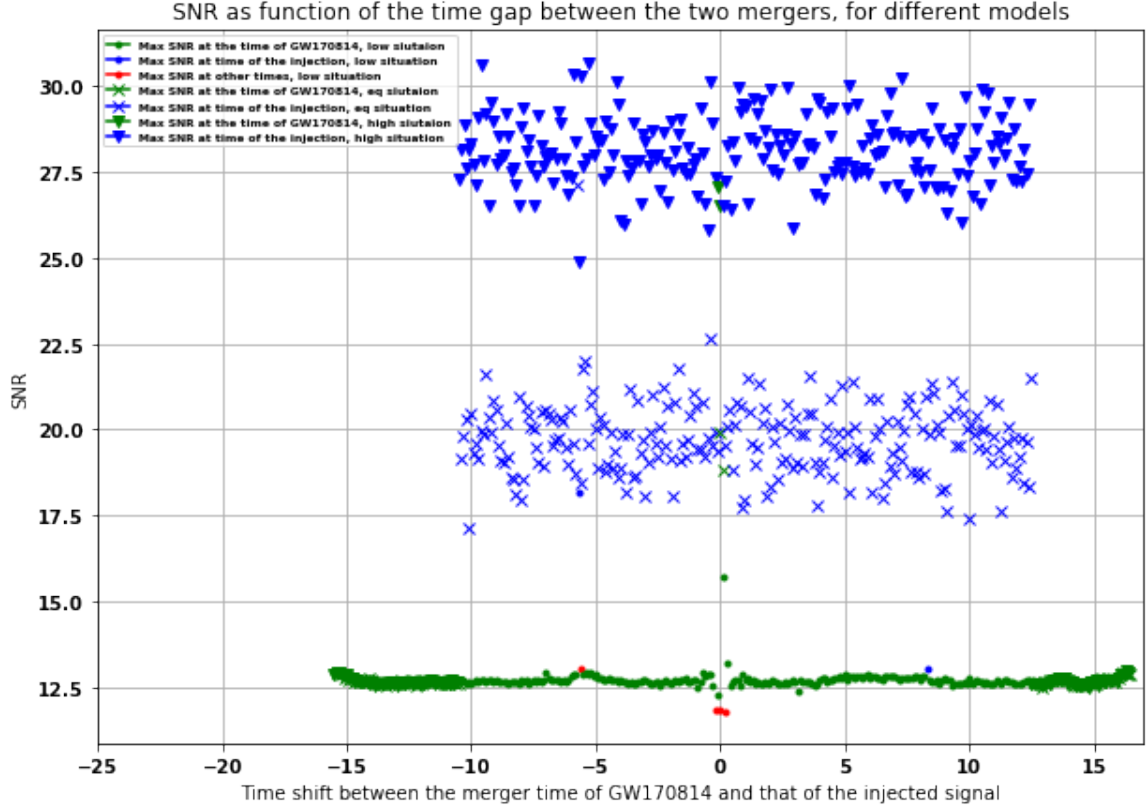
Figure 8.2: Evolution of the SNR as a function of the shift between the two mergers. The blue triangles and crosses correspond to an SNR found at the time of the injected merger, the green points correspond to the SNR found at the time of the GW170814 merger and the red points to any other time. An error of 0.01 s is tolerated for the different times. When the amplitudes are too high, the GW170814 event is never found at the corresponding time. The variations around the median for the two upper cases are due to the interactions between the injected signal and the noise.

injection is smaller than that of the event. This enables us to focus on some specific interactions that can happen between the injection and the noise and between the two events. The injected signal corresponds to a black hole merger at 580 Mpc with masses M1 $= 18\,M_\odot$ and M2 $= 30\,M_\odot$. The amplitude ratio of the injection and the strain is 0.0025. In this figure, we can see the value of the SNR as well as when it was found, with an error of 0.01 s tolerated. Globally, we see that the correct time is found. However, there are some randomly placed points where the SNR is a bit higher and found for the time of the injection. This is interpreted as the interaction of the injected signal with the noise present in the detector, leading to an increase of the SNR, bringing it to higher values than the true SNR of the event. Around a time shift of -6 s, there is a higher peak. This corresponds to the moment when the injected merger interacts with the glitch present in the LIGO-Livingston detector. We see that it leads to a large increase in the SNR. This increase was already present without the injection (see Section 3.2). The same type of increase can be observed at the time of the merger when the shift is close to zero. In that case, the interaction happens between the two mergers and the time is correct as both events are found at the time of GW70814. In Fig. 8.3, there are also a few red points, corresponding to an SNR found at a time that does not correspond to the time of the GW170814 event or the time of the injection. When looking into the details of these points, those are still close to that of one of the events but simply with a margin greater than 0.01. This is interpreted as an interaction between the glitch and the injection (for the -6 s time shift) or the interaction between the two mergers (for the zero time shift). In the case where the two events interact, we also see that the red points correspond to lower SNR. This can be due to a destructive inference between the injected signal and the GW170814 signal. Moreover, since the correspondence is not perfect, it leads to a shift of the SNR. The interaction between injection and noise cannot be avoided and adds artifacts to the results. In [7], they explain how this glitch has been removed for the analysis. However, this process is computationally costly. As a consequence, the study of the impact of the overlap on the rest of the analysis is done on another event, free from glitches.

8.2   Overlap of two black-hole mergers

We look at the evolution of the SNR depending on the time spacing between the mergers, by investigating the possibility to find parameters consistent with those of the events. We start from the GW150914 event, the first black hole detection done by the LIGO collaboration [6]. The injected signal is made of two black holes with masses $40.3\,M_\odot$ and $32.3\,M_\odot$ and at 440 Mpc. This choice is made to have the same strain amplitude as for the GW150914 event.

The procedure applied here is as follows: we look at the possibility to detect one event, by maximizing the SNR for different masses. We adjust the parameters for the event with a best-fit procedure and then subtract the event from the data. Afterwards, we repeat the process for the remaining event. The masses that are explored correspond to the error bars for the GW150914 given in [9], by steps of 0.01.

The different time gaps for which we carried the analysis are 5 s, 2 s, 1 s, 0.5 s, 0.25 s, 0.1 s, 0.05 s and 0.02 s. Once an 0.02 s gap is reached, it is not possible anymore to detect one event with the corresponding parameters. In terms of fractions of the signal, GW150914 was found as long as the last 5% of its signal was not superposed to the other signal. This is consistent with what
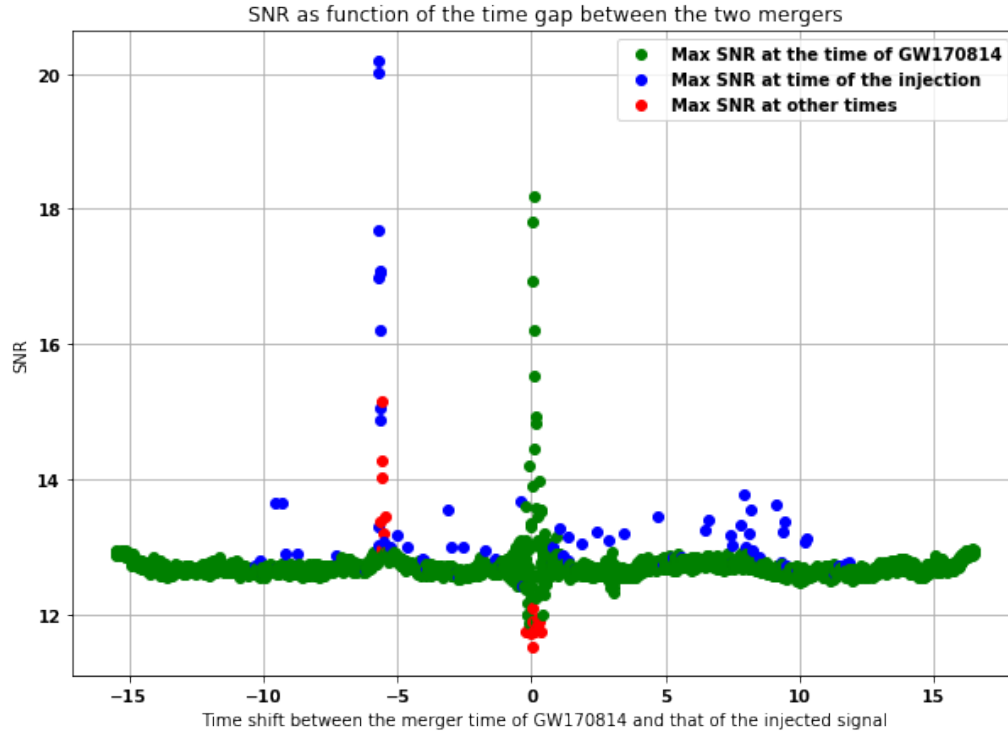
Figure 8.3: Evolution of the SNR as a function of the time gap between the two mergers when the GW170814 (reference event) strain is larger. There is a glitch present in the data which interacts with the injected event, leading to the left peak. We see that, globally, the GW170814 event is well detected, but there are times when the injection interacts with the noise and gives a higher SNR.
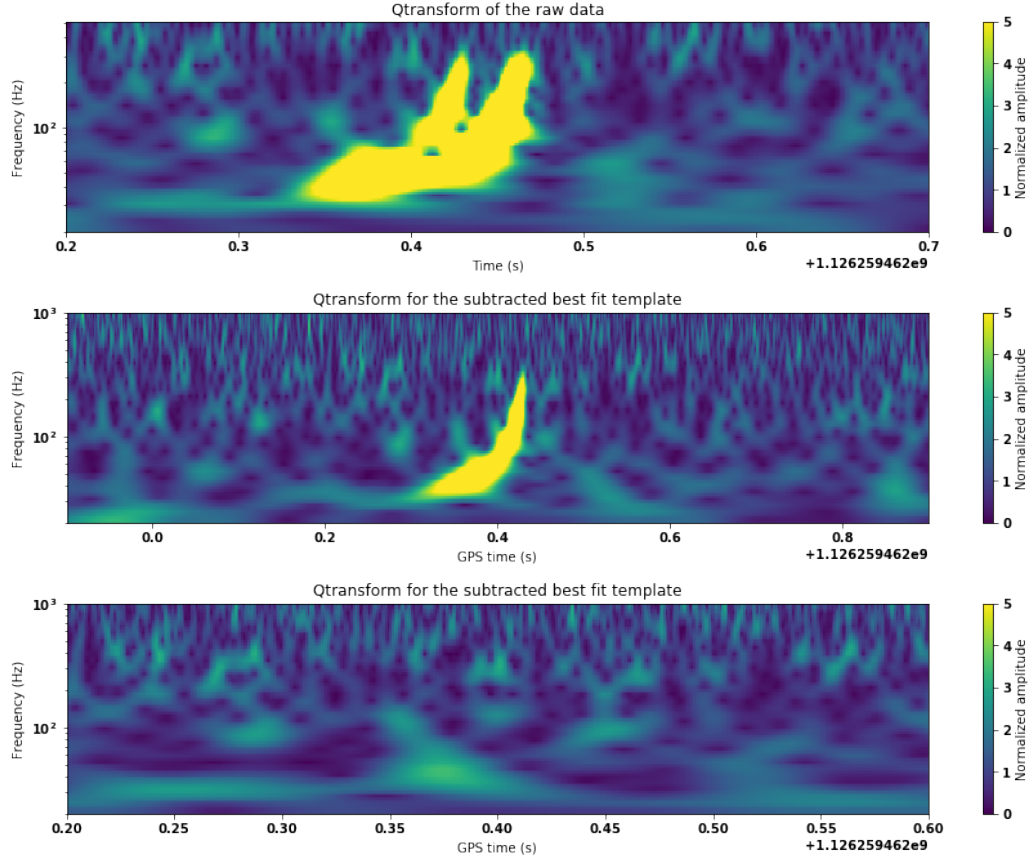
Figure 8.4: Above, the signal with the two events placed at 0.05 s of each other. In the middle, the remaining signal after the injection has been subtracted. Below, the final signal after the two events have been subtracted. From one panel to the next, the matched filtering is applied, followed by the best-fit routine and the subtraction of the result.

has been found for the variation of the SNR as a function of the fraction of the event present in the data. For the two first times, it seems clear that the matched filtering process should work, as there is no overlap between the two signals. Nevertheless, it is included here as it shows that the method applied works in these cases.

An example of the evolution of the signal through the process can be seen in Fig. 8.4, where we show the evolution of the Q-transform for the 0.05 s gap between the events. From one panel to the next, the matched filtering is made, followed by the best fit of the parameters and the subtraction of the event. One can see that both signals are well subtracted in this case. It can be argued that there is a slight over-density that remains after subtraction. However, because the parameters found are the same as for the GW150914 [9] event and the injection alone and the density is not higher than the noise, both events can still be found.

An important quantity that can be followed throughout the evolution is the SNR, which translates the significance of the event. It does not change much as long as the events are well detected. It drops from 34.3 and 19.5 for the injection and GW150914 for the 5 s gap, to 33.4 and 19.2 respectively, for the 0.05 s gap.

The situation becomes more confused for the 0.02 s gap, where several solutions have been tried to find the best-fit solution but nothing gave a convincing result. Indeed, if we keep the mass limits fixed, we see that the iteration stops with the maximum values for both masses. If we do the subtraction of one event after the best-fit and then redo the procedure, the parameters that are found for the signal are not consistent with the GW150914 event. Moreover, once the second event has been subtracted, there is still a signature with a shape similar to a merger. This event can then also be fitted and we find a third event with a low significance (its SNR is 8.3), but still high enough to be considered as a third event. We know that this event is not present in the data. Because the limit is reached for both values, we can increase the mass range for both black holes. In this case, the maximum SNR is found for 37 $M_\odot$ and 38 $M_\odot$ masses and the best-fit procedure places it at a distance of 460 Mpc. The idea here was to subtract one big event instead of several less significant ones. However, this does not work because the subtraction of the best-fit signal leads to the presence of two denser patches. Together, they could form another banana-shape. When trying to find a second signal, we find an SNR of 6 that is not at the time of the event. In conclusion, we see that, when the events are too close to each other, we cannot find the correct parameters. This problem appears clearly during the analysis. Because of this small time gap between the two mergers, we see that the probability that such a situation arises is extremely small, even if the detection rate increases a lot. As a consequence, the matched filtering technique will remain usable for the next generation detectors in the case of black hole mergers.

8.3   Overlap of a binary black hole merger and a neutron star merger

In this case, the difference in duration between the two events is important. Indeed, the first can be seen for a duration of a hundred seconds whereas the other is less than one-hundredth of it. Therefore, contrarily to the previous scenario, as the black hole goes closer and closer to the merger, it does not mask the inspiral of the neutron star signal. On the other hand, the influence on the black hole event could be bigger.

As explained in Chapter 7 about neutron stars, the signal is much longer. So, the computational cost is more important. To remain tractable for a traditional laptop, the procedure has to be modified in this case. Indeed, the fitting routine has to be abandoned and only the search by matched filtering is considered. We loop over the masses and see if the correct ones can be found. This is done by looking at the value and time of the SNR found by matched filtering. Moreover, the subtraction of the signal cannot correctly be done without fitting the signals present. In order to still be able to look at the influence of both signals, we perform the matched filtering for the neutron stars and then for the black holes. However, in some situations, without the subtraction, one signal could be found but not the other, whereas if the subtraction of the detected signal were done, the second signal would be found. When the parameters are slightly changed by the interaction between the signals, the subtraction could also play a role (as will be seen in what follows in the case of the black holes) and it could lead to better parameters.

As can be seen in Eq. (7.1), the duration of the signal depends on the masses and the detector

characteristics. Therefore, the number of events will increase when the detectors are improved, as will the duration of the signals. As a consequence, the probability to find a binary black hole signal somewhere in a binary neutron star coalescence will be larger in the coming years [74, 82].

To have a maximum amplitude for the black hole event that is comparable with that of the neutron star event, we chose two black holes with $30.1\,M_\odot$ masses and placed them at 100 Mpc. This choice enables us to make each event detectable with its specific template, without having one with an SNR much higher than the other and masking it.

The relative times between the neutron-star merger and the black-hole mergers tested are $110\,\text{s}$ (where the events should not overlap and is used to test if the procedure works well), $50\,\text{s}$, $25\,\text{s}$, $10\,\text{s}$, $5\,\text{s}$, $2.5\,\text{s}$, $1\,\text{s}$, $0.5\,\text{s}$, $0.1\,\text{s}$, $0.05\,\text{s}$, $0.02\,\text{s}$, $0.01\,\text{s}$, $0\,\text{s}$, $+0.01\,\text{s}$, $+0.05\,\text{s}$, and $+0.1\,\text{s}$. The times with a "+" denotes that the binary black hole merger is after the neutron star merger. Indeed, there is no symmetry between the events. So, the influence of the neutron star merger could be felt in the inspiral of the black holes merger, whereas the opposite is not true.

This manipulation shows that the influence of one event on the other is weak, probably due to the difference in duration. The neutron star is always detected at the correct time and with the correct masses, due to the shortness of the black hole event, which can be seen as a very small glitch present in the neutron star signal. The SNR for the neutron stars is globally not affected. Its value changes a little from one time to the other but there is no decreasing trend and we stay around 24.5 all the time. For the black holes, there is a small difference that can be seen in the parameters once it is placed $1\,\text{s}$ before the neutron star merger. The SNR drops a little (from 183 to 180) but the parameters are not as well-defined anymore. We go from masses found that were $30.1\,M_\odot$ for both black holes to a mass of $28.5\,M_\odot$ and another of $31.9\,M_\odot$. This variation of the masses holds until we are at a time shift of $+0.05\,\text{s}$, where the parameters take their initial values again. However, the chirp mass (see Eq. (2.2)) found for these masses are very close (26.24 for the different masses and 26.21 for the same masses). This is the dominating parameter for the events, which shows that the leading term is still relatively well determined. The small differences will thus come from the higher orders, where precision is lost due to the interference with the neutron stars merger. Because the neutron-star event can be found with relatively high precision, the difference could be taken away if we subtract the neutron star merger from the signal before searching for the black hole event. In any case, the signals are different enough to be well distinguished, whatever the time gap between their mergers and the difference found for the parameters correspond to values that would fall within the error bars. So, there will not be any problem for the next generations of detectors to detect neutron-star and black-hole events when they overlap.

8.4   Overlap of two neutron star signals

Because the length of these signals will be even more important, the probability that they overlap will be higher. Therefore, it is important to look at this possibility. Here, we follow the same approach as in the previous section: we inject a second signal (now a neutron stars signal) with a certain shift relative to the GW170817 event. Due to the duration of the signals,
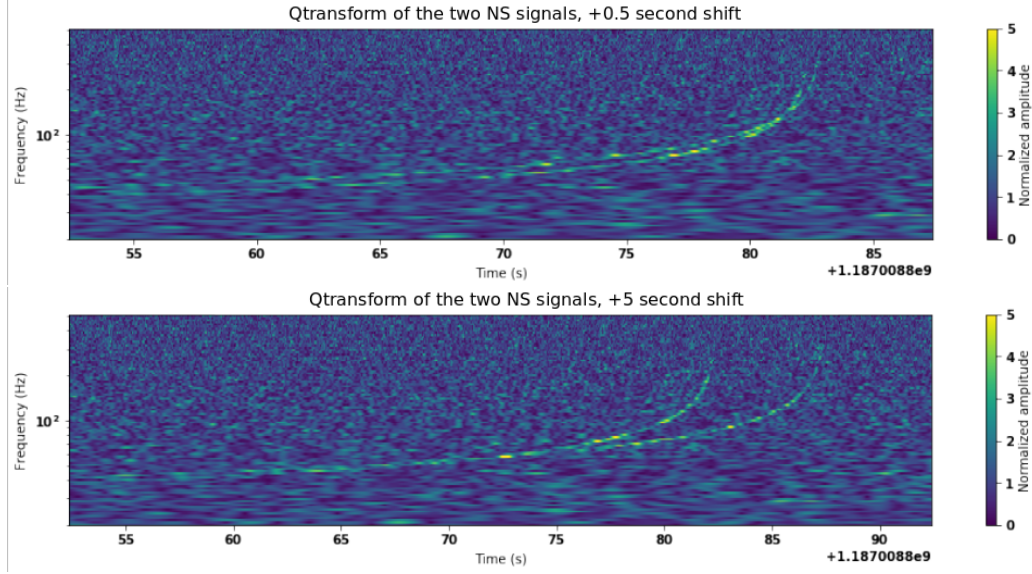
Figure 8.5: Above, the Q-transform of the two overlapping signals when the mergers have a +0.5 s shift. Below, the Q-transform for a shift of 5 s. The overlaps of the two signals are such that there is always a relatively important time-span where both are well separated. This makes it feasible to distinguish both events.

the fitting of a signal is not possible, and we cannot subtract one signal before detecting the other. So, we try to detect the one and then the other using matched filtering. We look at the possibility to retrieve the correct parameters for the event.

To keep signals that can be distinguished from one another, the injected signal corresponds to a binary neutron star coalescence with masses of $1.1\,M_\odot$ each and at a distance of $50\,$Mpc. To detect one signal and then the other, we use different mass ranges for the search. In one case, we go from the lowest to the highest bound on the masses given for GW170817 in [9], by steps of 0.01. For the second case, the loop goes from $1.0\,M_\odot$ to $1.25\,M_\odot$, by steps of 0.01.

The time shifts applied are $110\,$s, $50\,$s, $25\,$s, $10\,$s, $5\,$s, $1\,$s, $0.5\,$s, $0.1\,$s, $0.05\,$s, $0.01\,$s, $0\,$s, $+0.01\,$s, $+0.05\,$s, $+0.1\,$s, $+0.5\,$s, $+1\,$s, $+5\,$s, $+10\,$s, and $+25\,$s. The cases with "+" mean that the injection has its merger time later than that of the GW170817 event. For all these times, no significant changes in the values have been found. For GW170817, we kept the values of $1.2\,M_\odot$ and $1.48\,M_\odot$. These are the same as those found for the event without injection. On the other hand, the values found for the injection were $1.1\,M_\odot$ all along, excepts for $110\,$s, $25\,$s, $0.05\,$s, $0.01\,$s, and $+0.05\,$s, where we found $1.09\,M_\odot$ and $1.1\,M_\odot$. We see that these changes are very small. They are not linked to changes in the time of detection or a decrease of the SNR, which stays around 33 for all the shifts. The time between the two mergers is not always short in these cases. Therefore, these variations are most likely due to interferences between the injection and the noise. As a consequence, it is still possible to distinguish both events, regardless of the time gap between both mergers.

The behavior of the signals is different from that for the black holes. Here, the signals are always distinguishable. This difference can be interpreted by comparing Fig. 8.5 and Fig. 8.4.

In the case of two neutron-star merger, one can see that, even if there is a time overlap of the signals, there is no significant overlap in the frequency domain. Only a small portion of the signal overlaps at the crossing before separating again. On the other hand, for the binary black holes, there is a significant overlap in the frequency domain, ending up in a signal that looks like one big deformed event. It is in that situation that the distinction between both events cannot be done anymore. Such a situation is never met in the case of neutron stars. These signals are long enough to avoid an overlap of the frequency content over an extended period. This is very encouraging for the coming detectors, because, even if the overlap probability increases, matched filtering will still be able to do the job. However, the current way in which it is done is quite slow and should be improved. But, no completely new technique has to be found. For example, a solution could be to implement a neural network copying matched filtering. It would be much faster while conserving the knowledge already acquired about the detection technique.

8.5   Remark about the overlaps

Although the results presented above are very encouraging, they should not be taken as a guarantee for all the cases. They correspond to a preliminary investigation. Indeed, for each overlap, we have tested only one model for the injection. The latter was chosen so that both events could be distinguished easily when no overlap was present. They are probably a good example of what happens most commonly, but are not a guarantee. A question that should also be addressed is the possibility to subtract a louder event that masks another without losing information about the latter.

Conclusions

The detection of gravitational waves is one of the biggest achievements done by physicists these last years. It has required long years of development, first from a theoretical, then from a technological point of view. Nowadays, the detections become more and more regular, as the detectors are still improving. Therefore, an increase in the number of data analysts, as well as an improvement of the techniques are important for the coming years. This work presents the basics of the data analysis with the *PyCBC* package, developed by the LIGO-Virgo scientific team [21]. It also presents the influence of some parameters on the analysis and its result. Behaviors that could be observed in the coming years are also addressed.

Our main original contributions are as follow.

During the analysis of a typical event, we have seen that many parameters can be changed. For the first part of the work, the parameters recommended by the PyCBC tutorials were used. However, we explored in Chapter 5 how the analysis and its results change when we modify them. The first parameter that was considered is the value of the time-slice taken for the PSD computation. We have shown that the global shape of the PSD was modified, with more details present for the longest time intervals. We have also looked at the influence of this parameter on the SNR, and shown that, for a 32 s data sample, there was a change in its value depending on the time-slice. It had a maximum for 2 or 3 seconds and no SNR could be found anymore above a time slice of 17 s. This shows that a change in the value of this parameter can lead to the event passing under a threshold limit.

The windows used in Welch's method have also been shown to impact the analysis. In the PSD, for the lowest frequencies, the descent to the plateau has a different shape from one window to the other. For some, the plateau could not be found. The value of the SNR is also different when different windows are used. Among all the windows tested, we have found that the best one is the Hann window, which is proposed by default in PyCBC.

In Chapter 6, we looked at the impact of signal variations on the results, i.e. at the possibility to detect a black hole merger when only part of the signal is present. This is useful for the forthcoming years, during which we could detect the signal before the merger to improve the multi-wavelength tracking of the events. Another use would be the acceleration of the search for events because a smaller sample of points has to be matched. The evolution of the SNR with the fraction of the total detectable signal present was studied starting from the inspiral of a binary black hole merger to the ring-down and from the ring-down to the inspiral. For the first

case, around 90% of the signal was needed for the event to be detected and 95% before having a significant SNR. This makes the early detection of little use. The gain for the post-processing is also marginal, as we have to consider a large part of the template. These values correspond to the worst-case scenario because the smallest detectable strain considered was chosen conservatively. When starting from the ring-down, we have also shown that 5% of the signal was enough. This is not helpful for live detections or an alert system. Nevertheless, it could be used to accelerate searches in post-processing cases. This enhancement could be particularly useful for the next generation of detectors. Additionally, the difference in the length of time needed to detect the signal in one case or the other shows that the merger contains more information about the event.

This work has also insisted on the importance and the problematic of the noise in the detectors. The matched filtering technique is the optimal method to retrieve a signal swamped in second-order stationary gaussian noise. However, the noise in the detectors is not of this type. We compared real noise to gaussian noise by injecting the GW170814 event into white noise. We showed that the noise amplitude could be nearly 10 times larger for white noise than for real noise while keeping a detectable signal. We also looked at the evolution of the SNR as a function of the noise amplitude, for white noise and simulated detector noise. For both cases, the decrease in the noise amplitude leads directly to an increase in the SNR found for a given event. This shows the importance of the characterization of the noise and its suppression in the detectors. Moreover, it helps to understand how the progressive decrease of the noise in the detectors over time has lead to the ability to detect the first events.

After having focused mainly on binary black hole mergers, we looked at the neutron star mergers. The difficulties encountered due to the length of the signal for this case show the need to make the processing lighter in the coming years. and, as all signals will become longer as the sensitivity of the detectors increases.

In Chapter 7, we studied the possibility to detect the neutron star merger early on to send an early alert to the astronomers. The problem that arises here is that our modeling of the event is not as good as for black holes (due to CPU limitations) and its subtraction before addition by part is not possible. We decided to use a time window of 300 seconds and let it slide in time, taking more and more of the neutron star signal into account. Because the matched filtering returns values only for the times present in the data, we needed to add data behind the considered windows. The addition of real noise works well with only a very small over-density to be seen at very high frequency, which does not impact the detection of the event, whereas the addition of gaussian noise fails. We find that it is possible to detect the signal only ten to twenty seconds before the merger happens. This process is relatively fast and could be implemented in a low-latency search. Moreover, the decrease of the noise in the detectors will help predict the event earlier, making the alert system better for the coming enhancements of the LIGO/Virgo detectors and the Einstein Telescope.

Finally, we considered in Chapter 8 the analysis in the presence of overlapping signals. If we increase the detection rate and the duration of the signals, the probability to have overlaps between events increases. We looked at three distinct cases: two black hole mergers, one black hole merger and one neutron star merger, and two neutron star mergers. For each of them,

we studied the possibility to detect the two events depending on the time gap between their mergers. In the three cases, we saw that the matched filtering technique continues to work well for most of the time shifts. Nevertheless, for two overlapping black hole coalescences, there is a time-shift for which it does not work anymore. It is due to the overlap of the two mergers in the frequency domain for a significant time period. For the overlap between a binary neutron star merger and a binary black hole merger, the difference in duration between both signals leads to a clear distinction for all the time shifts. For two neutron-star events, we see that there are no overlaps for the signals over extended period of time. There is only a very small fraction of the signals that overlap, which makes it possible to distinguish both events, for all shifts tested. In the case of the black hole mergers, we also used a system of subtraction of the signal. Once a signal is detected, we did a best-fit procedure to find the parameters. Then, we subtracted the signal from the data and turned to the remaining event. This is probably how one will have to work when signals overlap regularly.

In the end, the goal of this work is to give an overview of a typical analysis of a gravitational wave event with PyCBC. This work shows that gravitational wave astronomy has some very well-implemented tools, even if they have their limits. Some investigated behaviors and ideas used in this work may be useful for the coming years. Moreover, the processes set up could serve as basic ideas for the data analysis and be upgraded to be used on more powerful machines. We also saw that the coming upgrades of the detectors will lead to a lot of new detections and interesting physical analyses. However, as the signals will become longer, the power needed to detect them will be even more important. So, the techniques shown here will have to evolve. One clue for this is the use of artificial intelligence.

Gravitational wave analysis is a quite new field, with still lots of prospects to look at and exciting improvements to be done.

Bibliography

[1] I. Newton. *Philosophiæ Naturalis Principia MathematicaPhilosophiæ Naturalis Principia Mathematica.* Encyclopaedia Britannica, London, 1687.

[2] Jorge L. Cervantes-Cota, S. Galindo-Uribarri, and G-F. Smoot. A Brief History of Gravitational Waves. *Universe*, 2(3):22, 2016.

[3] James Clerk Maxwell. Viii. a dynamical theory of the electromagnetic field. *Philosophical Transactions of the Royal Society of London*, 155:459–512, 1865.

[4] Maggiore Michel. Gravitational Waves. *Oxford University Press*, 2008.

[5] PyCBC Development Team and the LIGO / Virgo Collaborations. A Brief History of LIGO. `https://www.ligo.caltech.edu/system/media_files/binaries/313/original/LIGOHistory.pdf/`. Consulted on 1 October 2019.

[6] B. P. Abbott et al. GW150914: First results from the search for binary black hole coalescence with Advanced LIGO. *Phys. Rev.*, D93(12):122003, 2016.

[7] Abott B.P. et al. GW170814: A Three-Detector Observation of Gravitational Waves form a Binary Black Hole Coalescence. *Physical review letter*, 119, 2017.

[8] B. P. Abbott et al. GW170817: Observation of Gravitational Waves from a Binary Neutron Star Inspiral. *Phys. Rev. Lett.*, 119(16):161101, 2017.

[9] B. P. Abbott et al. GWTC-1: A Gravitational-Wave Transient Catalog of Compact Binary Mergers Observed by LIGO and Virgo during the First and Second Observing Runs. *Phys. Rev.*, X9(3):031040, 2019.

[10] Et Science Team. Einstein gravitational wave telescope conceptual design study. *ET-0106C-10*, 4, 2011. `http://www.et-gw.eu/index.php/etdsdocument`.

[11] LISA Science Study Team. Lisa science requirements document. 2018. `https://www.cosmos.esa.int/documents/678316/1700384/SciRD.pdf`.

[12] Peter Kalmus. *Search for Gravitational Wave Bursts from Soft Gamma Repeaters*. PhD thesis, Columbia U., 2009.

[13] LIGO Scientific Collaboration. LIGO's Interferometer. `https://www.ligo.caltech.edu/system/media_files/binaries/239/original/Basic_michelson_with_FP_and_PR_labeled.jpg?1435864227`. Consulted on 10 October 2019.

[14] LIGO Laboratory. LIGO - A Gravitational-Wave Interferometer. `https://www.ligo.caltech.edu/page/ligos-ifo`. Consulted on 10 October 2019.

[15] European Gravitational Obseravtory. A gravitatonal waves antenna. `http://www.ego-gw.it/virgodescription/indice.html`. Consulted on 10 October 2019.

[16] National Astronomical Observatory of Japan. Large-scale Cryogenic Gravitational Wave Teklescope: KAGRA. `https://www.nao.ac.jp/en/research/telescope/kagra.html`. Consulted on 10 October 2019.

[17] Max-Planck-Gesellschaft. GEO600: Gravitational Wave detector. `http://www.geo600.org/`. Consulted on 10 October 2019.

[18] LIGO Scientific Collaboration. LIGO-India. `http://www.ligo-india.in/about/institutions/`. Consulted on 10 October 2019.

[19] The Virgo Collaboration. Advanced Virgo. `http://public.virgo-gw.eu/advanced-virgo/`. Consulted on 10 October 2019.

[20] Jean-René Cudell. Introduction to astroparticles. 2019. `https://www.theo.phys.ulg.ac.be/wiki/Introduction_to_astroparticles`.

[21] PyCBC Development Team and the LIGO / Virgo Collaborations. PyCBC: Free and open software to study gravitational waves. `https://pycbc.org/`. Consulted on 23 July 2019.

[22] Samantha A. Usman et al. The PyCBC search for gravitational waves from compact binary coalescence. *Class. Quant. Grav.*, 33(21):215004, 2016.

[23] Michele Vallisneri, Jonah Kanner, Roy Williams, Alan Weinstein, and Branson Stephens. The LIGO Open Science Center. *J. Phys. Conf. Ser.*, 610(1):012021, 2015.

[24] Cody Messick, Kent Blackburn, Patrick Brady, Patrick Brockill, Kipp Cannon, Romain Cariou, Sarah Caudill, Sydney J. Chamberlin, Jolien D. E. Creighton, Ryan Everett, Chad Hanna, Drew Keppel, Ryan N. Lang, Tjonnie G. F. Li, Duncan Meacher, Alex Nielsen, Chris Pankow, Stephen Privitera, Hong Qi, Surabhi Sachdev, Laleh Sadeghian, Leo Singer, E. Gareth Thomas, Leslie Wade, Madeline Wade, Alan Weinstein, and Karsten Wiesner. Analysis framework for the prompt discovery of compact binary mergers in gravitational-wave data. *Phys. Rev. D*, 95:042001, Feb 2017.

[25] S. Klimenko, G. Vedovato, M. Drago, F. Salemi, V. Tiwari, G. A. Prodi, C. Lazzaro, K. Ackley, S. Tiwari, C. F. Da Silva, and G. Mitselmakher. Method for detection and reconstruction of gravitational wave transients with networks of advanced detectors. *PHYSICAL REVIEW D*, 93(4), February, 11 2016.

[26] Turin L. George. An Introduction to Matched Filters. *IRE Trans. Information Theory*, 1960.

[27] V. D. Zubakov L. A. Wainstein. Extraction of signals from noise. *Dover Publication*, 1962.

[28] N. Wiener. Generalized harmonic analysis. *Acta Math*, 1930.

[29] Hidaki Asada and Toshifumi Futamese. Post-Newtonian Approximation: Its Foundation and Applications. *Progress of Theoretical Physics Supplement*, 128, 1997.

[30] Ajith P. et all. Phenomenological template family for black-hole coalescence waveforms. *Class.Quant.Grav.*, 24, 2007.

[31] Thibault Damour. Introductory lectures on the Effective One Body formalism. *Int. J. Mod. Phys.*, A23:1130–1148, 2008.

[32] Husa S. et all. Frequency-domain gravitational waves from non-processing black-hole binaries. *Int.J.Mod.Phys.A*, 23, 2008.

[33] Bruce Allen. χ^2 time-frequency discriminator for gravitational wave detection. *Phys. Rev.*, D71:062001, 2005.

[34] Hogg W. David. Luminosity Distance. `https://ned.ipac.caltech.edu/level5/Hogg/Hogg7.html`. Consulted on 23 July 2019.

[35] Ken K. Y. Ng, Salvatore Vitale, Aaron Zimmerman, Katerina Chatziioannou, Davide Gerosa, and Carl-Johan Haster. Gravitational-wave astrophysics with effective-spin measurements: asymmetries and selection biases. *Phys. Rev.*, D98(8):083007, 2018.

[36] Benjamin P. Abbott et al. The basic physics of the binary black hole merger GW150914. *Annalen Phys.*, 529(1-2):1600209, 2017.

[37] Jean-René Cudell. Course on Gravitational waves. 2019. `https://www.theo.phys.ulg.ac.be/wiki/Gravitational_waves`.

[38] MCiver Jess. LIGO strain Data and Data Quality. `https://dcc.ligo.org/public/0151/G1800649/005/McIver_LIGO_open_data_workshop.pdf`. Consulted on 4 July 2019.

[39] Rudiger Paschotta. Noise in Laser Techology. `https://www.rp-photonics.com/shot_noise.html`. Consulted on 24 July 2019.

[40] A. Okutomi, K. Yamamoto, S. Miyoki, M. Ohashi, and K. Kuroda. Development of a radiation pressure noise interferometer. *J. Phys. Conf. Ser.*, 32:327–332, 2006.

[41] Flavio Vetrano and Andrea Viceré. Newtonian noise limit in atom interferometers for gravitational wave detection. *Eur. Phys. J.*, C73(10):2590, 2013.

[42] Michael Coughlin et al. Limiting the effects of earthquakes on gravitational-wave interferometers. *Class. Quant. Grav.*, 34(4):044004, 2017.

[43] Aashirwad Viswanathan Anand. A brief study of discrete and fast Fourier transform. *Uchicago*, 2010. `https://www.math.uchicago.edu/~may/VIGRE/VIGRE2010/REUPapers/Anand.pdf`.

[44] J. W. Tukey J. W. Cooley. An Algorithm for the Machine Calculation of Complex Fourier Series. *Mathematics of Computation*, 9(90):297–301, Apr 1965.

[45] Julius O. Smith. *Spectral Audio Signal Processing.* `http://ccrma.stanford.edu/~jos/sasp/`, Consulted on 12 November 2019. online book, 2011 edition.

[46] F. J. Harris. On the use of windows for harmonic analysis with the discrete fourier transform. *Proceedings of the IEEE*, 66:51–83, 1978.

[47] The SciPy community. scipy.signal.windows.hann. `https://docs.scipy.org/doc/scipy/reference/generated/scipy.signal.windows.hann.html`. Consulted on 2 October 2019.

[48] Welch D. Peter. The Use of Fast Fourier Transform for the Estimation of Power Spectra: A Method Based on Time Averaging Over Short, Modified Periodograms. *IEEE transactions on audio and electroacustics*, 2, 1967.

[49] Donald B. Percival and Andrew T. Walden. *Spectral Analysis for Physical Applications.* Cambridge University Press, 1993.

[50] Urban Alex. Calibration. `https://www.gw-openscience.org/static/workshop1/course.html`. Consulted on 4 July 2019.

[51] Christopher Biwer Duncan Brown Josh Willis Alexander Nitz, Ian Harry and Tito Dal Canton. pycbc.types module. `https://pycbc.org/pycbc/latest/html/pycbc.types.html?highlight=timeseries%20psd#pycbc.types.timeseries.TimeSeries.psd`. Consulted on 20 October 2019.

[52] LIGO Scientific Collaboration. Observing Plans and Public Alerts. `https://ligo.org/scientists/GWEMalerts.php`. Consulted on 1 April 2020.

[53] Giovanni Losurdo. Advanced Virgo first results. `https://agenda.infn.it/event/14206/attachments/16823/19094/Seminario_INFNPisa_171005.pdf`, October 2017. Talk given on 5 October 2017, Slides consulted on 12 November 2019.

[54] Judith C. Brown. Calculation of a constant q spectral transform. *The Journal of the Acoustical Society of America*, 89(1):425–434, 1991.

[55] Dennis Gabor. Communication theory and physics. *Trans. of the IRE Professional Group on Information Theory (TIT)*, 1:48–59, 1953.

[56] Pierre A Millette. The heisenberg uncertainty principle and the nyquist-shannon sampling theorem. *Progress in Physics*, 9(3):9–14, 2013.

[57] Paolo Addesso, Maurizio Longo, Stefano Marano, Vincenzo Matta, Maria Principe, and Innocenzo M. Pinto. Compressed Sensing for Time-Frequency Gravitational Wave Data Analysis. 5 2016.

[58] Shourov Chatterji. The search for gravitational wave bursts in data from the second LIGO science run. *Massachusetts Institute of Technology*, 2006.

[59] S. Chatterji, L. Blackburn, G. Martin, and E. Katsavounidis. Multiresolution techniques for the detection of gravitational-wave bursts. *Class. Quant. Grav.*, 21:S1809–S1818, 2004.

[60] LIGO Scientific Collaboration. Inspiral Gravitational Waves. `https://www.ligo.org/science/GW-Inspiral.php`. Consulted on 26 July 2019.

[61] Owen J. Benjamin and Sathyaprakash B; S. Matched filtering of gravitational waves from inspiraling compact binaries: Computational cost and template placement. *Phys. Rev. D*, 1998.

[62] Piero Rettegno. Waveform models for compact binary coalescences. 2020. Talk at Virgo Week 2020 (Pisa).

[63] Weinstein Alan. CBC Overview. `https://www.gw-openscience.org/static/workshop1/course.html`. Consulted on 4 July 2019.

[64] Christopher Biwer Duncan Brown Josh Willis Alexander Nitz, Ian Harry and Tito Dal Canton. pycbc.fiter package. `https://pycbc.org/pycbc/latest/html/pycbc.filter.html?highlight=matched_filter#pycbc.filter.matchedfilter.matched_filter`. Consulted on 8 March 2020.

[65] PyCBC Development Team and the LIGO / Virgo Collaborations. PyCBC Tutorials: Signal Consitency and Significance. `https://pycbc.org/tutorials/4/4_ChisqSignificance/`. Consulted on 23 September 2019.

[66] J. Abadie et al. Search for Gravitational Waves from Low Mass Compact Binary Coalescence in LIGO's Sixth Science Run and Virgo's Science Runs 2 and 3. *Phys. Rev. D*, 85:082002, 2012.

[67] Babak S. et al. Searching for gravitational waves from binary coalescence. *Phys.Rev. D87*, 2, 2013.

[68] Berger Roger L. Casella George. Statisctical Inference. *Duxbury*, 2002.

[69] J. Abadie et al. Search for gravitational waves from binary black hole inspiral, merger and ringdown. *Phys. Rev.*, D83:122005, 2011. [Erratum: Phys. Rev.D86,069903(2012)].

[70] N. J. Cornish T.B. Littenberg. BayesLine Bayesian Inference for Spectral Estimation of Gravitational Wave Detector Noise. *Phys. Rev. D 91, 084034*, 2015.

[71] M. J. D. Powell. An effcient method for finding the minimum of a function of several variables without calling derivatives. *The Computer Journal*, 7(2):155–162, 1964.

[72] Bernard F. Schutz. Networks of gravitational wave detectors and three figures of merit. *Class. Quant. Grav.*, 28:125023, 2011.

[73] Daniel Foreman-Mackey, David W. Hogg, Dustin Lang, and Jonathan Goodman. emcee: The MCMC Hammer. *Publications of the Astronomical Society of the Pacific*, 125(925):306, Mar 2013.

[74] B. P. Abbott et al. Prospects for Observing and Localizing Gravitational-Wave Transients with Advanced LIGO, Advanced Virgo and KAGRA. *Living Rev. Rel.*, 21(1):3, 2018.

[75] Christopher Biwer Duncan Brown Josh Willis Alexander Nitz, Ian Harry and Tito Dal Canton. pycbc.psd.estimate module. `http://pycbc.org/pycbc/latest/html/pycbc.types.html?highlight=highpass_fir#pycbc.types.timeseries.TimeSeries.highpass_fir`. Consulted on 20 October 2019.

[76] The SciPi community. scipy.signal.get.windows. `https://docs.scipy.org/doc/scipy/reference/generated/scipy.signal.get_window.html#scipy.signal.get_window`. Consulted on 3 October 2019.

[77] Sebastian Raschka. Kernel density estimation via the Parzen-Rosenblatt window method. `https://sebastianraschka.com/Articles/2014_kernel_density_est.html#23-the-window-function`, June 2014. Consulted on 29 October 2019.

[78] The MathWorks, Inc. Bohmanwin. `https://nl.mathworks.com/help/signal/ref/bohmanwin.html`. Consulted on 2 October 2019.

[79] The MathWorks, Inc. Barthannwin. `https://nl.mathworks.com/help/signal/ref/barthannwin.htmll`. Consulted on 2 October 2019.

[80] Ehud Nakar. The electromagnetic counterparts of compact binary mergers. *arXiv e-prints*, page arXiv:1912.05659, December 2019.

[81] C. J. Moore, R. H. Cole, and C. P. L. Berry. Gravitational-wave sensitivity curves. *Class. Quant. Grav.*, 32(1):015014, 2015.

[82] Bangalore Sathyaprakash, Matthew Abernathy, Fausto Acernese, P. Ajith, Bruce Allen, P. Amaro-Seoane, Nils Andersson, Sofiane Aoudia, K. Arun, P. Astone, Bala Krishnan, L. Barack, Fabrizio Barone, B. Barr, M. Barsuglia, Massimo Bassan, R. Bassiri, Mark Beker, Nicola Beveridge, and K. Yamamoto. Scientific objectives of einstein telescope. *Classical and Quantum Gravity*, 29, 06 2012.

[83] S Hild et al. Sensitivity studies for third-generation gravitational wave observatories. *Classical and Quantum Gravity*, 28(9):094013, 2011.

[84] B. P. Abbott et al. Characterization of transient noise in Advanced LIGO relevant to gravitational wave signal GW150914. *Class. Quant. Grav.*, 33(13):134001, 2016.

[85] The SciPy community. scipy.stats.norm. `https://docs.scipy.org/doc/scipy/reference/generated/scipy.stats.norm.html`. onsulted on 27 February 2020.

[86] Abadie J. Abbot B. et al Aasi, J. Enhanced sensitivity of the LIGO gravitational wave detector by using squeezed states of light. *Nature Photon*, 7(17):613–619, 2013.

[87] Duncan Meacher, Kipp Cannon, Chad Hanna, Tania Regimbau, and B. S. Sathyaprakash. Second Einstein Telescope Mock Data and Science Challenge: Low Frequency Binary Neutron Star Data Analysis. *Phys. Rev.*, D93(2):024018, 2016.

[88] Christopher Biwer Duncan Brown Josh Willis Alexander Nitz, Ian Harry and Tito Dal Canton. pycbc.noise.gaussian module. `https://pycbc.org/pycbc/latest/html/pycbc.noise.html?highlight=frequency_%20noise_from_psd#pycbc.noise.gaussian.frequency_noise_from_psd`. Consulted on 20 October 2019.

[89] LIGO Scientific Collaboration. LIGO/Virgo O3 Public Alerts. `https://gracedb.ligo.org/superevents/public/O3/`. Consulted on 27 February 2020.

[90] Daniel George and E. A. Huerta. Deep Learning for Real-time Gravitational Wave Detection and Parameter Estimation: Results with Advanced LIGO Data. *Phys. Lett.*, B778:64–70, 2018.

[91] Marco Cavaglia, Sergio Gaudio, Travis Hansen, Kai Staats, Marek Szczepanczyk, and Michele Zanolin. Improving the background of gravitational-wave searches for core collapse supernovae: A machine learning approach. *arXiv e-prints*, page arXiv:2002.04591, feb 2020.

[92] Paul D. Lasky, Nikhil Sarin, and Greg Ashton. Neutron Star Merger Remnants: Braking Indices, Gravitational Waves, and the Equation Of State. *AIP Conf. Proc.*, 2127(1):020025, 2019.

[93] B. P. Abbott et al. Multi-messenger Observations of a Binary Neutron Star Merger. *Astrophys. J.*, 848(2):L12, 2017.

[94] B. P. Abbott et al. A gravitational-wave standard siren measurement of the Hubble constant. *Nature*, 551(7678):85–88, 2017.

[95] Sergei M. Kopeikin, Gerhard Schaefer, Carl R. Gwinn, and T. Marshall Eubanks. Astrometric and timing effects of gravitational waves from localized sources. *Phys. Rev.*, D59:084023, 1999.

[96] F. K. Thielemann, M. Eichler, I. V. Panov, and B. Wehmeyer. Neutron Star Mergers and Nucleosynthesis of Heavy Elements. *Ann. Rev. Nucl. Part. Sci.*, 67:253–274, 2017.

[97] Sebastian Khan, Katerina Chatziioannou, Mark Hannam, and Frank Ohme. Phenomenological model for the gravitational-wave signal from precessing binary black holes with two-spin effects. *Phys. Rev.*, D100(2):024059, 2019.

[98] Batoul Banihashemi and Justin Vines. Gravitomagnetic tidal effects in gravitational waves from neutron star binaries. *Phys. Rev. D*, 101(6):064003, 2020.

[99] Eanna E. Flanagan and Tanja Hinderer. Constraining neutron star tidal Love numbers with gravitational wave detectors. *Phys. Rev.*, D77:021502, 2008.

[100] Christopher Biwer Duncan Brown Josh Willis Alexander Nitz, Ian Harry and Tito Dal Canton. pycbc.frame package. `https://pycbc.org/pycbc/latest/html/pycbc.frame.html?highlight=pycbc%20frame%20read_frame#pycbc.frame.frame.read_frame`. Consulted on 5 March 2020.

[101] Hsin-Yu Chen and Daniel E. Holz. The Loudest Gravitational Wave Events. 9 2014.

[102] Stephen Fairhurst. Source localization with an advanced gravitational wave detector network. *Classical and Quantum Gravity*, 28(10):105021, 2011.

[103] Christopher Biwer Duncan Brown Josh Willis Alexander Nitz, Ian Harry and Tito Dal Canton. pycbc.types package. `https://pycbc.org/pycbc/latest/html/pycbc.types.html?highlight=to_frequencyseries#pycbc.types.timeseries.TimeSeries.to_frequencyseries`. Consulted on 8 March 2020.

[104] Abraham Loeb. Electromagnetic Counterparts to Black Hole Mergers Detected by LIGO. *Astrophys. J.*, 819(2):L21, 2016.

[105] M G Beker, J F J van den Brand, E Hennes, and D S Rabeling. Newtonian noise and ambient ground motion for gravitational wave detectors. *Journal of Physics: Conference Series*, 363:012004, jun 2012.

[106] Jay Marx et al. The Gravitational Wave International Committee Roadmap: The future of gravitational wave astronomy. 11 2011.

[107] Reitze Dave. The LIGO Detector. `https://www.gw-openscience.org/static/workshop1/course.html`. Consulted on 4 July 2019.

[108] Trovato Agata. Accesing Data Through GWOSC. `https://www.gw-openscience.org/static/workshop1/course.html`. Consulted on 4 July 2019.

[109] Macleod Duncan. Introduction to gwpy. `https://www.gw-openscience.org/static/workshop1/course.html`. Consulted on 4 July 2019.

[110] Nitz Alex. CBC Search Pipelines. `https://www.gw-openscience.org/static/workshop1/course.html`. Consulted on 4 July 2019.

[111] Chatziioannou Katerina. Introduction to CBC Parameter Estimation. `https://www.gw-openscience.org/static/workshop1/course.html`. Consulted on 4 July 2019.

[112] Min-A Cho. LIGO/Virgo Low-latency Alerts and Skymaps. `https://www.gw-openscience.org/static/workshop1/course.html`. Consulted on 4 July 2019.

[113] Time Systems and Dates - GPS Time. `https://www.oc.nps.edu/oc2902w/gps/timsys.html`. Consulted on 1 July 2019.

[114] LIGO Scientific Collaboration. Find an Inspiral: Optimal matched filter. `https://www.gw-openscience.org/tutorial_optimal/`. consulted on 27 July 2019.

[115] Bruce Allen. χ^2 time-frequency discriminator for gravitational wave detection. *Phys. Rev. D*, 71:062001, 2005.

[116] Benjamin Blankertz. The Constant Q-Transform. *Technische Universität Berlin*, 1999.

[117] Bruce Allen, Warren G. Anderson, Patrick R. Brady, Duncan A. Brown, and Jolien D. E. Creighton. FINDCHIRP: An Algorithm for detection of gravitational waves from inspiraling compact binaries. *Phys. Rev.*, D85:122006, 2012.

[118] IPAC Communication and Education Team. LIGO Technology. `https://www.ligo.caltech.edu/page/ligo-technology`. Consulted on 26 September 2019.

[119] Tony Rothman. The Secret History of Gravitational Waves. `https://www.americanscientist.org/article/the-secret-history-of-gravitational-wavesl`. Consulted on 1 October 2019.

[120] Albert Einstein. Approximative Integration of the Field Equations of Gravitation. *Sitzungsber. Preuss. Akad. Wiss. Berlin (Math. Phys.)*, 1916:688–696, 1916.

[121] Yves De Rop. Les ondes gravitationelles. *Revue des Questions Scientifiques*, 178(1):113–138, 2007.

[122] PyCBC Development Team and the LIGO / Virgo Collaborations. LIGO timeline. `https://www.nsf.gov/mps/images/ligo_timeline_lg.jpg`. consulted on 5 October 2019.

[123] PyCBC Development Team and the LIGO / Virgo Collaborations. The Potential of Gravitational Waves. `https://www.ligo.org/science/GW-Potential.php`. Consulted on 5 October 2019.

[124] Subhra Priyadarshini. Gravitational waves send ripples of joy for LIGO-India. `http://www.ligo-india.in/about/institutions/`. Consulted on 10 October 2019.

[125] Eric Thrane and Joseph D. Romano. Sensitivity curves for searches for gravitational-wave backgrounds. *Phys. Rev.*, D88(12):124032, 2013.

[126] J. Aasi et al. Advanced LIGO. *Class. Quant. Grav.*, 32:074001, 2015.

[127] Christopher Biwer Duncan Brown Josh Willis Alexander Nitz, Ian Harry and Tito Dal Canton. pycbc.types.aligned module. `http://pycbc.org/pycbc/latest/html/pycbc.types.html?highlight=highpass_fir#pycbc.types.timeseries.TimeSeries.highpass_fir`. Consulted on 20 October 2019.

[128] Edmund Lai. *Practical digital signal processing for engineers and technicians*. IDC Technology. Newnes, 1 edition, 2004.

[129] JAISWAL Shiva ARYA Rachna. Design of Low pass FIR Filters using Kaiser Window Function with variable parameter Beta. *International Journal of Multidisciplinary and Current Research*, 2015.

[130] Manira Khatun. Design technique of high-pass filter using different window. *International Journal of Engineering and Computer Science*, 7(02):23585–23589, Feb. 2018.

[131] Abbott et all. Observation of gravitational waves from a binary black hole merger. *Phys. Rev. Lett.*, 116:061102, 2016.

[132] O M Solomon, Jr. Psd computations using welch's method. [power spectral density (psd)].

[133] Kai Sheng Tai, Sean T. McWilliams, and Frans Pretorius. Detecting gravitational waves from highly eccentric compact binaries. *Phys. Rev.*, D90(10):103001, 2014.

[134] Alexander H. Nitz, Thomas Dent, Tito Dal Canton, Stephen Fairhurst, and Duncan A. Brown. Detecting binary compact-object mergers with gravitational waves: Understanding and improving the sensitivity of the PyCBC search. *The Astrophysical Journal*, 849(2):118, nov 2017.

[135] R. Schilling G. Heinzel, A. Rüdiger. Spectrum and spectral density estimation by the discrete Fourier transform (DFT), including a comprehensive list of window functions and some new flat-top windows. 2002.

[136] Md Islam, Md Islam, Syed Rahman, Neelanjana Ferdous, and Jakeya Sultana. Design of fir filter using hamming window. *International Journal of Emerging Research in Management & Technology*, 3:2278–9359, 02 2014.

[137] The EGO/Virgo Outreach Team. Virgo in a nutshell. `http://public.virgo-gw.eu/virgo-in-a-nutshell/`. Consulted on 1 April 2020.